PRECISION 3-D METAL MICROSTRUCTURE ARRAY FABRICATION WITH DIRECT-WRITE ELECTRODEPOSITION

A Dissertation
Presented to
The Academic Faculty

by

Yen-Po Lin

In Partial Fulfillment
of the Requirements for the Degree
Doctor of Philosophy in the
School of Mechanical Engineering

Georgia Institute of Technology
May 2017

PRECISION 3-D METAL MICROSTRUCTURE ARRAY FABRICATION WITH DIRECT-WRITE ELECTRODEPOSITION

Approved by:

Dr. Min-Feng Yu, Co-Advisor
School of Aerospace Engineering
Georgia Institute of Technology

Dr. Min Zhou, Co-Advisor
School of Mechanical Engineering
Georgia Institute of Technology

Dr. Ting Zhu
School of Mechanical Engineering
Georgia Institute of Technology

Dr. Jerry Qi
School of Mechanical Engineering
Georgia Institute of Technology

Dr. Meilin Liu
School of Material Science and Engineering
Georgia Institute of Technology

Dr. Julian Rimoli
School of Aerospace Engineering
Georgia Institute of Technology

Date Approved: March 13th, 2017

To God for his blessing.
To my family for their unconditional love.

ACKNOWLEDGEMENTS

I would like to express my deep gratitude to my advisor, Dr. Min-Feng Yu, for his insightful guidance, support and inspiration throughout the course of my research. I would also like to thank Dr. Min Zhou for serving as my co-advisor and sharing his expertise. I thank Dr. Ting Zhu, Dr. Jerry Qi, Dr. Meilin Liu, and Dr. Julian Rimoli for serving on my graduate committee.

I would also like to thank my past colleagues, Dr. Bongwon Jeong, Dr. Arash Tajik, Jaehoon Bang and present fellow labmates Yining Chen and Fengze Jiang for creating a comfortable and friendly environment for my research.

I would like to acknowledge Dr. Yong Zhang for his helpful discussions and assistance. I would also like to thank staff members in the institute for electronics and nanotechnology at Georgia Tech for their help in developing microfabrication processes. Last but not the least, I would like to thank the National Science Foundation for their support for making this research possible.

TABLE OF CONTENTS

LIST OF TABLES

LIST OF FIGURES

SUMMARY

One of the major challenges in 3-D manufacturing is to develop a parallel manufacturing process for fabricating precision metal microstructures. Its realization promises the development of high aspect-ratio metal microstructures that could provide microscale mechanical and electrical interfaces for applications in electronic testing and bio-sensing. In this research, the self-regulated growth mechanism in the meniscus-confined direct-write electrodeposition was exploited to realize the parallel process fabrication of high density area arrays of ultrahigh aspect-ratio solid metal microwire structures; micromachining processes were developed to produce precision nozzle arrays required for the high throughput parallel process fabrications; and the underlying physics that enabled this parallel manufacturing process were revealed and formulated to guide the development. A 3-D micro-printing process that integrated the concept of discretized 3-D printing manufacturing with meniscus-confined direct-write electrodeposition was also developed to enable the fabrication of ultrahigh-density and complex-structured 3-D micro/nano-scale metal structures. Further on, a parallel 3-D micro-printing process for metal was realized. Specifically, mesoscale high quality and high-density arrays of curvilinear Cu spirals with designed mechanical and dimensional characteristics were fabricated with the metal spirals having a wire diameter of 20 μm, a coil diameter less than 100 μm, a structural aspect-ratio of over 40 and a pitch of 50 μm. High quality metal springs and spring arraying having a wire diameter of only 1 μm, a coil diameter of only 5 μm and an aspect-ratio exceed 100 were also readily fabricated. More interestingly, the Cu spirals were found to acquire exceedingly high yield strength of over 800 MPa due to the nanocrystalline microscopic nature of the Cu wires. Targeted studies

of the precision metal structures uniquely produced by such parallel manufacturing processes were carried out for applications especially in the field of microelectronics and biosensing.

CHAPTER 1

INTRODUCTION

1.1 Background

In recent developments of nanosystems, researchers have shown growing interest in the development of three-dimensional (3D) structures with micro- and nano-scale features (*1-3*), particularly high aspect-ratio 3-D metal structures due to the unique mechanical and electrical qualities of metal. Ultrahigh aspect-ratio structures with microscale/nanoscale feature resolutions are necessary interface components in advanced system packaging of microchips as well as in the integration of microelectronics with multifunctional sensor networks and even biological living systems. These can be found in the case of developing 3-D chips with the use of through silicon vias in chip scale packaging for multilayer interconnections, and developing neural probes with high density microneedle arrays for brain stimulation(*4, 5*). Besides using metal material, the high aspect-ratio 3-D interface structures integrated within such systems needs to be material compatible in chip packaging applications, and to be biocompatible in neural probe applications. Further, to make the integration of such components in dedicated applications economically viable, parallel process-based manufacturing is desired to fabricate such precision interfaces. However, the current means of fabricating such micro- and nano-scale 3D metal structures remain limited.

Most common methods for microfabrication of a high aspect-ratio structure are either surface micromachining based, LIGA (a German acronym for a process involving lithography, electroforming, and molding) based, or 3-D printing based. Although all of them are capable of fabricating high aspect-ratio structures, each of them has its limitations due to its adopted fabrication mechanism.

1.2 Review of 3-D Fabrication Methods

1.2.1 Surface-machining-based and LIGA-based methods

Surface micromachining based methods refers to 2-D photolithography based ones. It is based on transferring patterns from photomasks to photoresists through exposure and development, as shown in Figure 1. Materials on a substrate are etched afterwards by either chemical wet etching, physical dry etching, or combination of these two etching methods (*6*). However, surface micromachining-based methods are intrinsically 2-D based, therefore they are limited in developing micro-structures of limited thickness (height). To produce features of larger thickness based on micro-machining methods, two processes are usually involved, which are deep reactive ion etching (DRIE) and multi-layer development.

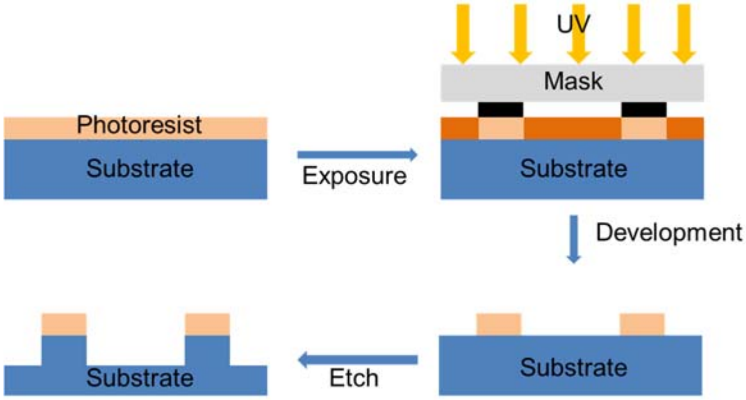

Figure 1. Surface machining based methods

Similar to the reactive ion etching, DRIE uses ions generated by a plasma to physically bombard a substrate to remove unwanted materials anisotropically to create shallow features. However, DRIE process includes an additional passivation process between two etch processes to protect etched sidewall from further etching in the consecutive etching cycle (Figure 2). Many such etching and passivation cycles are performed to realize the fabrication of high aspect-ratio structures. However, structures created using DRIE have only simple vertical geometries, and the aspect-ratio is limited to below 30.

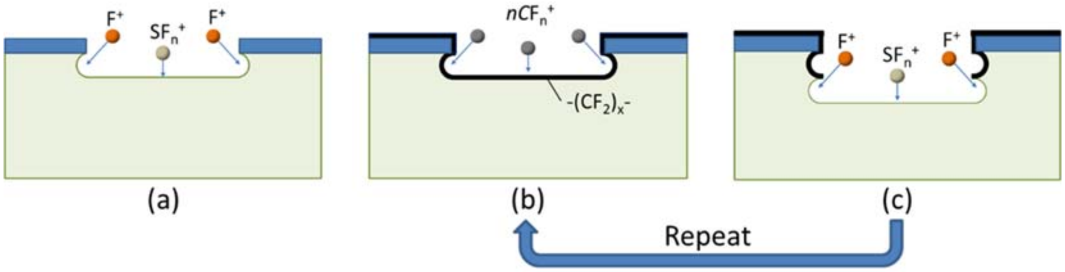

Figure 2. Schematic diagram of DRIE Process of silicon etch, including (a) SF6 etching of the exposed substrate, (b) passivation of the etched structure to prevent sidewalls from further etching, and (c) consecutive SF6 etching for deepening patterned features. Steps (b) and (c) are repeated to create high aspect-ratio features.

The other process for fabricating high aspect-ratio microstructures involves multi-layer development, in which repeated patterning, developing, layer deposition and etching are applied layer after layer (*7-10*). However, this process multiplies the number of process steps needed for the microfabrication, demands high precision in pattern alignment especially with the increasing number of needed layers, and requires the development of increasing number of photomasks, which can be very costly.

LIGA process (acronym for Lithography, Electroforming, and Molding) is another process used for fabricating very high aspect-ratio microstructures (*11-13*). Unlike typical photolithography methods, the LIGA process uses x-ray produced from a synchrotron to expose very thick specialty photoresists to make microstructures up to several millimeters in height. Several specialty photoresists were used in LIGA based process, e.g. PMMA, SU-8, etc. (*6, 14, 15*). The LIGA process, however, is hardly compatible with the traditional photolithography based microfabrication processes widely used for developing integrated electronic devices.

Although both surface machining-based and LIGA-based methods are high throughput processes that are capable of high volume production, they are not ideal for making high aspect-ratio microstructures with complex 3-D shapes. To make somewhat complex 3-D microstructures would require a layer-by-layer process that is time-consuming, costly and less precise. In addition, these methods are primarily designed for fabricating structures of semiconductor-related materials, mostly silicon or silicon related materials.

1.2.2 3-D printing-based methods

Unlike the photolithography based methods, which are essentially subtractive methods based on removing material from the bulk form to produce the desired form with designed microscale features, 3-D printing is an additive manufacturing method that applies the way of addition to precisely add and join materials to produce the desired 3-D structures. In 3-D printing, materials are continuously deposited and bonded according to a minimum unit volume defined as a voxel, analogous to a pixel in the two-dimensional representation, to form a final 3-D structure regardless of its geometrical complexity. As a popular tool in rapid prototyping, 3-D printing provides significant design and fabrication flexibility, shortens product design cycles and thus drastically reduces the costs of prototyping. As a result, several 3-D printing-based techniques that print structures with micro-/nano-scale precision were developed to circumvent the constraints in lithography related fabrication technologies and produces arbitrary-shaped 3D microscale structures that cannot be produced with the surface-machining based and LIGA-based methods mentioned above.

Among those 3-D printing techniques capable of fabricating 3-D structures with microscale precision, microprobe-based fabrication techniques are widely used, in which a specialized microprobe is used to spatially define and control the material addition for 3-D construction.

In the localized electrochemical deposition (LECD), a sharpened metal probe was biased and used to create a localized electric field over a conductive substrate immersed in an electrolyte tank (*16-19*) to induce localized electrodeposition of metal. The movement of the probe thus defines the shape forming of the deposited metal wire, as shown in Figure 3 (A). However, the localization of electrodeposition is realized through the confinement of the electric field which is not precisely localized within the electrolyte. The resolution of LECD is thus somewhat limited and is difficult to fabricate structures having feature resolution of less than 10 µm (Figure 3 (B)). More problematically, LECD produces mainly structures that have high surface roughness and are even porous due to the high voltage involved in electrodeposition, which degrades the mechanical and electrical properties of the fabricated structures for applications (*20-22*). Another concern is that the LECD process subjects the work piece in an electrolyte solution, and thus can introduce contamination onto the work piece.

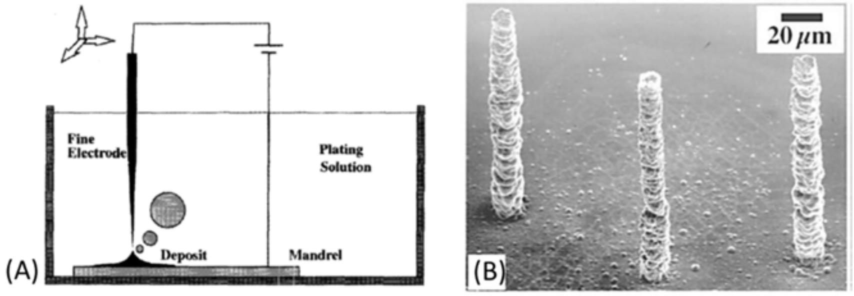

Figure 3. (A) Schematic showing the localized electrochemical deposition process (From (*16*)). (B) Representative metal wires fabricated with LECD (From (*19*))

In ink-based printing methods (basically the traditional robocasting methods), a microscale nozzle is typically used to dispense functional ink. The nozzle is translated with a nanoposisioning system to lay down the ink to make a 3-D microstructure, as shown in Figure 4 (A). To make it work for making microscale resolution structures, specific inks with specially designed rheological and viscoelatic properties are required. Ideally, the ink needs to possess a low viscosity that can facilitate its extrusion through the micronozzle under an applied pressure. In addition, to retain the shape of the microstructure, the ink needs to be able to solidify quickly upon being extruded from the nozzle. Periodic structures and microvascular networks with microscale resolution have been fabricated using these methods for potential applications in optics and microfluidics (*23-25*). However, these methods deposit materials in the x-y plane only, and the realization of 3-D structures is based on the sequential layer-wise deposition, as shown in Figure 4 (B) and (C).

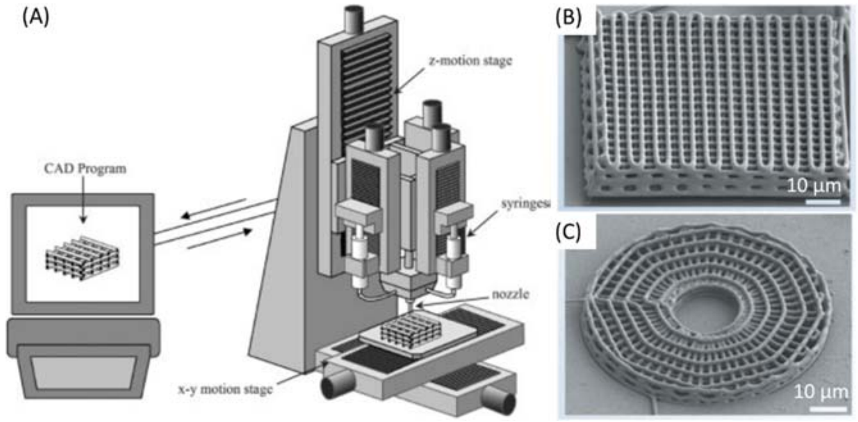

Figure 4. (A) Schematic showing the deposition system used in an ink-based micro-printing. Inks are housed in the syringe mounted on the z motion stage, and deposited through a cylindrical micro-nozzle onto a x-y stage (From (*24*)). (B) and (C) are micro 3-D periodic structures printed from a PAA/PEI ink (From (*25*)).

In order to create truly 3D high aspect-ratio microstructures, some ink-based methods extrude high concentration colloidal inks with embedded silver nanoparticles in air through micronozzles, which enables omnidirectional printing of flexible, stretchable and spanning microelectronics (*26*), shown in Figure 5. However, silver colloidal structures produced using this technique are with low mechanical and electrical properties because material are formed by silver nanoparticle congregation instead of chemical bonding. As a result, hours of the annealing process are required to convert colloidal structures into high quality metallic structures, such a high temperature process limits its application in electronic processing. Furthermore, the resolution of this method is limited by the minimum nozzle diameter can be used without clogging due to the finite size of the colloidal particles in the dispersion.

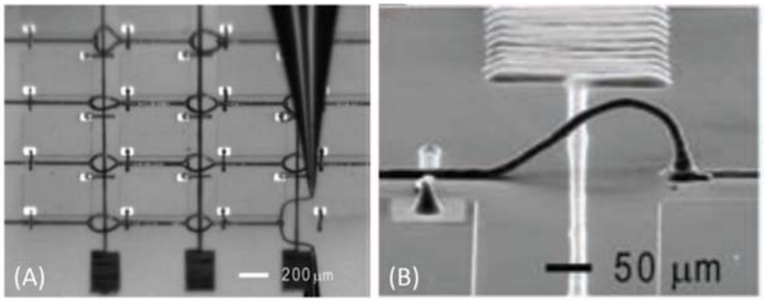

Figure 5. (A) Optical image of a spanning silver interconnects micro-printed onto an electrode LED chip array. (B) The SEM image of a silver interconnect arch printed over an electrode junction. (From (*26*))

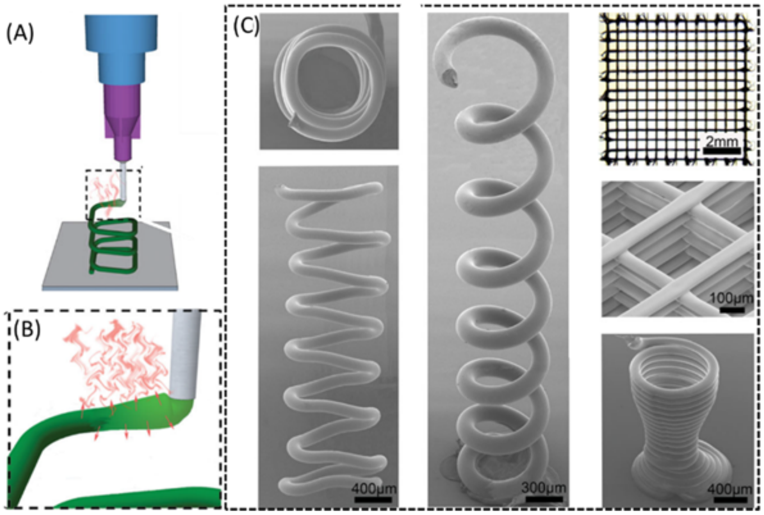

Figure 6. Schematic illustration of the SC-DW process. (A) Deposition of the thermoplastic solution through a micronozzle. (B) Rapid solvent evaporation port extrusion. (C) Several microstructures manufactured by SC-DW, including PLA micro-spirals, a PLA scaffold and a PLA cup. (From (*27*))

Another ink-based method, solvent-cast direct-write (SC-DW), uses the solvent ink with dissolvable thermoplastic polymers to fabricate high microstructures with high aspect-ratio (*27, 28*). After the extrusion, the rapid solvent evaporation takes place and the rigidity of the filament increases due to the increase of polymer concentration. Although SC-DW was used to fabricate several 3D microstructures, including 3-D spirals, micro-cups, and micro-scaffolds, only limited materials can be used in this technique (*27*). Besides, when solvent evaporates, micro-structures produced by SC-DW undergo significant volume changes, which could be a potential problem for precision manufacturing.

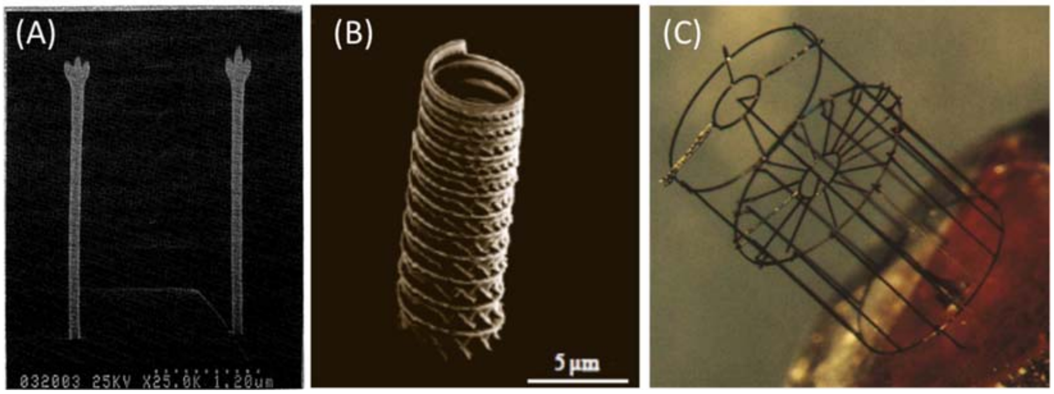

Figure 7. (A) Special-lized three-fold pointed AMF tips deposited via EB-FIB (From (*29*))(B) Micro Leaning Tower of Pisa fabricated via FIB-CVD (From (*30*))(C) Aluminum oxide 3D microstructure produced via LCVD process (From (*31*))

Beam-induced chemical-vapor-deposition (CVD)-based techniques use high-power beam to direct the material deposition, such as electron-beam CVD (EB-CVD) (*29, 32-34*), focused-ion-beam CVD (FIB-CVD) (*30, 35*) and laser-CVD (L-CVD) (*31, 36, 37*). These beam-induced CVD are capable of fabricating 3-D microstructures, shown in Figure 7, with down to 10 nm resolution owing to the absolute confinement provided by induced beams. Both EB-CVD and FIB-CVD have a better resolution than L-CVD, but EB-CVD is a slower process when compared with L-CVD and FIB-CVD (*30*). During the process, induced high-power beams dissociate a precursor species resulting in a solid deposit on the substrate, and the substrate move with respect to the beam source to change deposition location gradually until final objects are formed. Various materials can be deposited using these methods including diamond-like carbon (*38*), aluminum(*39*), aluminum oxide(*36*), tungsten (*40, 41*) and SiO_x (*42, 43*). However, these techniques demand specialized environments such as a high vacuum environment and a high-power beam source, therefore their operations are still cost prohibitive. Besides, metals deposited using these methods suffers from low electrical conductivities (*44*).

Several metal-droplet-based printing techniques such as the droplet jetting (*45, 46*) and laser-induced forward transfer (*47, 48*) use jetting modules to transfer metal droplets onto a substrate to form 3-D microstructure by stacking of droplets. As a result, the resolution of these techniques depends on the minimum droplet that can be produced. Although some high aspect-ratio 3-D structured can be fabricated using these methods(*45, 47, 48*), structures tend to with low qualities because of unreliable droplet transfer processes. Besides, these methods are limited by material selection, fabrication resolution, and fabrication reliability.

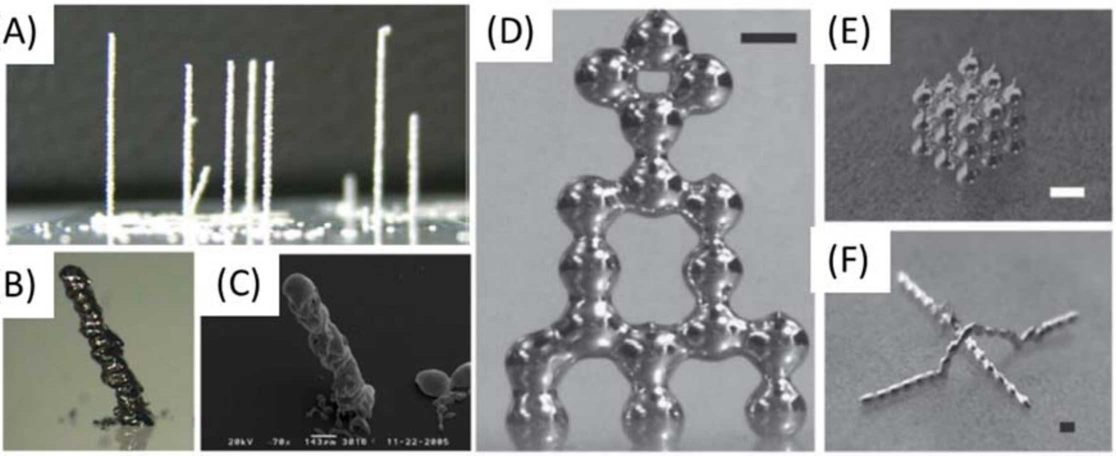

Figure 8. (A), (B), and (C) are 3-D columns stacked by jetted solder droplets, taken from (*45*). (A) A optical image of a jetted column array. (B) A close optical image of a stacked column. (C) The SEM image of the stacked column. (D), (E), and (F) are several 3-D structures stacked by liquid metal droplets, taken from (*49*). (D) A 3-D tower of stacked droplets. Scale bar is 500 µm. (E) A 3-D cubic array of stacked droplets. Scale bar is 500 µm. (F) A metal wire and an arch composed of liquid metal droplets. Scale bar is 500 µm.

Similar to metal-droplet-based printing techniques, liquid metal printing (*49*) use metal droplet to form 3D microstructures. Yet, instead of transfer metal droplets through high temperature transformation, liquid metal droplets are formed at low temperature with oxide shells. A computer controlled dispense tool then stack liquid metal droplets one after another to gradually finish a final object. As a result, materials can be used in this process is highly limited and the resulting structure is not mechanically robust for most applications.

Methods based on the photo-polymerization rely on use of light source to cure photosensitive polymers to fabricate 3D microstructures. For instance, the stereolithography (SLA) focuses an UV laser on to a thin layer of photopolymer resin performs photopolymerization layer-by-layer (*50-53*). After solidify each layer of the polymer, the surface is recoated with a new layer of photopolymer that flow in, schematically shown in Figure 9 (A). Then the object is reattached to the new then layer of the photopolymer to preform another cycle of the solidification, re-coating and re-positioning. In the past, SLA has been used to fabricate various 3-D microstructures with complex geometries(*52, 53*), some are shown in Figure 9 (A). Yet, due to the complicate repeating process, the production rate of SLA is low(*54*). On the contrary, Continuous liquid interface production (CLIP) achieved high speed photo-polymerization process with the ultraviolet (UV) light to print complex solid parts at rates of hundreds of millimeters per hour with resolution down to submicron (*54*), which is schematically shown in Figure 9 (B). When draw parts out of a pool of liquid photopolymer resin, an oxygen-permeable window below the UV image projection plane creating a persistent liquid interface where photopolymerization is inhibited. As a result, CLIP is a continuous process that avoids a series of steps to cure, replenish and reposition for each additive cycle in typical stereolithography and the production rate is up to 100 times faster than that of the stereolithography.

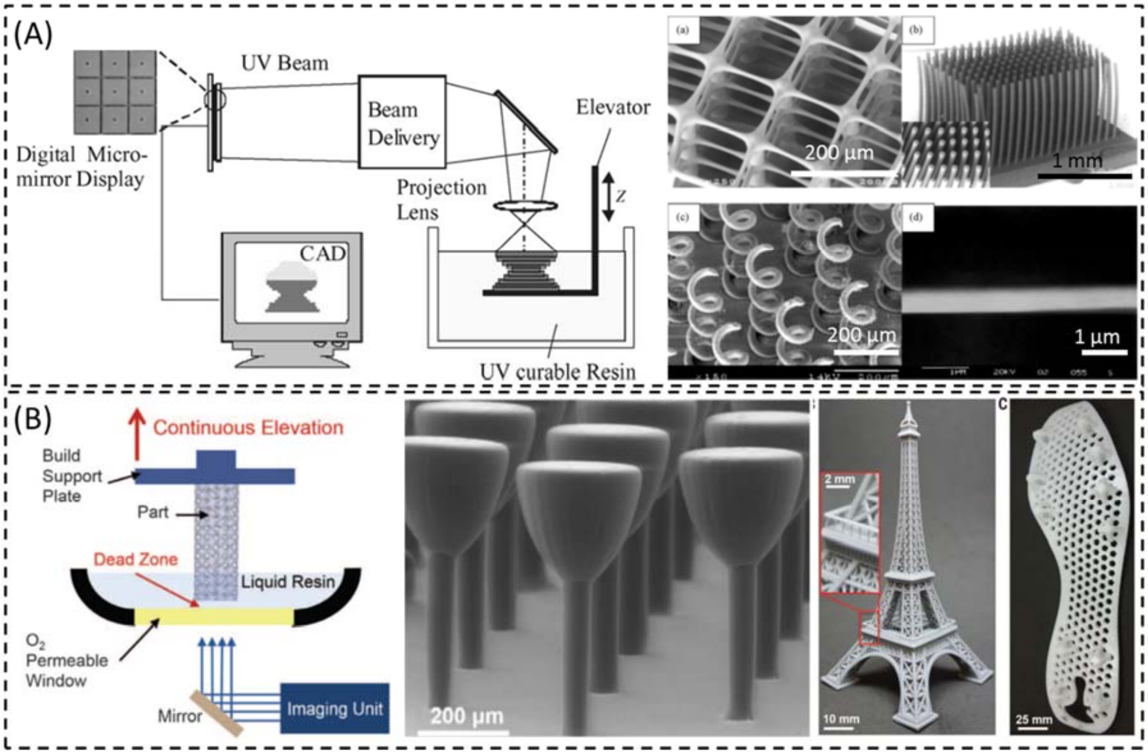

Figure 9. Comparison between SLA and CLIP processes. (A) Schematic illustration of the SLA process and numerous printed microstructures, including a micro matrix with suspended beam diameter of 5 µm, a high aspect-ratio micro rod array with overall size of 2 mm by 1 mm, a micro coil array with coil diameter of 100 µm and the wire diameter of 25 µm, and a suspended ultra-thin line with diameter of 0.6 µm (From (*53*)). (B) Schematic representation of the CLIP process and a variety of printed structures, including a micro-pedal array with stems 50 µm in diameter, Eiffel Tower model over 10 cm tall with features smaller than 1 mm, and a shoe cleat that is over 20 cm in length (From (*54*)).

The resolution of processes such as SLA are limited by the minimum layer thickness allowed due to viscosity and surface tension of the resin (*55*). To overcome this problem, the two-photon polymerization (2PP) uses a mode locked pulsed infrared laser to cure photosensitive polymer to fabricate 3D microstructures(*52, 56-58*). In the 2PP process, the photoinitiator needs two photons release a free radical that can initiate polymerization. Since only the photoinitiator near the center of the laser has high photon density that strike the same photoinitiator molecule, the resolution of photopolymerication process increase considerably, about 100 nm (*52, 57*). Several micro-3-D structures have been printed using 2PP for different applications includes photonic crystals(*59, 60*), optical memories(*61, 62*), microrotors(*63-65*) and micro-oscillators(*66*).

Despite numerous studies have demonstrated printing various functional materials using micro-3DP for different applications (*67-69*), most promising 3-D printing technologies that print materials with sub-micron resolutions, to date, are polymer-based (*54, 58, 70*) or colloidal ink-based with embedded metal particles (*26*), which cannot satisfy the requirements of many applications because of their low material strength and electrical conductivity. Although hollow structures including metal and ceramic materials have been developed (*2, 71-73*) by combining a polymerization process with an electroless plating post-process, fabrication processes remain complicated and restricted. In addition, metal droplet-based and LECD techniques are not capable of producing high-quality metal micro-structures for electronic applications.

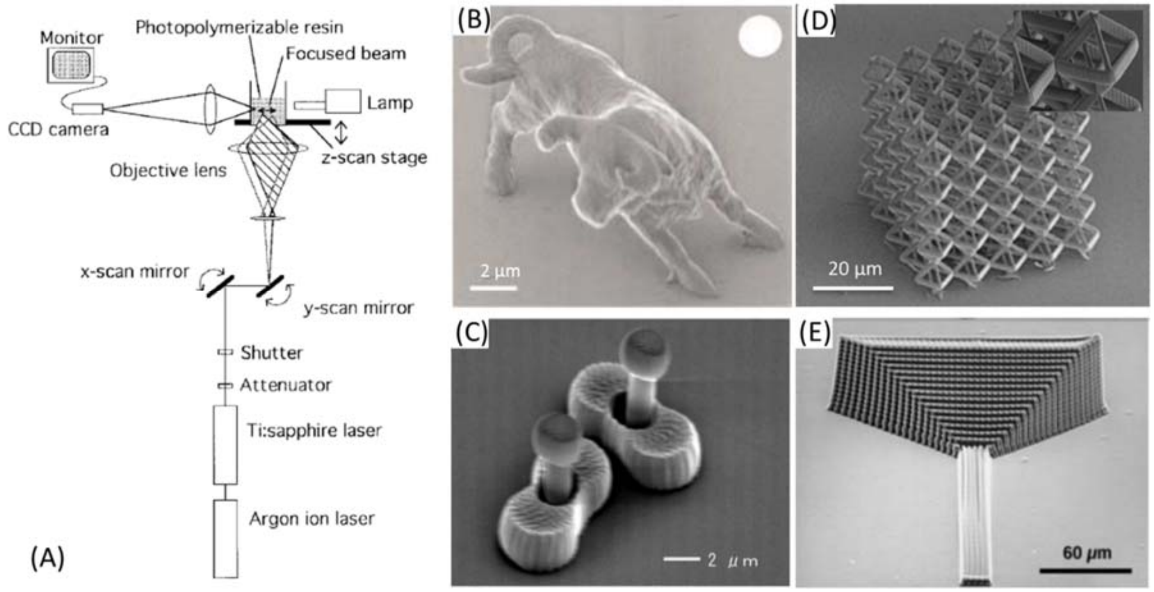

Figure 10. (A) Schematic diagram depicts the optical system of the 2PP process for 3-D microfabrication (From (*56*)). A wide variety of micro-structures fabricated based on 2PP, including (B) a printed bull micro-sculpture (From (*70*)), (C) a optically driven micropump (From (*65*)), (D) a 3-D hollow metallic nanolattices (From (73)), and (E) a tapered waveguide micro-structure (From (61)).

An alternative for fabricating micro metal structures is the electrochemical fabrication process (EFAB), which combines photolithography, electrodeposition, and planarization processes to manufacture micro devices layer-by-layer (*74-76*), schematically depicts in Figure 11. Despite the high-quality material produced by EFAB, multiple steps involved in each layer preclude such a technology from producing complex out-of-plane structures. Besides, EFAB, intrinsically relies on aforementioned 2-D photolithography, is limited in fabrication of structures above certain height.

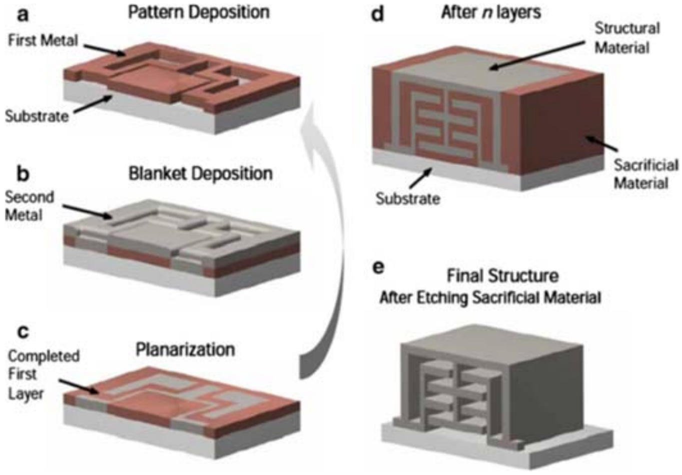

Figure 11. Schematic diagram of the EFAB process

Promising conventional metal 3-D printing methods such as selective laser sintering (SLS) (*77-79*) and selective laser melting (SLM) (*80-83*) undergo high-temperature processes that involve a high-power laser and a controlled environment filled with inert gas, which makes it costly to operate. Besides, using micro-/nano-metal particles to print micro-objects results in inter-particle force prevents these methods from forming dense objects. Resolutions of conventional SLS and SLM are difficult to extend to sub-micron because layers with finer powders are loose, owing to the prevailing forces between particles (*55, 78, 84*), could be found in Figure 12.

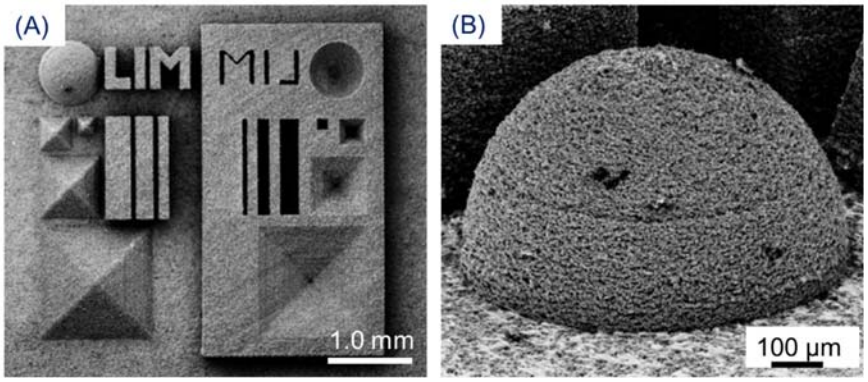

Figure 12. (A) SEM images of a multi-shape test structure sintered of tungsten powder with average grain size of 300nm. (B) A close inspection shows the porous rough surface of the printed micro-structure.

Although the 3-D printing-based methods are the most versatile and have almost no theoretical limited to make microstructures of any meaningful height, they are currently not capable of fabricating electronics-quality metal microstructures, because the resolution of conventional 3-D printing is not applicable in the micro/nano scale. In addition, these serial processes are arduous to scale up as a result of system limitations, which preclude high-volume production. Therefore, a promising low cost and flexible method that fabricates metal material in micro/nano scale is still unavailable.

1.3 Objective and Outline

Further development in making high aspect-ratio microstructures would ideally possess the combination of the several breakthroughs. First, the method performs fabrications in a parallel process. Second, the method retains the microscale and even nanoscale resolution of photolithography. Third, the method overcomes the height limitation in lithography-based microfabrication. Fourth, the method is process-compatible to existing microfabrication processes. Last but not least, the method realizes multi-material microfabrication. Such breakthroughs would bring in exciting new applications in any system interfaces that require mechanical and electrical transitions from microscale to mesoscale, such as in chip scale packaging, wafer scale testing and biological cell-electronics integration.

The objective of this research is to develop a high-throughput parallel direct-write process that fabricates high quality 3-D micro-/nano-scale metal structures with a nozzle array. The primary focus is to develop the theoretical understanding of electrochemical processes involved in the nozzle array based meniscus-confined electrodeposition, to develop the necessary microfabrication process for fabricating the precision nozzle array systems needed for the parallel process fabrications, and finally, to realize experimentally the parallel process direct-write electrodeposition fabrication of electronics quality 3-D metal structures with microscale and nanoscale resolution.

In this dissertation, chapter 2 describes the principle of the meniscus-confined electrodeposition, followed by developing and understanding the self-regulated mechanisms involved in the array-based meniscus-confined electrodeposition in chapter 3. Chapter 4 covers the design and microfabrication of the nozzle array systems. Actual array-based fabrications of 3-D metal structures are demonstrated and the mechanical characterization of the resulting structures is performed also in chapter 4. Chapter 5 describes the design, fabrication and the mechanical characterization of high-density metal electrode arrays that can be potentially used for wafer probing applications. Chapter 6 describes a 3-D printing method that realizes the fabrication of complex-shaped 3-D micro-/nano-scale metal structures and ultrahigh density metal electrode arrays. Chapter 7 introduces several extended developments of the meniscus-confined electrochemical methods for developing expanded applications. Finally, Chapter 8 summarize the whole research.

CHAPTER 2

MENISCUS-CONFINED ELECTRODEPOSITION

2.1 Introduction

2.1.1 Electrodeposition

Electrodeposition of metal and metal alloys involves the electrochemical reaction that reduces metal ions from aqueous, organic, and fused-salt electrolytes. A typical setup of the electrodeposition in the aqueous solution consists of an anode and a cathode in the electrolyte, and the reduction of metal ions M^{Z+} in an aqueous solution can be expressed as

$$M_{aqueous}^{Z+} + ze^{-} \rightarrow M_{lattice} \quad (1)$$

During the deposition process, electrons consumed in the reaction usually come from two electron source: the external power supply or reducing agent in the solution such as in the electroless deposition process. In this study, only the electrochemical reaction that deploys the external power supply as the electron source was applied, and the typical setup consists of an anode and a cathode that are immersed in the electrolyte. In this case, the workpiece to be plated in the circuit is the cathode, at which the reduction takes place. The electrolyte contains dissolved metal salts along with other ions that permit the electricity to flow. In the setup, the anode and the cathode were connected to an external power supply that supplies electrons and passes a direct current to the anode. For a total reaction, the anode is dissolved at a rate that is equal to the rate at which the cathode is plated. Therefore, the ions in the electrolyte are continuously replenished by the anode. Some electrodeposition processes use anon-consumable anode such as lead and therefore ions to be plated need to be replenished in the bath periodically.

2.1.2 Meniscus-confined electrodeposition

Meniscus-confined electrodeposition, which entails materials electrochemically via a confined meniscus (*85*), has been developed to produce high aspect-ratio micro and nano 3-D structures that can be used in wide variety of applications such as AFM imaging in liquids (*86*), direct-write of wire bonds (*87*), and potentially electrophysiological applications (*88, 89*).

Figure 13 shows the schematically setup of the meniscus-confined electrodeposition. The working principle is based on the electrodeposition. However, except for immersing the substrate into a tank of the electrolyte, meniscus-confined electrodeposition uses a micro-/nano- pipette that filled with the electrolyte to defined features. An electrode was placed within the electrolyte to complete the electrochemical reaction during the process. When the pipette is in contact with a substrate, meniscus forms between a nozzle and a substrate. Such meniscus confines the electrolyte and thus, the electrodeposition when a bias was applied between the substrate and the electrode. During the process, a nanopositioning system that moves in XYZ was used to control the movement of the micropipette. The rate of the movement of the micropipette is synchronized with the rate of the electrodeposition to realize high-precision manufacturing. Because of high-precision 3D movement, 3D structures were fabricated with complex shapes. After fabrication, the bias between the electrode and the substrate was terminated before pulling up the micro pipette to break the meniscus.

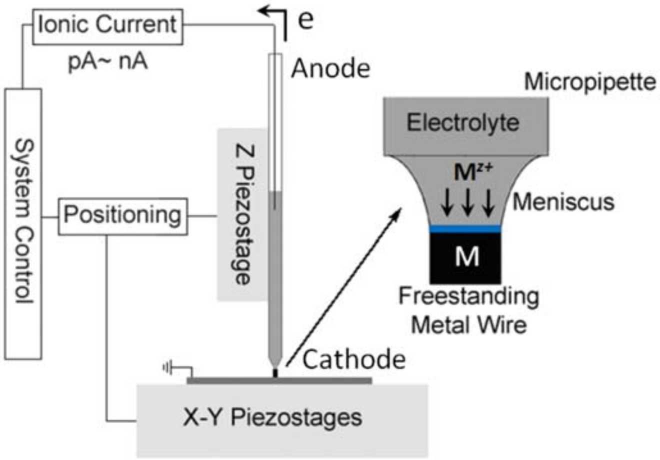

Figure 13. Schematic diagram of the meniscus-confined electrodeposition (From (*87*))

Although many complex structures can be constructed using meniscus-confined electrodeposition(*85, 87, 90-92*), previous demonstrations of the production efficiency of such technique are limited to serial process only.

2.1.3 Electrochemistry in meniscus-confined electrodeposition

In the meniscus-confined electrodeposition, by selecting different combinations such as electrolyte, electrodes, the applied potential, the presence of the additives, and so on, a wide variety of metal materials can be reduced, including gold, silver, nickel, cobalt, tin, etc. In this study, to illustrate the performance for the proposed method two types of materials were studied, copper (Cu) and platinum (Pt), that are widely applied in the electronics industry.

The effect of deposition potential on the deposition process can be studied using an analysis technique, cyclic voltammetry (CV) (*93, 94*). The cyclic voltammetry has widely used to understand the complex nature of electrochemical reactions take place at electrodes. A CV plot is obtained by plotting the current flowing through the electrochemical cell with respect to the applied potential as the potential is cycled between two limiting values at a constant sweeping rate. As the potential changes continuously in a CV experiment, the charging current due to the double layer capacitance is always present and the net current is a sum of the faradaic current and the charging current. Since it is difficult to estimate the charging current, any quantitative data obtained from the peaks in a CV plot such as concentration of reactive species or rate constants may not be reliable. But the CV plot is a powerful tool for a qualitative evaluation of the electrochemical process as it provides essential information of a reaction such as the metal deposition, the hydrogen evolution and so on, which can be obtained from the onset and peak potentials in CV plots. The deposition potential for obtaining a smooth, non-porous metal deposit can be chosen by analyzing the CV plots. The cathodic reduction process for copper and platinum deposition can be directly examined with in situ CV.

Figure 14 (A) shows a typical CV plot obtained in meniscus-confined electrodeposition using a micropipette with 10μm in diameter that is filled with 5mM H_2PtCl_6 solution and a platinum reference electrode. The potential scan rate for all the CV experiments were fixed at 100mV/s and the potential was swept with an increment of 1mV. Peaks shown in Figure 14 at C_1 and C_2 indicate the reactions Pt^{4+} to Pt^{2+} and Pt^{4+}/Pt^{2+} to Pt, respectively. As the potential increases further, the reduction current continues to rise due to the reduction of platinum ions as well as hydrogen ions (*95-98*).

Figure 14 (B) shows the CV plot for a 5 mM $CuSO_4$ solution with an Ag/AgCl reference electrode. The cathodic reduction and oxidation peaks are clearly seen at –0.4V and 0.03V, respectively. The deposition potential is chosen such that it is above the cathodic reduction potential but below the hydrogen evolution potential. When the deposition potential is above the hydrogen evolution potential, the significant hydrogen bubble formation can agitate the meniscus and prevent stable deposition of metal wires, which results in a highly porous wire structure (*98*) instead of a solid and smooth wire structure when hydrogen is not co-deposited with copper atoms as shown in inserted image.

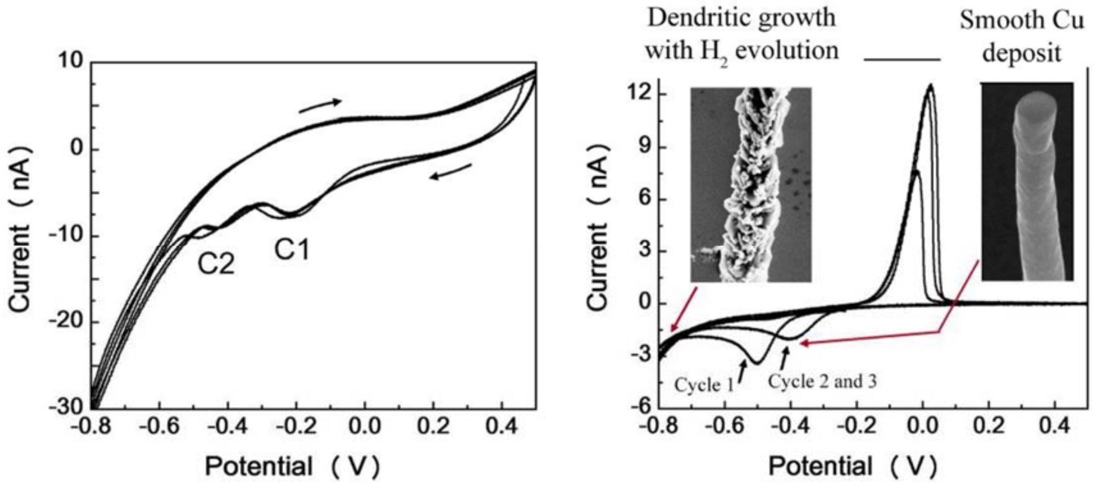

Figure 14. (a) Cyclic voltammetry plot acquired for 5 mM H_2PtCl_6 (pH = 1) with respect to a platinum reference electrode at a scan rate of 100 mV/s. (b) Cyclic voltammetry plot acquired in meniscus-confined electrodepotision with 5mM $CuSO_4$ (pH = 1) with respect to a Ag/AgCl reference electrode at a scan rate of 100 mV/s (From (*95*) by A. P. Suryavanshi).

2.2 Meniscus-Confined Electrodeposition System

2.2.1 System overview

In this study, the meniscus-confined electrodeposition process was automated using the computer-controlled system. The system consists of several subsystems such as motion control system, current measurement system, humidity control system, pressure control system, and visualization systems. All subsystems and the whole setup are connected to a computer and controlled by a series of programs written in Visual C++.

2.2.2 Motion control system

The motion control subsystem consists of two motorized stages and two piezo-stages. Two motorized stages were used to control the coarse motion and perform coarse positioning, whereas two high-precision piezo-stages were used to control the fine motion of the microstructure fabrication. Before been connected to the computer, all stages are connected through their own controllers.

Two DC motors were used to drive coarse motion control: one in Z axis and one in XY. The Z stage (model LS-50, Applied Scientific Instrumentation, Inc.) has a travel range of 50 mm with a resolution of 200 nm; the XY stage (model ms-2000, Applied Scientific Instrumentation, Inc.) has a travel range of 100 mm in both X and Y with a resolution of 220 nm.

Two nanopositioning stages were used to control ultra-fine motion in an effort to realize high precision 3D structure fabrication. A PIMars XYZ piezo-nanopositioning system (Model P563.3CD, PI) that has 300 μm closed loop travel was used for fabrication of structures smaller than the travel range. The open- and closed-loop resolutions of the PIMars are 0.5 nm and 2 nm, respectively. Another untra-long range high-resolution stage (model N-664, PI) that moves in Z direction is used when fabricating ultra-high aspect-ratio structures. The long-range high-resolution translation stage has a 30 mm travel range with 0.5 nm closed-loop resolution. Overall, when combined with two high-precision a nanopositioning stages, structures ultrahigh features and 300 μmin width and length can be fabricated, which is far exceed most engineering applications requirements of the meniscus-confined electrodeposition.

2.2.3 Current measurement system

The working principle of the meniscus-confined electrodeposition, as discussed, is based on the electrodeposition, therefore the growth current during the process needs to be monitored to ensure the deposition quality. In addition, the current while a pipette searching for a substrate as a result of establishing the electrical contact was detected. In this study, a constant voltage between a cathode and an anode was usually applied. The input voltage terminal is connected to the digital-to-analogy port of NI Data Acquisition Card PCI6711 to provide the voltage for electrodeposition.

Since the applied potential directly affects the charge transfer reaction at the electrode/electrolyte interface, the optimal potential has to be carefully chosen by using the cyclic voltammetry (CV) technique (*93, 94*). During the experiment, the current profile was measure by a NI USB DAQ card (USB9162) that is connected to a low noise current amplifier (model DLPCA-200, FEMTO). The current amplifier has variable gains that allows selections of difference current detection range corresponds to different applications, which the gain setting is from 10^3 to 10^9.

2.2.4 Pressure control system

When necessary, an external backside pressure can be applied to the electrolyte reservoir. If the curvature of electrolyte at the pipette front is concave, which prevents a micro-pipette from forming a meniscus between the nozzle and the substrate, the backside pressure allows the electrolyte in the micro-pipette to form a protruding liquid front. This is particularly important when a nozzle with diameter over 15 μm.

To control the pressure during the process, a pressure regulator that connects to a nitrogen tank was used, while the pressure was controlled manually with a digital pressure gauge. Before the pressure enters the electrolyte reservoir, a three-way solenoid valve was also used to switch the backside pressure on and off. The solenoid valve is activated by the NI USB DAQ card (USB9162) that connects to the computer so the pressure control is integrated into the control program for system automation.

2.2.5 Humidity control system

The relative humidity of the environment is a dominant parameter in the meniscus-confined electrodeposition system that determines the growth rate and growth quality of the deposition. Without proper control of the experimental enclosure, the evaporation of the electrolyte from the meniscus at the deposition interface, due to the exposure, will disturb the continuous wire growth.

For a serial process performed with a single pipette, the relative humidity of the environment is maintained at around 50% as a low relative humidity will result in pipette clogs and a high relative humidity will degrade the rate and quality of the deposition. Further, when performing the array-based meniscus-confined electrodeposition, which will be discussed later, the realization of the array growth system is sensitive to the environmental humidity control. In short, to achieve the high quality and uniformity array growth, the uniform humidity across an entire nozzle array needs to be accomplished.

The enclosure of the experimental setup is sealed from atmosphere. The desired humidity of the enclosure is obtained by bubbling dry air through a bottle of DI water with various rate before entering the enclosure (*99, 100*). The flow rate of the air was controlled using a precision needle valve to maintain the desired humidity and compensate for any leakage in the system. Although this type of humidity control is relatively local, relatively even distribution of vapor can be obtained within the small enclosure. Further, all the electrical components were isolated from the humid air to avoid damage due to exposure of high humidity environment. To guarantee the accurate measurement of the relative humidity during the deposition, a humidity sensor was installed close to the deposition point.

2.3 Summary

In this chapter, the basic concept of the meniscus-confined electrodeposition was introduced. Details of experimental setup for the meniscus-confined electrodeposition were described, including subsystems such as motion control system, current measurement system, pressure control system and humidity control system.

CHAPTER 3

THEORY DEVELOPMENT OF THE SELF-REGULATED PARALLEL MANUFACTURING PROCESS

3.1 Introduction

In an electrodeposition system in which mass transfer is the rate-determining process, deposition rate is mainly governed by the time for transporting ions to the reaction interface via migration, diffusion and/or convection (*94*). Since the electrochemical reaction involved in this study is fast when compared to mass transport, I analyze the system using diffusion-limited model. As a result, how rapid and how uniform ions transport to the deposition interface becomes critical to ensure the uniform deposition. In addition to the typical mechanisms governing electrodeposition in an unstirred electrochemical deposition setup, evaporation plays an important role in our meniscus-confined deposition system (*91*), where evaporation from the meniscus drives electrolyte to flow and carries ions towards deposition surface.

The objective of this study is to realize the array-based fabrication via a nozzle array system. To realize the array-based fabrication, adequate conditions for the uniform array growth need to be found when taking into account of the balance among evaporation, ion-transport, and stability of meniscus for every nozzle.

3.2 Self-Regulated Electrodeposition Mechanism

For the nozzle array based electrodeposition, how rapid and uniform ions transport through every nozzle determines if synchronized metal wire array growth can be realized. Two major issues related to the uniform transport of ions through every nozzle channels during array-based electrodeposition are schematically depicted in Figure 15. One is the uniformity of evaporation around the exposed menisci between each nozzle end and the corresponding growth front of metal wires, the other is the uniformity of the ion transport over the back openings of nozzle channels.

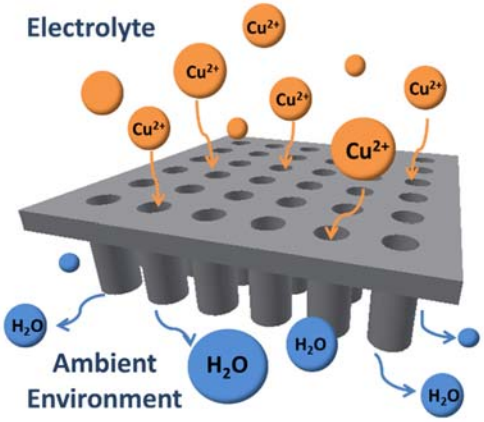

Figure 15. Issues related to uniform ion transport in the array-based fabrication: ion transport through the nozzles and evaporation at nozzle openings

3.2.1 Effect of evaporation

In contrast to a typical electrodeposition system in which the deposition takes place in a submersed electrolyte environment, the meniscus-confined electrodeposition system involves a liquid/air interface where the evaporation of water from the electrolyte in the microscopic sized meniscus dynamically modulate the ion concentration of the electrolyte in the meniscus and affects the diffusion zone development at the growth front of metal and thus the deposition rate of the metal wire (*91*).

3.2.1.1 Relative humidity

Because evaporation from meniscus is a diffusion process driven by the concentration gradient of water molecules in the ambient environment, a lower ambient relative humidity will result in a higher concentration gradient, thus a higher deposition rate. In our evaporation-assisted deposition system, the relative humidity in the vicinity of each nozzle needs to be kept uniform across the nozzle array in order to maintain consistent deposition rate for different nozzles.

Intrinsically, this uniformity of evaporation can be maintained if a nozzle array has a large nozzle-to-nozzle spacing so that the diffusion resistance for water from the inner nozzles is relatively small, or if the nozzle array is simply a small array, e.g. a 2 by 2 array, in which the diffusion conditions would then be identical for each nozzle. However, for high density nozzle arrays having small lateral spacing and large array sizes, water molecules become more difficult to diffuse out from inner nozzles to ambient environment compare to from marginal nozzles. The rate of metal electrodeposition under the marginal nozzles would therefore be higher than that under the inner nozzles, creating non-uniform electrodeposition rates across the nozzle array that prevents the array-based uniform deposition.

In an effort to eliminate the non-uniform deposition rate due to the non-uniform evaporation rate across the nozzle array, Finite element modeling was applied to study how ambient humidity and nozzle-to-nozzle spacing affect the water evaporation across high density nozzle arrays.

3.2.1.2 Finite element modeling

The evaporation of water from meniscus was simulated with finite element analysis using a 2-D diffusion model in COMSOL Multiphysics. Two 9 × 9 nozzle arrays are considered, one having the array spacing-to-diameter ratio (SR) of 2 and the other of 20, which simulates a high-density array (SR=2) and a low-density array

(SR=20). The diameter of a nozzle opening is set to be 30 μm, as same as the diameter of the nozzle used in experiment. In both simulations, Dirichlet boundary conditions (B.C.s) are used at domain boundaries and nozzle openings. Ambient relative humidity is varied from 70% to 100% at domain boundaries and the humidity along the nozzle opening is fixed at 100%, which reflects the saturation condition right at water/air interface. To reduce the computational time, Neumann boundary conditions are imposed along the center line of the nozzle array to account for the symmetric nature of the problem. Figure 16 shows a representative mesh fora high density array having a nozzle spacing to diameter ratio of 2. To capture the more detailed variation near the nozzle area, fine meshed are designed around the nozzle openings while coarse meshes are applied to the ambient environment.

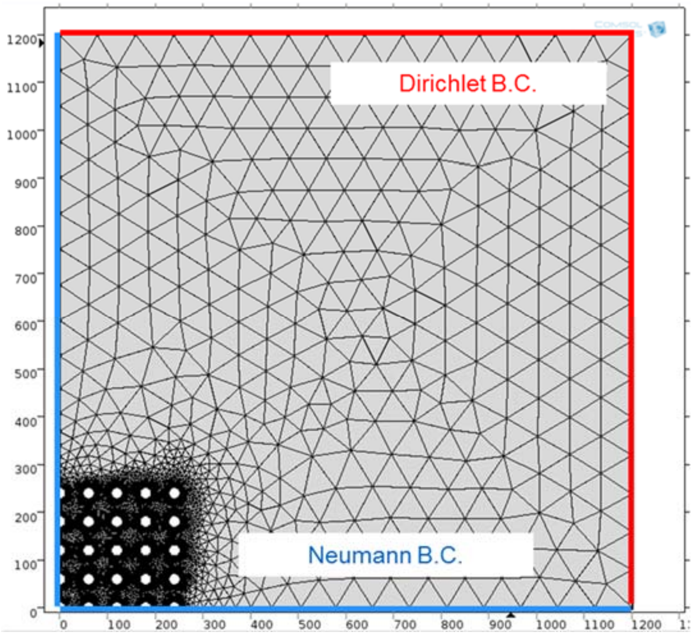

Figure 16. Domain, mesh, and boundary conditions created for a high-density nozzle array (SR=2) in the finite element simulation. Units in both axis are microns.

Figure 17 shows the color scale representation of the water concentration over the high-density nozzle array (with SR=2) when the ambient humidity is set at 70%. The humidity distribution is shown to be fairly uniform within the nozzle array and is at its saturation of 0.944 mol/m^3.

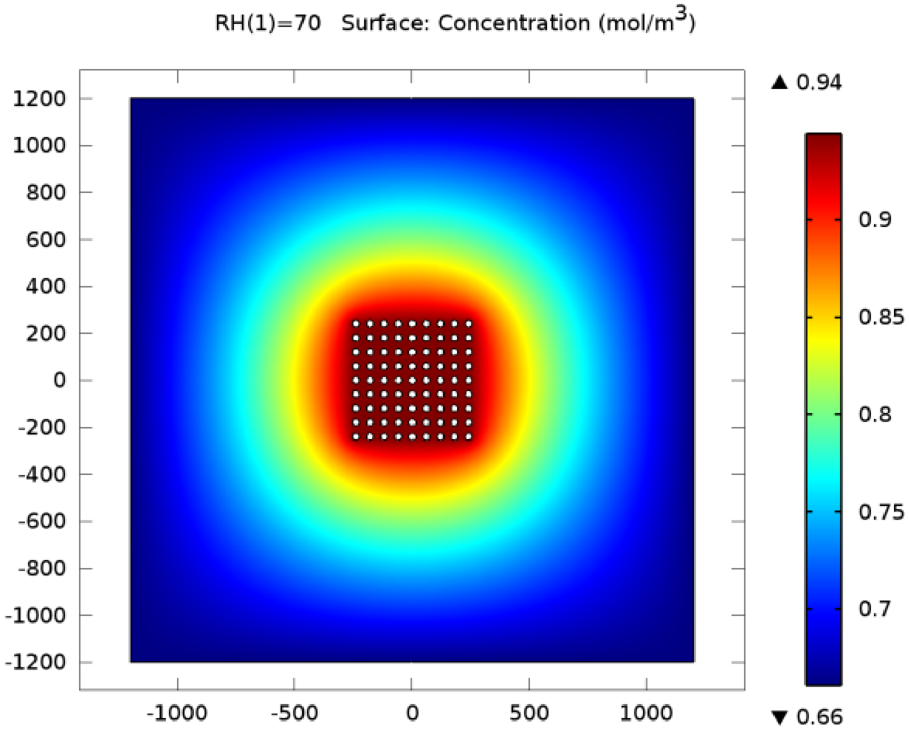

Figure 17: Relative humidity distribution over a 9 × 9 array of nozzle opening filled with water when the surrounding relative humidity is at 70%, simulated with a 2-D diffusion model. The nozzle array has array spacing to diameter ratio (SR) of 2 and a nozzle diameter of 30 µm.

The line profile of the humidity distribution along the middle row of the nozzles in Figure 18 exhibits this uniformity more clearly, where the water concentration begins to drop only outside the nozzle array.

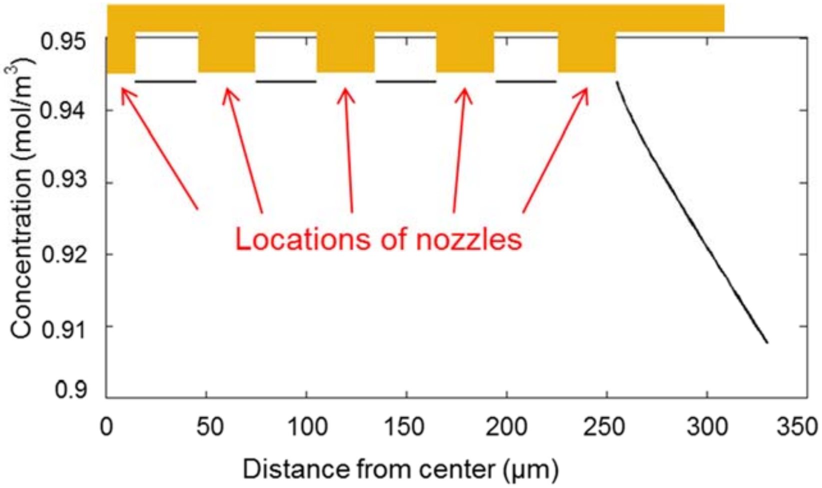

Figure 18: Line plot showing the relative humidity distribution across the middle row of a 9 × 9 array of nozzle opening filled with water when the surrounding relative humidity is at 70%. The nozzle array has array spacing to diameter ratio (SR) of 2 and a nozzle diameter of 30 µm. An orange block diagram is overlaid on the plot to show the nozzle locations in the array.

Figure 19 shows the humidity distribution at the ambient relative humidity of 70% over the array with a spacing-to-diameter ratio of 20, in which a similar uniformity is observed within the nozzle array. Although slightly variation over the first two rows of the nozzles is observed, the variation reduces quickly and becomes homogeneous after the first two rows. Besides, the water concentration deviates from the saturation within the array is still near 0.94 mol/m^3 even towards the peripheral nozzle.

The highest concentration gradient, as expected, occurs at the nozzles around the very edge of the array, as shown in both Figure 18 and Figure 19. Here the concentration profile of two configurations were compared at an inter-nozzle spacing away from the array, which are 0.928 mol/m^3 for SR=2 and 0.91 mol/m^3 for SR=20. Although Figure 18 shows the water concentration drops slightly around the outmost layer of nozzles for a high density array, from 0.944 mol/m^3 to 0.928 mol/m^3 (1.7% drop) when the ambient humidity is set to be 70%. The difference is more obvious for a low-density array, shown in Figure 19, the water concentration deviates from the relatively uniform distribution of around 0.944 mol/m^3 to 0.91 mol/m^3 (3.6% drop) over the marginal nozzles. This difference in concentration gradient results in different rate of ion transport that eventually disrupts array-based deposition. (also, evaporation rate is determined by the concentration gradient, thus the slope of the concentration drop. Quoting the concentration value near the nozzle is not relevant. Better extract some gradient values for comparison)

To eliminate the concentration gradient difference between marginal nozzles and inner nozzles, the ambient humidity is set at over 90%. As a result, more uniform distribution with less variation can be realized over the whole nozzle array. In the following experimental studies, a constant relative humidity over 95% around the nozzle array was always provided for the array-based electrodeposition.

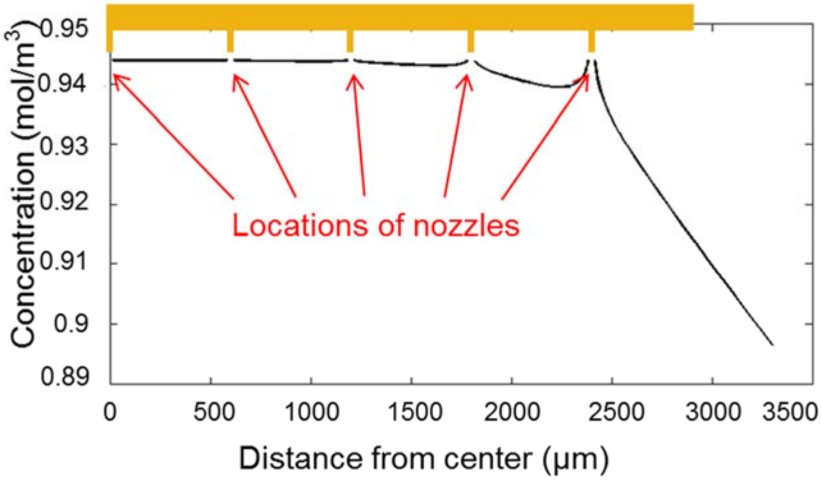

Figure 19. Line plot showing the relative humidity distribution across the middle row of a 9 × 9 array of nozzle opening filled with water when the surrounding relative humidity is at 70%. The nozzle array has an array spacing to diameter ratio (SR) of 20.

3.2.1.3 Summary

In this section, difference in the deposition rate caused by evaporation was discussed. To account for the effect, numerical simulation of 2-D diffusion of water molecules between meniscus and ambient environment was carried out using COMSOL Multiphysics finite element analysis software. The simulated water concentration distribution revealed that the concentration distribution in a large high density nozzle array was quite homogeneous within the inner nozzles beyond the first two marginal rows of nozzles. However, to eliminate any significant difference in evaporation due to the concentration gradient difference around the marginal nozzles and the inner nozzles setting an ambient environment with a high relative humidity above 95% is recommended for the array based parallel process fabrication.

3.2.2 Effects of the nozzle geometry

3.2.2.1 Diffusion zone overlap

Considering a single nozzle filled with electrolyte performing electrodeposition at the end opening of the nozzle, the metal ion concentration at the back opening of the nozzle is lower than the bulk concentration of the same metal ion established far away from the back opening. In between, a hemispherical diffusion zone exists that establishes the balance of ion flux required to flow into the nozzle channel and being depleted at the reduction interface at the end opening of the nozzle (Figure 20 (A)). This diffusion zone development into the bulk solution is determined only by the size the back opening of the nozzle, the ion flux through the channel and the bulk concentration of the electrolyte. On the other hand, for an array of nozzles filled with electrolyte performing the array based electrodeposition as shown in Figure 20 (B), the diffusion zone development above each back opening of the nozzle is expected to be influenced by the corresponding development over the neighboring nozzles. Depending on the nozzle spacing, the nozzle size and the concentration of the ions, there exists the possibility of the diffusion zone overlapping that would limit the amount of ion flux going into each nozzle channels (*101-106*). For array-based electrodeposition, such a diffusion zone overlapping and its effect on the rate of metal electrodeposition needs to be analyzed.

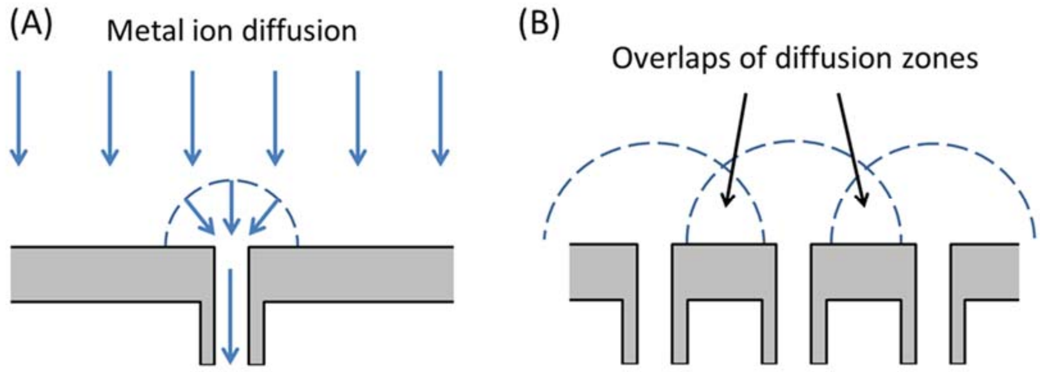

Figure 20. Diffusion zone development above (A) a single nozzle and (B) an array of nozzles

Further taking into consideration of the finite size of the nozzle array and thus the difference in diffusion zone development over the back openings of the inner nozzles and the peripheral nozzles, there exists also a potential non-homogeneous ion flux distribution across the nozzle array. In the following, such an ion flux distribution over a finite-sized nozzle array is analyzed.

The difference in diffusion zone development occurs most pronounced between the peripheral nozzle openings and the inner nozzle openings: while peripheral nozzles have less neighboring nozzles and allow more diffusion zone development into the bulk electrolyte (*104*). As a result, biased at the same electrical potential for the electrodeposition, there occurs higher diffusion-limited current through the marginal nozzles than that through the inner nozzles. The difference makes it infeasible to sustain continuous co-growth of metal wires across the whole nozzle array.

The difference between marginal nozzles and center nozzles, however, can be alleviated by the proper design of the nozzles with certain finite channel lengths. To find a condition that realizes uniform co-growth of the entire array, the diffusion-limited current is analyzed by converting an inlaid disc electrode array related diffusion problem into a recessed-disc electrode array problem.

3.2.2.2 Model development

The development of diffusion zones over back openings of the nozzle array is modelled according to Figure 21, which shows the geometry for the diffusion model consideration of the nozzle array, where L, d, r, δ, are length of the nozzle, array spacing of the nozzles, inner radius of the nozzle, and Nernstian diffusion thickness, respectively.

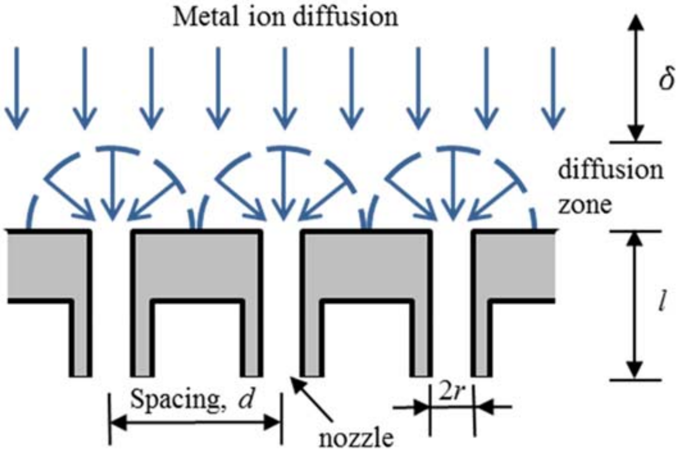

Figure 21: Schematic showing the geometric layout of a nozzle array and the diffusion zones for the model analysis

The ion current through a nozzle array is considered in two serial steps, one involves a planar diffusion from the bulk solution to an imaginary boundary plane, and the other involves a hemispherical diffusion from that imaginary boundary plane to the nozzle opening, as shown in Figure 21. In the analysis, nozzle openings are equivalent to electrodes in the nomenclature of electrochemistry.

In the derivation, the consideration of the effect of convection, and the transition from planar diffusion to hemispherical diffusion at the initial stage of the diffusion field development are excluded. The model was thus more appropriate to describe the long-term Cottrellian behavior of the chronoamperometric response of a microelectrode array, and to quantitatively predict the electrodeposition rate occurred under each nozzle in our array-based process.

The ion flux across the imaginary boundary plane is:

$$\frac{dn}{dt} = DA(c_b - c_i)/\delta \tag{2}$$

Where $c_\mathrm{b}$and c_i are the ion concentratio *n* in the bulk solution and at the imaginary plane, respectively, *D* is the diffusion coefficient of the ion, and *A* is the total area of the array. *δ* is the Nernstian diffusion thickness and is defined as $\delta = \sqrt{\pi D t}$, which increases with time t.

The ion flux related to the hemispherical diffusion towards the nozzle opening is described by considering the steady state current for recessed disc electrodes. The steady state current for a recessed disc can be found in (107):

$$I_{ss} = zFDrc\left[\frac{4\pi r}{\pi r + 4L}\right] \tag{3}$$

Where *z* is charging number of the ion, *F* is the Faraday constant, *r* is the nozzle diameter, *L* is the nozzle length and *c* is the bulk concentration of electrolyte.

Using this equation, the ion flux related to the hemispherical diffusion can be written as:

$$\frac{dn}{dt}=\frac{I}{zF}=NI_{ss}/z \;=\; NDrc_i\left(\frac{4\pi r}{\pi r+4L}\right) \tag{4}$$

As the ion flux is continuous through the imaginary boundary, the following equation is derived:

$$I=\frac{zFGA(c_b-c_i)}{\delta} \tag{5}$$

By eliminating c_i, it becomes:

$$\frac{1}{I}=\frac{1}{\left[\frac{4\pi r}{\pi r+4L}\right]xzFDrc}+\frac{\delta}{zFDAc} \tag{6}$$

To consider the current of an individual nozzle, $i = I/N$, where N is total number of nuzzle, the current for an individual nozzle is then:

$$\frac{1}{i}=\frac{1}{zFDrc_{b\left(\frac{4\pi r}{\pi r+4L}\right)}}+\frac{N\delta}{zFDAc_b} \tag{7}$$

The equation is non-dimensionalized by normalizing the current with the steady state current of an in-laid disc electrode (*94, 107*), $i_{ss,id}$, which is the diffusion-limited current that can be acquired by an electrode:

$$i^*=\frac{i}{i_{SS,id}}=\frac{i}{4zFDRc_b} \tag{8}$$

So

$$\frac{1}{i^*}=\frac{1}{\left(\frac{\pi r}{\pi r+4L}\right)}+\frac{4N\delta r}{A} \tag{9}$$

For an $n\times n$ square nozzle array with uniform nozzle distribution, $N=n^2$, and $A=(n\cdot d)^2$, so

$$\frac{1}{i^*} = \left(1 + \frac{4L}{\pi r}\right) + \frac{4r\sqrt{\pi D t}}{d^2} \tag{10}$$

Setting the aspect-ratio of nozzle to be $AR = L/2r$ and the array spacing to diameter ratio to be $SR = d/2r$ leads to:

$$\frac{1}{i^*} = \left(1 + \frac{8}{\pi} AR\right) + \frac{2\sqrt{\pi D t}}{d} \frac{1}{SR} \tag{11}$$

Further introducing a non-dimensional time $t^* = \frac{Dt}{r^2}$, which is the mass-transfer Fourier number, a dimensionless governing equation is finalized:

$$\frac{1}{i^*} = \left(1 + \frac{8}{\pi} AR\right) + \sqrt{\pi t^*} \frac{1}{SR^2} \tag{12}$$

The equation consists of two parts, one is the time-invariant part in the bracket containing hemispherical diffusion resistance of an individual nozzle that depends on the nozzle geometry AR, and the other is the time-variant part involving the diffusion resistance due to the overlaps of diffusion zones between neighboring nozzles that depends on the array parameter *SR*. In other words, the first part of the equation comes from the nozzle itself and the second part quantifies the effects from neighboring nozzles.

The equation can be better understood from the following analysis of two simple cases. In the case of t* and AR both being 0, the equation is simplified down to $i = 4zFDrc$, which is basic the classical steady state current for an inlaid disc electrode. In the case of t* being 0 and AR being of an arbitrary value, the equation is reduced to $i^* = \frac{\pi r}{\pi r + 4L}$, or converting to the dimensional form, $i = zFDrc\left[\frac{4\pi r}{\pi r + 4L}\right]$, which is again another classical steady state current for a recessed disc electrode. The inclusion of the time variant term in the equation means that as time increases, this term will dominate the overall contribution to the current, and thus elevates the importance of the parameter SR related to the neighboring arrangement of the nozzles, while the parameter AR, which is the aspect-ratio of the nozzle itself is more important in the the initial current response.

3.2.2.3 Nozzle array design considerations

The non-dimensionalized equation, Eq. 11, generalizes the relationship between the ionic current through each individual nozzle and the relevant geometric dimensions of the nozzle array. In the following, it is applied to guide the design of the nozzle array for the parallel process electrodeposition.

The objective of finding an optimal geometry for the nozzle array is to have identical or minimal differences in ionic current between peripheral and inner nozzles, so that the synchronized array growth of high quality metal wires under every nozzles can be realized. Over the peripheral nozzles, due to the lack of neighboring nozzles thus the immediate accessibility of bulk electrolyte, the diffusion zone development is much less affected by the diffusion zone overlapping. In the following discussion, the ionic current through peripheral nozzle is assumed to be non-variant over time and takes a fixed value defined in Eq. 11 at $t^* = 0$. It is then compared with the ionic current through the inner nozzles, and the dependence of their difference on the nozzle dimensions is developed.

The dependence of ionic current with respect to the array spacing to nozzle diameter ratio (*SR*) is shown in Figure 22 according to Eq. 11 by setting the nozzle aspect-ratio to be zero. The nozzle array in this case is essentially an inlaid disc electrode array. The array based electrodeposition system typically reaches steady state in about 45 seconds according to our experimental observation, which is equivalent to a dimensionless time $t^* = \frac{Dt}{r^2} \sim 167$. Plots are thus developed in the following for t^* from 0 up to 200.

Figure 22 shows that the ionic current through the inner nozzles increases with the increase of SR (i.e. the increase of the array spacing), meaning that increasing the array density (with a fixed nozzle diameter) promotes the development of diffusion zone overlapping and reduces the ionic current available through the inner nozzles for electrodeposition.

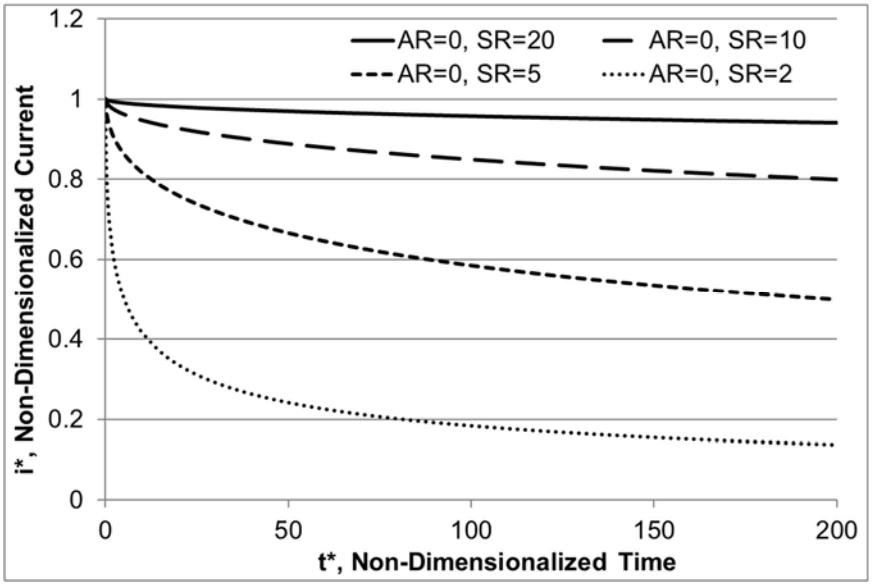

Figure 22. The dependence of ionic current over time in a nozzle array on array-spacing to diameter ratio (SR)

It also shows that with increasing array spacing to nozzle diameter ratio, the ionic current through the inner nozzle stabilizes towards a current only somewhat smaller than the initiation current. As the initiation current at t =0 is approximated as the current through the peripheral nozzle and is assumed to be not affected by the development of diffusion overlap, the plot essentially shows that with the increasing array spacing to nozzle diameter ratio, the difference in ionic current between through the inner nozzle and through the peripheral nozzle reduces, a condition that is beneficial for uniform wire growth across the whole array for the nozzle array-based parallel process. In the case of a very high SR, diffusion zone over the nozzle back opening develops independently from each other without significant overlapping effect.

Although increasing the SR provides a more uniform current response in the nozzle array, the density of the wire array to be fabricated would decrease, which is not desirable. For example, to keep the ionic current through the inner nozzle to be within 80% of the current through the peripheral nozzle, the SR needs to be greater than 10, meaning the nozzle spacing needs to be larger than 200 µm for growing array wires of diameter of 20 µm.

An alternative way to regulate the diffusion zone overlapping is to control the aspect-ratio (AR) of the nozzles in a nozzle array. The dependence of ionic current with respect to nozzle aspect-ratio is plotted in Figure 33, with the array spacing-to-diameter ratio fix at 2.

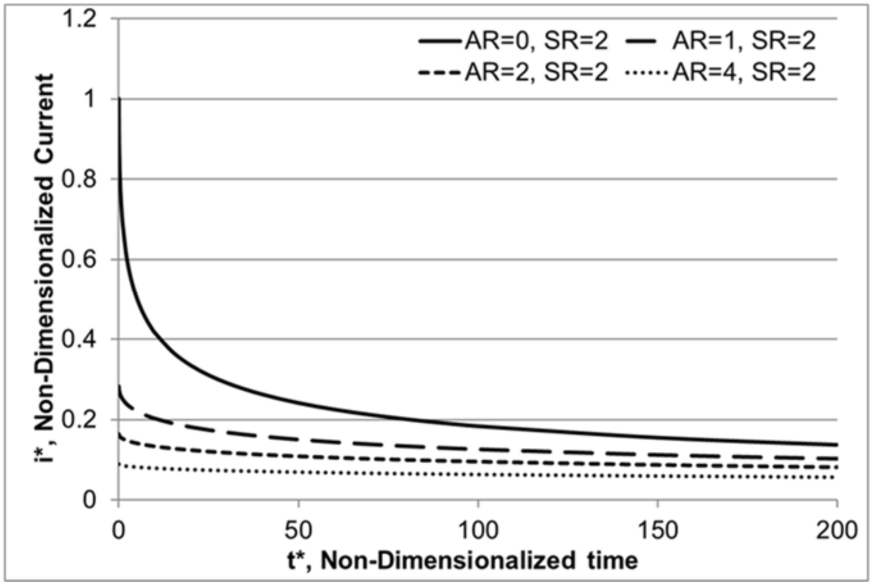

Figure 23. The development of ionic current over time in a nozzle array having different nozzle aspect-ratio (AR) and a fixed array-spacing to diameter ratio of 2.

As shown in Figure 23, increasing the aspect-ratio of the nozzle decreases the diffusion limited current through such nozzles and has the effect of minimizing the size of the diffusion zone over the nozzle and thus minimizes the effect of diffusion zone overlapping between the nozzles. It is much clearer when the actual values are compared between the stabilized ionic current through the inner nozzle and the ionic current through the peripheral nozzle (i.e. the initiating current) for a fixed $SR = 2$: $AR = 0$, $i^* = 13.8\% i^*_{\text{ini}}$; $AR = 1$, $i^* = 36.1\% i^*_{\text{ini}}$; $AR = 2$, $i^* = 49.3\% \mathrm{i}^*_{\text{ini}}$; $\mathrm{AR}=4$, $\mathrm{i}^* = 64.1\% \mathrm{i}^*_{\text{ini}}$. It shows that increasing AR is very effective in reducing the current difference between peripheral nozzles and inner nozzles while preserving the potential for high-density ($SR = 2$) array wire growth. The downside is that increasing AR decreases the overall diffusion limited ionic current through the nozzle array: $AR = 0$, $i_{\text{ini}}^* = 100\% i^*_{\text{inlaid disc}}$; $AR = 1$, $i_{\text{ini}}^* = 28.2\% i^*_{\text{inlaid disc}}$; $AR = 2$, $i_{\text{ini}}^* = 16.4\% i^*_{\text{inlaid disc}}$; $AR = 4$, $i_{\text{ini}}^* = 7.3\% i^*_{\text{inlaid disc}}$. This has the potential to lower the growth rate of the array wire. However, this can be sufficiently compensated by the potential to realizing the parallel process fabrication of a large array of metal wires. As the ionic current non-uniformity is caused mainly by the first few rows of peripheral nozzles in a nozzle array due to either the humidity effect or the diffusion zone overlap effect regardless of how large the nozzle array is, high throughput fabrication with the use of a high area density and large nozzle array is indeed possible.

3.2.2.4 Summary

In general, increasing the array spacing to nozzle diameter ratio (SR) reduces the diffusion zone overlapping between neighboring nozzles and minimizes the difference in diffusion zone development between over the peripheral nozzles and over the inner nozzles. However, increasing the array spacing-to-diameter ratio (SR) limits the development of high-density metal wire arrays. On the other hand, increasing the aspect-ratio (*AR*) of the nozzle minimizes the diffusion zone overlapping between neighboring nozzles but reduces the overall ionic current through the nozzle, thus lowers the electrodeposition rate of metal wire.

The design of the nozzle array for realizing the sustained parallel process electrodeposition of metal wire array needs thus consider the trade-off between the spacing-to-diameter ratio (*SR*) and the nozzle aspect-ratio (*AR*) in order to manage both the need for electrodeposition uniformity across the whole array and the need for acquiring sufficiently high electrodeposition rate for fabricating metal wire arrays within a reasonably short amount of time.

However, the management of the ionic current uniformity alone through nozzle array design is essential, but not sufficient, for realizing the parallel process array fabrication. This can be explained in the following discussion. The current responses in a peripheral nozzle and an inner nozzle are plotted against the nozzle aspect-ratio *AR*, as shown in Figure 24, for the nozzles in a high-density nozzle array of *SR* = 2. Unfortunately, an equal ionic current that would allow the growth of metal wires under the inner nozzle and the peripheral nozzle at the same growth rate does not exist. In other words, through the humidity control and the design of nozzle geometry are not enough to create continuous co-growth conditions. Further consideration of meniscus stability is required in order to seek conditions for successful parallel process co-growth of wire arrays, as discussed in the following.

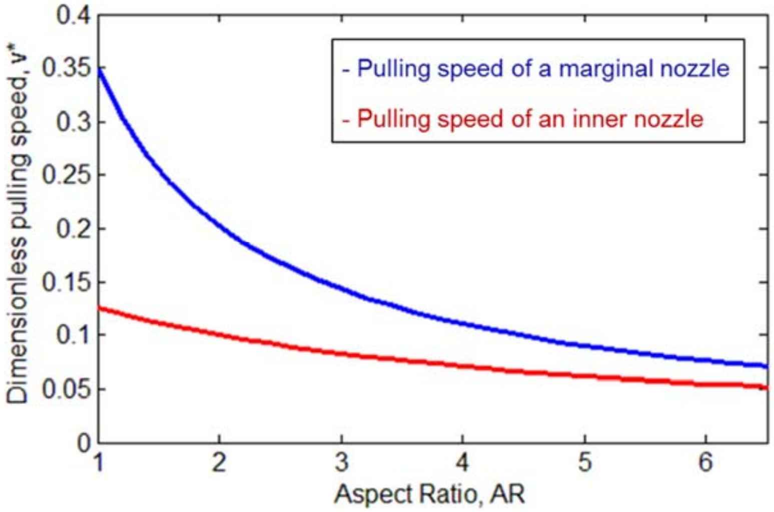

Figure 24. Growth rate dependence of electrodeposition on the nozzle aspect-ratio under a peripheral nozzle and an inner nozzle

3.2.3 Stability of the meniscus

3.2.3.1 Creating co-growth conditions

To keep the deposition condition the same under each nozzle in a nozzle array, some practical issues presented in the array-based fabrication system need to be overcome such as evaporation and the nozzle geometry. The effect of the evaporation can be minimized through humidity control as discussed above, however, the difference in diffusion-limited current between through the peripheral nozzles and through the inner nozzles, while can be minimized by design, cannot be theoretically eliminated. Here the stability of meniscus that is capable of regulating the wire growth rate during the electrodeposition process is discussed in order to find a common parameter window for realizing the co-growth in the nozzle array based fabrication.

3.2.3.2 Parameter window stability for realizing synchronized co-growth of metal array wires

A meniscus exists under each nozzle in the nozzle array-based electrodeposition, which provides a mechanism to regulate the electrodeposition rate due to the thermodynamic stability of the meniscus. As schematically shown in Figure 25, a meniscus, within a certain limit, has the ability to be deformed into different thermodynamically stable configurations to accommodate the different gap separation between the nozzle end and the growth front of the metal wire. In case that the gap separation increases, the meniscus would be stretched more, which would reduce the waist diameter of the meniscus, and thus the diameter of the metal wire to be deposited. As the overall ionic current through the nozzle is still the same or the amount of metal to be deposited is still the same, the overall height growth rate of the metal wire would actually increase, which would then reduce the gap separation in a self-regulated process.

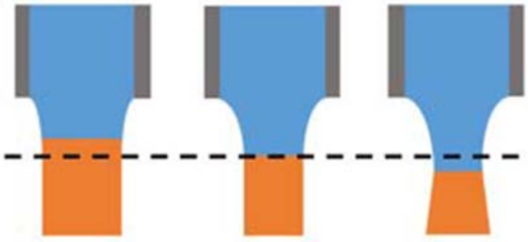

Figure 25. Meniscus regulated growth process

The thermodynamic consideration of the meniscus at the solid/liquid/air interface, known as the three-phase contact line, dictates the existence of a stable meniscus formation up to a certain meniscus height before the rupture:

$$\frac{H_M}{R_W} = \cos\varphi_0\left(\cosh^{-1}\frac{R_N}{R_W\cos\varphi_0} - \cosh^{-1}\frac{1}{\cos\varphi_0}\right) \tag{13}$$

(*108*) where H_M is the height of the meniscus, R_w is the radius of the wire, R_N is the radius of the nozzle, φ_0 is the slope of the meniscus off the growth direction at the three-phase contact line. The radius of a deposited wire, also the Kelvin radius critical for the thermodynamic stability analysis of the meniscus, is regulated by the height of the meniscus.

Analysis, confirmed by the experimental observation, shows that continuous wire deposition can be sustained as long as the radius of the deposited wire is maintained to be no less than 50% of the nozzle radius, in the case of Cu wire electrodeposition (*87*). As the maximum radius of the deposited wire cannot exceed the radius of the nozzle, the stable wire diameter in the copper-air-water system is in the range of $0.5R_N < R_W < R_N$. This is experimentally realized by selecting a nozzle withdrawal speed between a lower bound set by the speed for growing a wire having a diameter equal to the nozzle diameter R_N, when the meniscus height is zero, and an upper bound set by the speed for growing a wire having a diameter equal to 50% of the nozzle diameter, when the meniscus is stretched to its limit to keep thermodynamically stable. Since the amount of available ions is controlled, this existence of a stability window in the meniscus-confined electrodeposition is essential for realizing the synchronized and continuous co-electrodeposition of an array of metal wires.

The pulling speed of a nozzle, based on the Faraday's equation, can be written as:

$$v = \frac{MI}{zF\pi {R_N}^2 \rho} \tag{14}$$

which is predetermined by the radius of a nozzle and is inverse proportional to ${R_N}^2$. In our deposition system, the meniscus is stable within the range of $0.5R_N < R_W < R_N$, and the stable pulling speed is therefore in the range of $v \leq v_{stable} \leq 4v$. A deviation from this withdrawal speed window of stability would either cause the clogging into the nozzle or the abrupt rupture of meniscus below the nozzle. Experimentally, the stable condition of the meniscus is set to be within the range of $0.55R_N < R_W < 0.95R_N$. Including this window of stability into consideration, two lines shown in Figure 24, actually expand to two bands, as shown in Figure 26, which are the stable growth windows for corresponding nozzles. The dimensionless withdrawal speed is defined as an actual withdrawal speed divided by the withdrawal speed for growing a metal wire having the same diameter as the nozzle diameter under a nozzle having a zero aspect-ratio, defined in Eq. 13. The window of stability due to the meniscus regulated growth mechanism creates an overlapped region that would allow the synchronized co-growth of metal wires under an entire nozzle array.

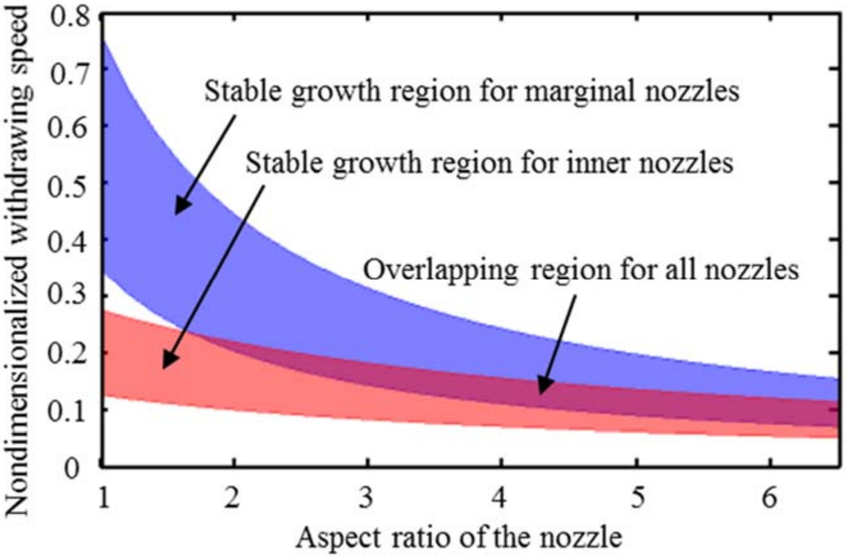

Figure 26. Overlap of the stability windows of a peripheral nozzle and an inner nozzle

As long as the variation in nozzle dimension, ionic current and the misalignment of the nozzle array with the substrate are within technically acceptable limit, a common window of stability exists, albeit a somewhat narrower one as a result of overlapping the windows of stability defined by the conditions under every nozzle. A nozzle array withdrawal speed can thus be chosen within this common window of stability to sustain the continuous co-growth of an array of metal microwires. Such an existence of self-regulation is an intrinsic feature of this meniscus confined electrodeposition, and is not available in any other existing direct-write fabrication methods (6).

3.2.3.3 Summary

Here a common window of stability was derived to sustain a continuous growth across the whole nozzle array. This condition begins to appear when the nozzle aspect-ratio is designed to be larger than about 2, as shown in Figure 26,. However, operating at this boundary condition, the peripheral nozzle would work at the lower limit of its own window of stability and thus grow a wire having a diameter close to the nozzle diameter, while the inner nozzle would work near the upper limit of its own window of stability and grow a wire having a diameter close to the half of the nozzle diameter. As discussed previously, a slight disturbance may nudge the system out of this narrow common window of stability, and disrupt the continuous co-growth of wires across the entire array. Increasing the nozzle aspect-ratio expands this common window of stability, making it possible to grow uniform diameter metal wires across the whole nozzle array, besides making the system more stable.

3.3 Summary

In this chapter, the effect of water evaporation thus the relative humidity in the environment on the nozzle array based electrodeposition was studied. It is found that providing a controlled environment at a relatively high humidity condition is essential to create a homogeneous water molecule concentration gradient throughout the narrow nozzle array/substrate interface.

The diffusion zone development in the nozzle array during electrodeposition was studied for nozzle arrays having different array spacing and nozzle aspect-ratio for the purpose of minimize the ionic current difference between through the peripheral nozzles and through the inner nozzles. The diffusion limited current through the inner nozzles was modeled by the electrochemical analysis of an infinite array of recessed microelectrodes. A non-dimensionalized governing equation was derived.

The current through the peripheral nozzle is assumed to be immune to the diffusion zone overlapping and remain constant. Accordingly, the difference in ionic current through the peripheral nozzle and through the inner nozzle was analyzed. It is found that increasing the nozzle spacing to diameter ratio *SR* or the nozzle aspect-ratio *AR* can effectively minimize such a difference. However, increasing the *SR* compromises the capability of fabricating high-density metal microwire array with this parallel process direct-write approach; while increasing an *AR* lowers the ionic current for electrodeposition (20), thus the deposition rate for the co-growth of metal microwires. In addition, it is found that the difference in ionic current between through a peripheral nozzle and through an inner nozzle cannot be completely eliminated through the nozzle design.

The self-regulated growth mechanism due to the stability of the meniscus in the nozzle-based electrodeposition was considered. It is found that a common window of stability for sustaining a continuous growth across the whole nozzle array begins to emerge when the nozzle aspect-ratio is larger than about 2, and a wider window of stability exists for the nozzle aspect-ratio between 5 and 7 for a nozzle array having a nozzle spacing to diameter ratio of 2.

Figure 27. Schematic showing the preferred nozzle array design having a nozzle aspect-ratio of 6 and a nozzle spacing-to-diameter ratio of 2

Experimentally, nozzle arrays based on what is specified in Figure 16 will be fabricated and studied in our following chapters. This design provides an overlapped zone of window of stability wide enough to make it technically feasible to realize the simultaneous growth of a high-density array of metal microwires. It also minimizes the variation in wire diameters across the whole array and achieves a reasonable growth rate for high throughput fabrication.

CHAPTER 4

DEVICE FABRICATION FOR REALIZING ARRAY-BASED MENISCUS-CONFINE ELECTRODEPOSITON

4.1 Introduction

In this chapter, a parallel process that deploys devices consists of nozzle arrays that are capable of direct-write arrays of metal wires simultaneously will be developed. It has been shown that in principle the meniscus-confined deposition is capable of array fabrication of microstructures owing to its self-regulated mechanisms discussed in the previous chapter. Although the efficiency of the array-based growth is substantially higher than that of a serial process, the array-based fabrication process requires also the use of more precisely fabricated nozzle array devices to perform the electrodeposition.

Here micromachining-based fabrication techniques are deployed to fabricate precision nozzle array devices with high yield. The development of such a fabrication process is described in this chapter.

4.2 Design Consideration of the Fabrication Process

Cost and precision of the micromachining process relies on the numbers of photomasks used for photolithography in the process, as the use of more photomasks increases the number of fabrication steps involved and the requirement for accurate alignment. To reduce the number of photomasks used in the process, self-alignment with nozzles defined passively with existing patterns was used. To have nozzle arrays with fine-pitch and thus high-density, anisotropic etchings such as RIE and DRIE was used. Finally, to manage the development of diffusion zone during electrodeposition, the aspect-ratio and spacing-to-diameter ratio are chosen to be 6 and 2, respectively, as they have been shown to be optimal for the array-based fabrication process.

4.3 Device Fabrication

The selected optimal nozzle aspect-ratio provides a common window of withdraw speed wide enough for the simultaneous growth of an array of metal microwires, while minimizing the variation in wire diameters across the array with a reasonable growth rate for high throughput fabrication. Following the design criteria mentioned above, nozzle arrays used to perform the parallel metal direct-write process are fabricated following the fabrication process shown in Figure 28.

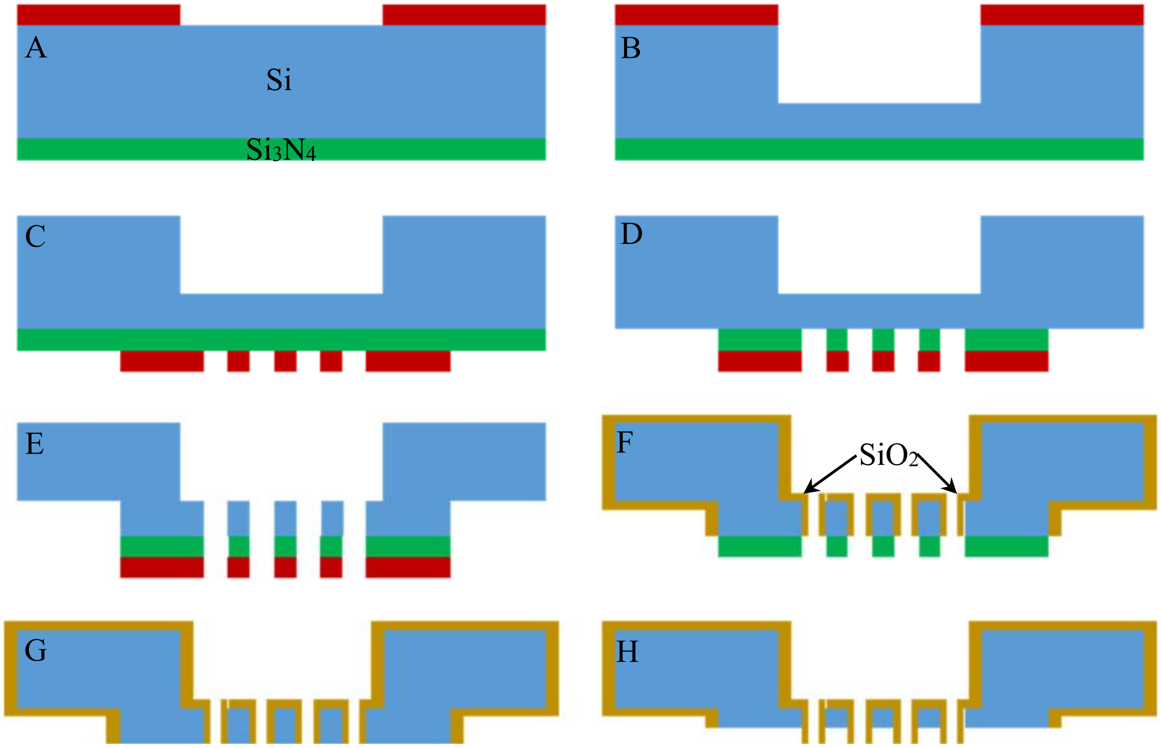

Figure 28. The fabrication process of the nozzle array.

The fabrication process starts with a cleaned double-side polished Si wafer of 480 μm in thickness. First, shown in Figure 28(A), a Si_3N_4 film of 100 nm thick is deposited onto the front side of the wafer using low-pressure chemical vapor deposition. The nitride layer was later served as a protection layer in the thermal oxidation. Second, to pattern the back side of the wafer to define the reservoir, a thin layer of photoresist, SPR220, is spun, patterned, and developed on the other side of the wafer, leaving the un-etched photoresist as mask for consecutive DRIE silicon etching. After patterning, shown in Figure 28 (B), DRIE is used to etch down 380 μm of the silicon wafer from the backside to form cavities that later are used as electrolyte reservoirs.

On the front side, another layer of photoresist, SPR220, is spin-coated, patterned and developed on the deposited Si_3N_4 layer, shown in green in Figure 28 (C), to define the shapes of circular nozzle arrays. Backside alignment is performed with extra care to ensure high precision. To expose the underneath silicon for through wafer etching to form micro channels, RIE is used to etch the thin nitride layer (Figure 28 (D)). After exposing the silicon layer, shown in Figure 28 (E), DRIE is used to etch through the Si membrane to form the nozzle channels that connect to the backside reservoir. During the DRIE process, several inspections are performed after few cycles of DRIE to ensure the uniform etch.

To define the final channels, Figure 28 (F) shows that the Si surfaces not covered by Si_3N_4 are thermally oxidized to form a conformal SiO_2 layer of 1 μm thick, which is done in a furnace. In the next step shown in Figure 28 (G), Si_3N_4 is etched off by RIE to expose underneath silicon before the final etch. In the final step, DRIE is used to etch down silicon to produce the protruding SiO_2 tubes, as shown in Figure 28 (H). The protruding SiO_2 tubes serve as the protruding nozzles for the parallel process direct-write electrodeposition.

In summary, a two-mask micromaching process is developed to create the nozzle array needed for the development. The process is found to be effective in reducing the difficulty in lithography alignment and thus achieve high fabrication precision as well as minimize steps involved in the fabrication process.

With the fabrication process described above, several nozzle arrays were fabricated on 4-inch silicon wafers. Several arrays consisting of various nozzle sizes and distinct configuration such as 1D or 2D arrays were fabricated. Figure 29 shows SEM images of one of the fabricated nozzle arrays, which consists of a 2D array of 20 by 20 protruding nozzles. Such an array contains uniform nozzles, shown in Figure 29 (B), with an inner diameter of 20 μm and a nozzle spacing of 50 μm. The lengths of those through wafer channels are 120 μm.

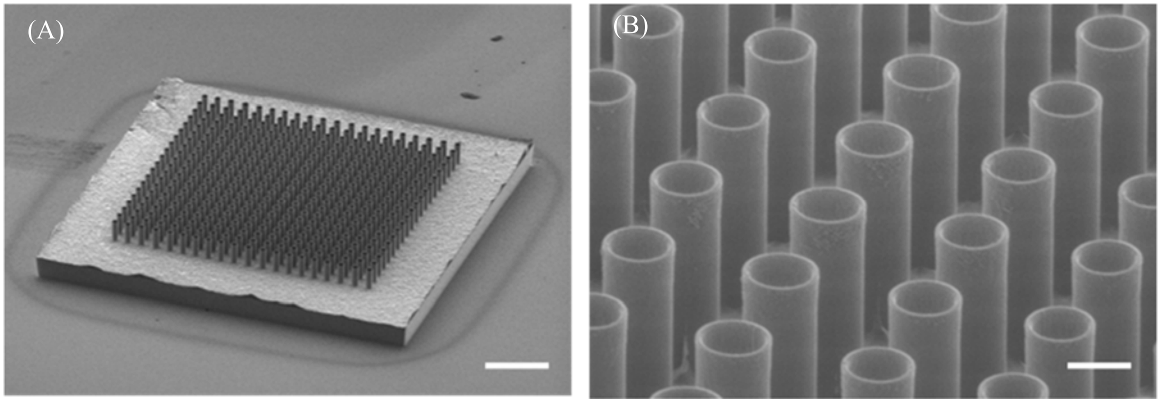

Figure 29. (A) An SEM image of a 20X20 nozzle array. The scale bar is 200 μm. (B) A Close-up SEM image of nozzle openings. The scale bar is 20 μm.

Such a nozzle array will be used to fabricate vertical wire arrays to verify the growth mechanisms and conditions. The quality of deposited metal wires will also be examined through mechanical testing.

4.4 Array-Based Parallel Process Manufacturing

Figure 30 describes the general principle of the proposed scaled-up process of meniscus-confined direct-write electrodeposition, in which an array of nozzles was fabricated through photolithography described above and filled with the selected electrolyte solution for metal electrodeposition. The general procedure of this process includes the parallel alignment of the nozzle array with a conductive substrate, the slow descending of the nozzle array to the substrate to establish the liquid contact with the substrate by the formation of a meniscus (liquid bridge) under each nozzle, the application of an electric potential to initiate the electrodeposition on the substrate, and the withdrawal of the nozzle array from the substrate at a set speed synchronized with the growth rate of metal wires confined underneath menisci. During the whole process, mechanical motions are precisely controlled by piezoelectric stages in all directions, and electrodeposition current was acquired to monitor the wire growth.

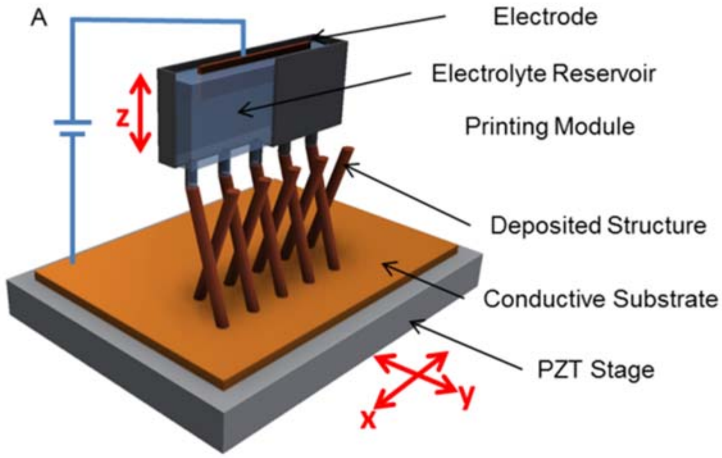

Figure 30. Schematic showing the working principle of the parallel direct-write process.

Issues such as the homogeneity of humidity across the nozzle array, the misalignment between the nozzle array and the substrate surface, and the microfabrication resolution of the nozzle array itself, can all introduce inhomogeneity in electrodeposition conditions across the nozzles in a nozzle array. To realize the synchronized and continuous co-growth of an array of metal wire structures without individually-addressable nozzle controls during the whole electrodeposition process requires the assistance of a self-regulated electrodeposition mechanism intrinsically existed in the meniscus confined electrodeposition, as have been analyzed in the previous chapter.

4.4.1 Array wire growth

A 1 M aqueous $CuSO_4$ solution for the electrodeposition of solid Cu metal microwires was used in the following fabrication. The array electrodeposition process is performed at room temperature in an ambient environment under a controlled relative humidity of 95% to 98% to minimize the variation in evaporation across the array nozzles. At this high relative humidity environment, the difference in evaporation rate between from the peripheral nozzles and from the inner nozzle should be within 1%. Two-electrode configuration is used for the electrodeposition with the gold-coated substrate as the cathode and a copper wire dipped into the reservoir electrolyte as the anode. A potential of 0.2 V is typically biased across the electrodes.

To ensure complete engagement between the array nozzles and the substrate, a small pressure (around 3 kpsi) is applied on the backside during the engaging process to force the electrolyte to form protruding menisci at the nozzle fronts, as shown in Figure 31.

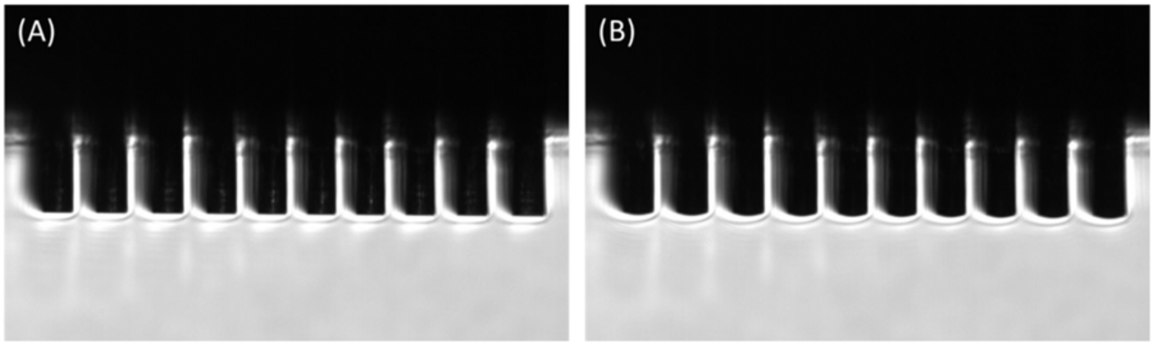

Figure 31. Optical images of a 10 × 10 nozzle array during the experiment illustrating the effect of applying the backside pressure. (A) without a backside pressure. (B) with a backside pressure.

Shown in Figure 32 is a 20 × 20 vertical Cu wire array fabricated with a nozzle array. To fabricate this Cu wire array, the overall ionic current is around 120 µA, and the withdrawal speed of the nozzle array for the continuous metal wire electrodeposition is about 40 nm/s, matches with that calculated based on the Faraday's law.

Figure 32(B) shows a close-up view of the wire array showing more clearly the wire quality.

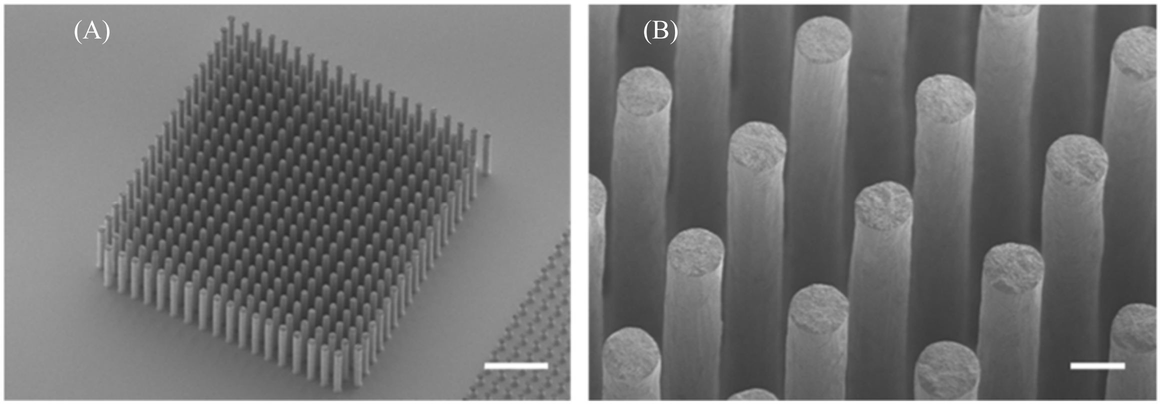

Figure 32. (A) SEM image showing a 20 × 20 array of vertical Cu microwires grown with the nozzle array. The scale bar is 200 µm. (B) Close-up SEM view of the same Cu microwire array. The scale bar is 20 µm.

4.4.2 Stability of the array growth

Previous discussion has shown that a window of stability for array-based electrodeposition exist if only the system is operated at the conditions that satisfy the continuous growth conditions for both the inner nozzles and peripheral nozzles. It was estimated based on the model that for a nozzle array having a nozzle aspect-ratio of 6 and a spacing to diameter ratio of 2, the common window of stability that can sustain the continuous electrodeposition growth across the whole array nozzles quantified in terms of the withdrawal speed of nozzle array is as much as 11-nm/s. In the following, different nozzle withdrawal speeds operating within the boundaries of the stability window were tested for the wire array growth. As shown in the inset SEM images, by choosing a withdrawal speed located in the middle of the common window of stability, continuous growth of metal wires across the whole nozzle array with uniform diameter distribution was realized; and when choosing a withdrawal speed located near the upper bound of the common window of stability, good quality metal wire growth was realized only from peripheral nozzles but not from inner nozzles.

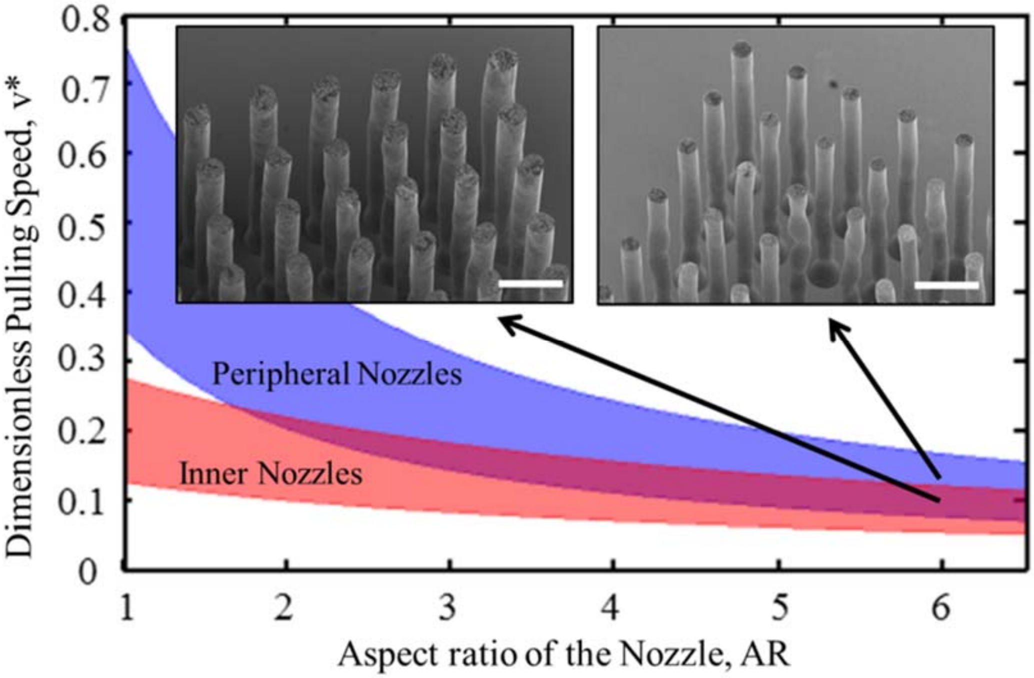

Figure 33. The common window of stability for self-regulated growth of metal wires in nozzle array based parallel process electrodeposition, and its dependence on the nozzle aspect-ratio. The insets show two representative 20×20 metal wire arrays produced at different withdrawal speeds, one at the middle of the common window of stability and the other at the upper limit of the common window of stability. The scale bar is 50 μm.

In such a nozzle array based electrodeposition, to make sure that such a common window of stability exist, a high degree of planar alignment between the nozzle array and the substrate surface is required and further, a high humidity environment at around 95% is needed to maintain the homogeneous evaporation condition across the whole nozzle array. Such conditions can be relaxed somewhat for small-sized nozzle arrays, such as for 1 × 10 and 2 × 10 arrays, where all nozzles are essentially peripheral nozzles and are exposed to similar surrounding environmental conditions. Uniform wire growth can be successfully realized from such nozzle arrays even at a relative humidity of only 80%. However, once inner nozzles are introduced, for example, for a 3 × 10 nozzle array, only a wire array with more significant diameter variations can be produced if a lower relative humidity environment is provided. As shown in Figure 34 for a wire array produced at a relative humidity of 80%, metal wires produced around the 4 corners are relatively large in diameter compared to the ones inside the array. As having been explained before, during the electrodeposition, there are less diffusion zone overlap and more evaporation involved with corner nozzles, and thus higher ionic current density through the corner nozzles, consequently, large diameter wire growth through the self-regulated growth process.

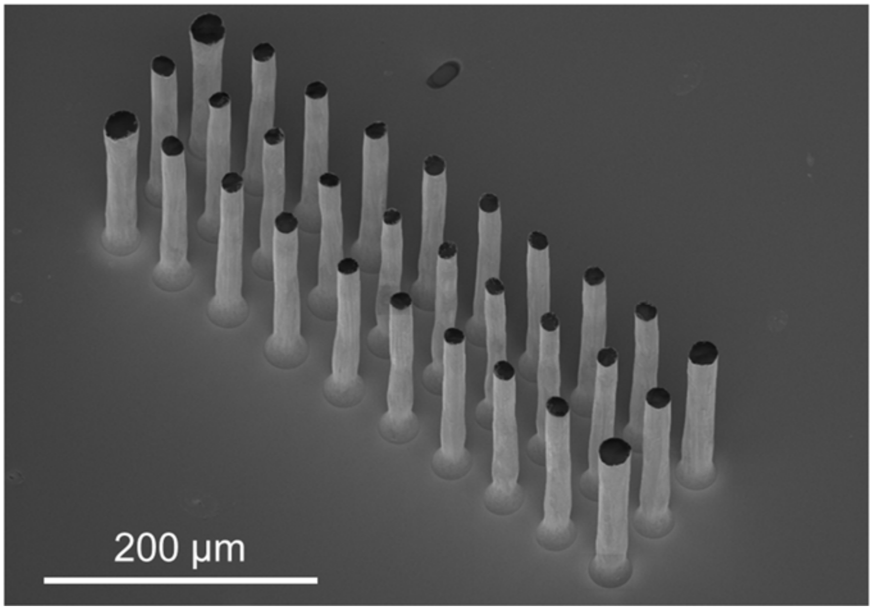

Figure 34. Diameter distribution of a 3 by 10 array

4.4.3 Mechanical characterization of metal wires

The Young's modulus of the Cu wires was measured through bending tests on three electrodeposited straight Cu wires of 510 μm in height and around 27 μm in diameter with a Hysitron Nanoindenter. Mechanical characterization of the deposited Cu wires was performed through a lateral deflection test by a Hysitron nanoindenter with a flat-ended tip.

Figure 35 (A) shows an SEM image of three straight Cu wires deposited onto a flat substrate for indentation tests. The left wire in the image has a diameter of 27.0 µm and a length of 511.9 µm. The middle wire has a diameter of 27.0 µm and a length of 510.0 µm. The right wire has a diameter of 26.8 µm and a length of 511.3 µm. Using the experimental data to measure the slope of the force response, the stiffness of a wire was obtained. A representative force vs. deflection curve acquired from the right wire shown in Figure 35 (B) yields a stiffness value of 76.9 N/m. Multiple tests were performed on each of the three microwires, yielding an average stiffness of 81.6 N/m for the left microwire, 80.1 N/m for the middle microwire, and 76.4 N/m for the right microwire. Young's modulus was calculated using the following equation:

$$E = \frac{4kl^3}{3\pi r^4} \tag{15}$$

The indentation was performed at a spot about 20 µm from the free end of the wire. Applying a cantilever stiffness model, the Young's modulus of the electrodeposited Cu was deduced to be 121.0 GPa, a value well matched with the reported value for bulk Cu. From the measured stiffness values, the electrodeposited Cu wires were found to have a Young's modulus of 121.0 ± 2.8 GPa, similar to that of bulk Cu. In other words, the quality of the deposited material through the array-based fabrication process is as good as the bulk material.

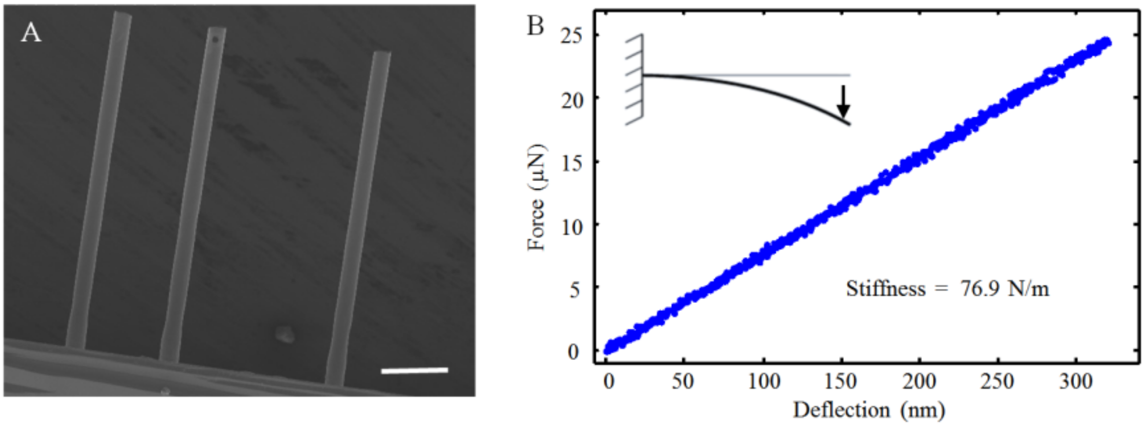

Figure 35. The elasticity measurement of deposited Cu wire. (A) An SEM image of three straight Cu wires deposited onto a flat. The scale bar is 100 μm. (B) A representative force vs. deflection curve acquired from the right wire shown.

4.5 Summary

In this chapter, a two-mask photolithography process was developed to fabricate nozzle arrays for the array-based meniscus-confined electrodeposition. The photolithography process was designed to minimize the amount of lithography steps involved and to avoid the issues related to lithography alignment. Various 1D and 2D nozzle arrays were successfully fabricated and used to test the array-based meniscus-confined direct write fabrication process. Following the developed theory, optimal growth conditions were acquired to realize high quality wire array growth. Critical growth conditions were also tested to verify the existence of the common window of stability predicted in the model analysis. Mechanical properties of the deposited metal wires were characterized, demonstrating the comparable quality with its bulk counterpart.

Although results shown in this section are with regular patterns that have a uniform spacing between nozzles, the array-based fabrication can be applied on patterns with various spacing among nozzles. For a nozzle array with irregular inter nozzle spacing, the upper bound of the stable growth window should still be defined by the peripheral nozzles, as discussed in the previous model analysis, where the effect from neighboring nozzles is less significant. The lower bound of the stable growth window should be determined by the nozzles with minimum spacing in the pattern. As long as these two windows overlap, a stable growth window exists for the rest of the nozzles. In other words, when designing a nozzle array device with a random pattern, one needs to consider the minimum spacing that exists in the nozzle array in order to find the critical growth condition.

In general, the material selection for array-based deposition relies on choosing suitable electrolytes that are practically and economically appropriate. Theoretically, as long as materials that electrochemically reduced can be used in this array-based meniscus-confined electrodeposition. The material, practically, has to be reduced at a reasonable rate to continue the growth as well as being economically applicable for fabrication. For instance, copper, heavily used in this research, is not only economically and practically appropriate for electronics applications owing to outstanding intrinsic material properties, it’s higher deposition rate makes it a superior candidate to fabricate bone structure for certain application that core materials are less significant to their performance. In some cases, post-processes such as electroless plating can be performed to enhance structural quality in order to fulfill different needs.

CHAPTER 5

FABRICATION OF ULTRA-HIGH ASPECT-RATIO MICROSTRUCTURE ARRAY

5.1 Introduction

In the past few decades, designs of I/O pad configuration has moved from the perimeter configuration to the area-array configuration because of higher I/O pad density, lower parasitic impedance, and improved thermal package performance.

However, increase of I/O pad density in area array configuration also increase the difficulty for testing, as testing the high density area-array requires reliable testing probes that establish appropriate contact through surface oxidation layer penetration and accommodating fabrication variation at different touchdown locations (*109, 110*).

Traditional probe cards for testing a perimeter configuration IC chip, which is an epoxy ring mounted with tens of hundreds of testing probes manually, cannot satisfy the need for high precision area array probing because of their complicate assembling process and fabrication difficulty. For testing devices with area array I/O pad configurations, MEMS-based probe cards are the most promising because of their high contact precision retained from photolithography processes(*111, 112*). However, as the dimension of the device decrease with higher I/O pad density and finer pad pitch, it is also challenging the limitations of MEMS-based probe cards due to the intrinsically planar nature of the micromachining processes. Further develop of the testing probe must consider a difficult trade-off among structural density, aspect-ratio, mechanical performance and process complexity.

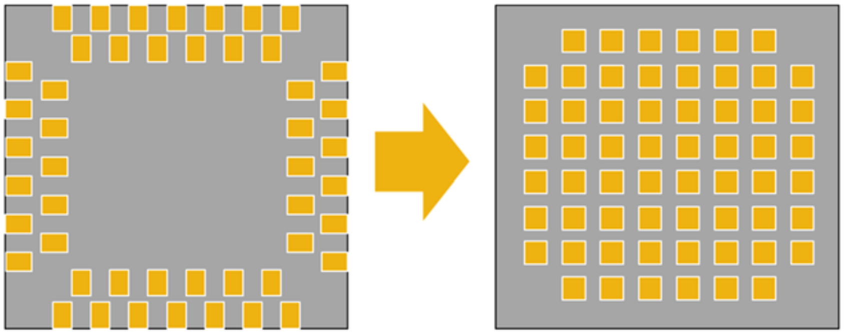

Figure 36. Evolution of the I/O pad configuration from a perimeter configuration to an area-array configuration.

The objective of this chapter is to design and fabricate a fine-pitch probe array for future I/O test applications via array-based parallel process developed in this study. The parallel process direct-write electrodeposition introduced in this study overcomes many technical limitations in the existing methods and enables the fabrication of such mechanically 3-D shaped metal array microstructures in a single step. Such an array should consist of conductive metal probes fabricated following the mechanical and dimensional design requirements potentially appropriate for their applications as wafer probes for chip testing.

5.2 Design of a Testing Probe

Owing to the process complexity, photolithography processes are not ideal for fabricating probes with complex shapes. However, probes fabricated by photolithography are with simple geometries such as zigzag shapes and often suffer from structural failure near sharp corners or de-bonding at the interface between the probe base and a substrate surface. Structural failures in probes are usually caused by the stress concentration near sharp corners that appear in structures. On the other hand, de-bonding at the interface at the substrate results from excessive bending moment with respect to the base of the structure under external loads. Therefore, to design a probe that is mechanically appropriate, we need to minimize the stress concentration within a structure and reduce the bending moment with respect to the base when a structure undergoes external loads. Besides, the structure needs to have a lower structural stiffness in order to accommodate height differences among probe arrays and testing I/O pads.

As a result, the design of the probe was with the structure shown in Figure 37. To reduce the bending moment with respect to the base, the structure has a center to center tip-base alignment. Such a design takes the advantage of the 3D continuous movement of the meniscus-confined electrodeposition to have a continuous and smooth shape without sharp corners, which prevents a structure from the failure caused by the stress concentration, i.e. to reduce the maximum stress appears in a structure. In addition, this spring-like 3D continuous shape has a low structural stiffness, which allows a testing probe to accommodate for geometrical differences between probe array and test pads.

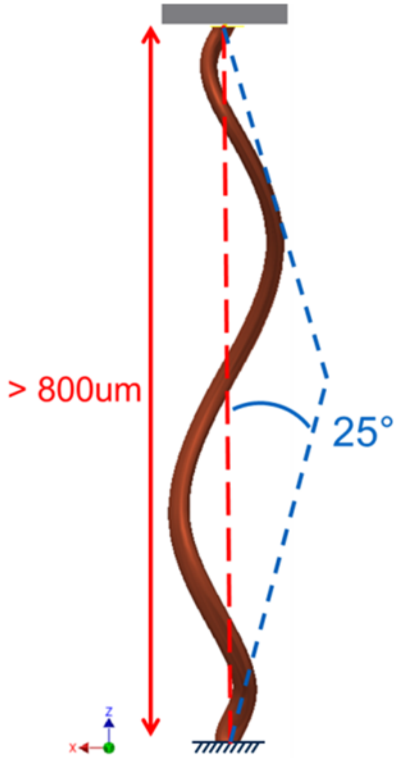

Figure 37. The design of the test probe

As a result, the shape of the resulting probe consists of two conical helixes starting from a 50 µm tall straight Cu segment (which is also the geometrical central axis of the spiral), one outward to a maximum diameter of 100 µm and immediately followed by the other inward helix, both at a cone angle of 25^0. The spiral terminates at geometrical center with another 30 µm tall straight segment along the central axis. This helix shape provides the structure a spring like function that absorbs external impact and minimize the structural bending moment when it undergoes external loads at the probe tip. The total height of the spiral is 805 µm and the diameter of the wire design, shown in Figure 37, is 18 µm.

5.3 Fabrication of Probe Arrays

Follow the experimental procedure of the array-based electrodeposition described in the last chapter, test probe arrays were fabricated. Figure 38 shows a 20 by 20 high density array of ultrahigh aspect-ratio Cu spirals fabricated using the parallel process direct-write electrodeposition with the design described above. The array was fabricated on a gold coated substrate in a single process without any post-processing. The motion of the nozzle array is programmed to produce such a curvilinear shape with the appropriate pulling speed of 40nm/s, the same rate as vertical wire growth.

This array of Cu spirals has a pitch of 50 µm, mirroring exactly the nozzle spacing in the 2-D nozzle array. Close inspections shown in Figure 38 (B) and (C) illustrate the high surface quality and uniformity of tips and bases of the array structures. Figure 38 (B) and (C) also shows the 50 µm tall straight Cu segment at the base and the 30 µm tall straight segment at the tip.

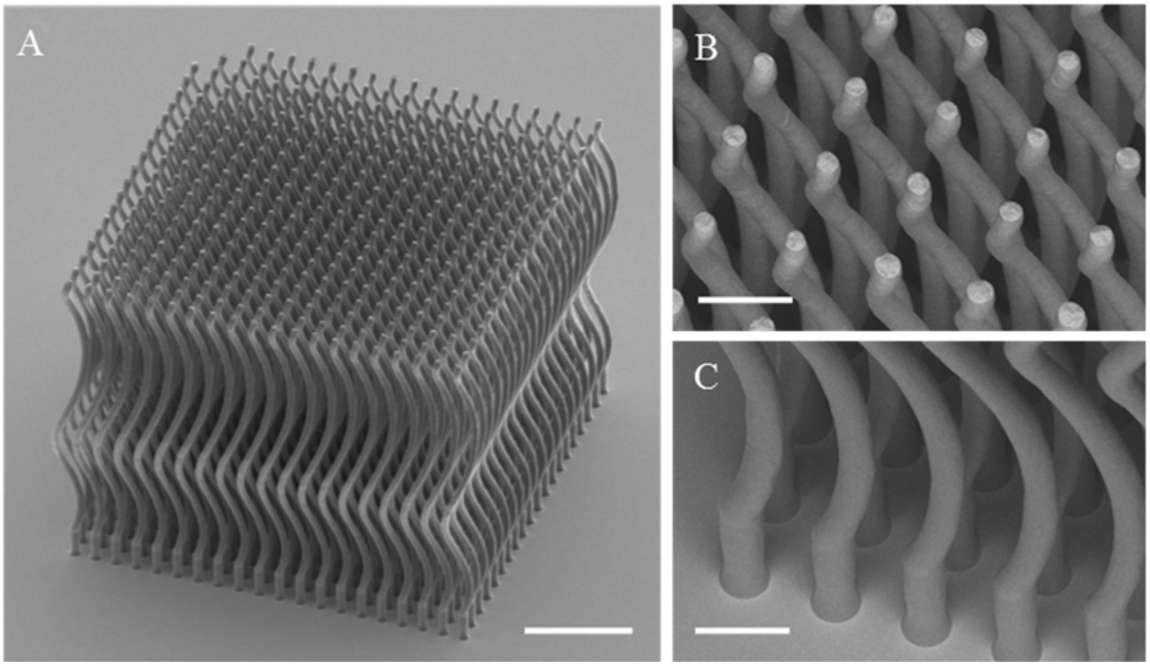

Figure 38. SEM images of a 20 by 20 array of microhelices of 700 µm tall and 20 µm in wire diameter. (A) Overall view of the array. The scale bar is 200 µm. (B) The tops of microhelices. The scale bar is 50 µm. (C) The bases of microhelices. The scale bar is 50 µm.

Such a high-density probe array with complex shapes cannot be fabricated with other conventional methods as those methods requires numerous consecutive steps to finish an array and cannot produce structures with high complexity. Not only our methods produce highly complicated structures in a single step, our method is capable of further miniaturization. Since future development of the chip I/O pad density also depends on reliable testing methods, using conventional MEMS probes because less feasible as dimension of a chip shrinks. As a result, our fabrication method is a perfect candidate for the future probing applications.

5.4 Mechanical Characterization of Probes

5.4.1 Indentation test

To examine mechanical properties of test probes, indentation tests were conducted on a 2 by 10 probe array, shown in Figure 39, with specified structural design described in the previous section. The uniaxial compression test with the use of a Hysitron Nanoindentor with a flat-ended indenter probe was carried out on selected individual spirals shown in Figure 38, test results are plotted in Figure 40 (B). In an ideal condition, wires fabricated in an array are identical. However, differences in the evaporation rate and diffusion zone development of 4 corner nozzles in the 2 by 10 array are different from 16 “inner” nozzles. As a result, diameter variations appear in the probe array, thus different mechanical properties.

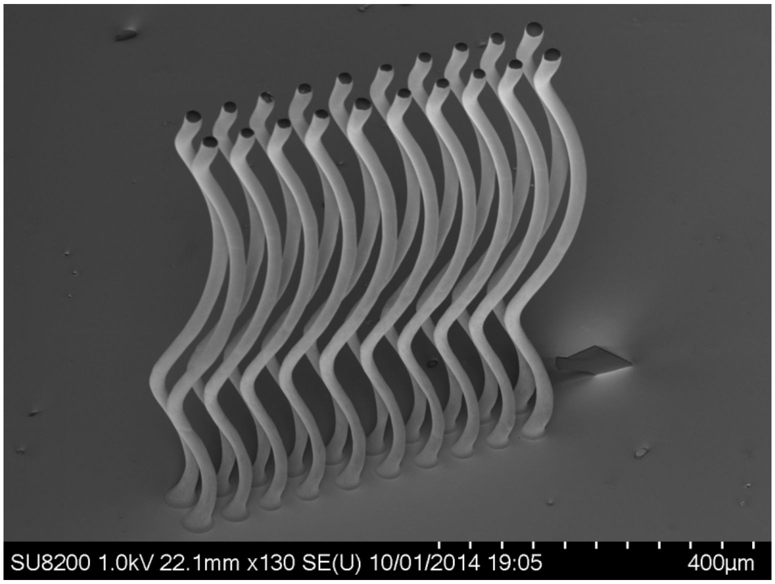

Figure 39. The 2 by 10 probe array with the same design as the 20 by 20 array fabricated for the indentation test.

From measurements of the SEM image, corner 4 probes are found to have a diameter of 18.5 μm and inner probes have a diameter of around 16.5 μm. Thus, two groups of mechanical test results are plotted in Figure 40, one group in red is data from four corner probes and the other in blue are data from inner probes. Results show that with maximum indentation depth of the instrument, 4.5 μm, test probes exhibit linear mechanical responses toward external loads. In other words, probes are elastic within the compression depth of 4.5 μm.

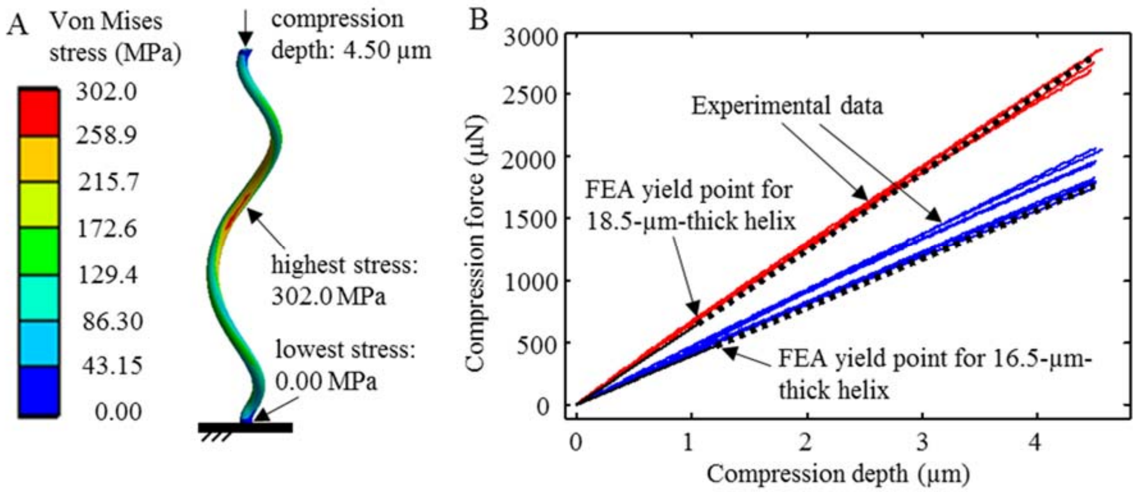

Figure 40. Mechanical characterization of helices. (A) FEA simulation. (B) Compression experiment results in comparison with simulation results.

5.4.2 Finite element simulation

I modeled the structure using CAD software Autodesk Inventor to obtain a geometry that precisely reflects that of a real structure, then the geometry was imported into the finite element analysis software ANSYS before simulation. Finite element analysis was performed to simulate the compression test and to reveal the stress distribution in the wire during the process, results are shown in Figure 40. In the simulation, the probe diameter of 18.5 µm was used to simulate test results of corner 4 wires. Young's modulus of copper as 128GPa was extracted from the experimental data of the vertical wire bending test and applied to the simulation. Linear elastic material with isotropic elasticity was assumed. Relevant physical properties of the copper material used in the simulation are included in Table 1.

Table 1. Relevant physical properties of the copper used in the simulation

Property	Value
Young's modulus (GPa)	128
Poisson ratio	0.34
Density (kg/m^3)	8960
Tangent modulus (GPA)	10

First stress distribution of a probe undergoes the maximum deformation, 4.5 μm, is shown in Figure 40 (A). As the result, the highest von Mises stress of 302 MPa with a probe diameter of 18.5 μm occurred at the inner wall near the center portion of the spiral, and is much higher than the typical yield strength of bulk Cu, which is merely around 80 MPa. The stress occurred at the base of the spiral is nearly zero, a feature potentially beneficial for mitigating the risk of debonding of the spiral from the substrate in actual applications. In addition, our design showed the more uniform stress distribution without obvious stress concentration because of continuous structural shape that has no sharp corner.

Mechanical response of shown in black, each line consists of two parts, one solid and one dotted, solid maximum stress of 70MPa occurs, dotted extended linear response with higher maximum stress. Showing material stronger than bulk. Since no plastic deformations were observed, the yielding stress of the material with a Hysitron Nanoindentor could not be obtained using a nanoindentor.

5.4.3 Cyclic test

Because test probes usually need to perform millions of tests throughout the life time. The uniaxial cyclic compression test were carried out with the use of a flat-ended indenter probe on selected probes and examine mechanical properties after tests. Therefore, 75000 loading-unloading cycles were performed with the dynamic mode of the Nanoindenter with probe spirals were compressed to the maximum indentation depth allowed, which is ~ 4.5 μm, before releasing external compressive loads. Normal indentation tests were performed after cyclic tests with same force-displacement results without displaying any plastic deformation behavior.

5.4.4 Failure test

To acquire the yielding strength of the electrodeposited Cu structure, a displacement controlled cyclic uniaxial compression test was performed on the fabricated Cu spirals with a custom-made mechanical testing setup since the yielding strength cannot be obtained using a nanoindentor. The spiral was shown to yield only at a compression of exceeding 15 μm. According to the corresponding finite element analysis, this elastic deformation cannot be reached unless the yield strength is of almost 850 MPa. In the yielding finite element analysis, a bilinear isotropic hardening elastic plastic material model was used.

This high yield strength is attainable in nanocrystalline Cu due to the Hall-Petch strengthening effect or in nanotwinned Cu (*113-115*). Hall-Petch strengthening, $\sigma_y = \sigma_0 + kd^{-1/2}$, predicts that the yield stress increase with the inverse of the square root of the grain size(*116*). A bulk copper has coarse grain sizes usually greater than 100 μm. On the contrary, our probes have diameters that are less than 20 μm, grains in our wire should be much smaller than coarse grains presented in a bulk material. Extrapolate from equation, a yielding stress of 850MPa has a grain that is about 17 nm (*117*). In the case of our parallel fabrication process, high yielding stress might be due to the nanocrystalline structure formation in Cu wire electrodeposited at high diffusion limited current density of near 12 A/dm^2.

As a result, this high density high aspect-ratio Cu spiral microstructure array, possessing extremely high mechanical yield strength, intrinsically high electrical conductivity (almost 5 time higher than Ni based material typically used in wafer probe applications) and designed mechanical compliance, could be the ideal interface structure for serving as interconnect in chip scale packaging to alleviate thermomechanical mismatch issues in flip chip bonding, or as wafer testing array probe meeting both mechanical and area density requirements in advanced chip testing.

5.5 Summary

In this chapter, probe arrays that are suitable for applications such as the chip testing were designed and fabricated in an effort to resolve issues exist in the conventional probe fabrication methods. Mechanical testing of the resulting structure were performed and the testing results were compared to the simulation modeled by ANSYS finite element analysis, which yields good agreement.

The array-based fabrication process not only provides a way to fabricate probes with high complexity, the material property of the deposited material is stronger than bulk material possibly owing to the nano-crystalline structures produced in the high current density condition. As a result, the yielding stress of the deposited material is over ten times higher than a bulk material when back track the material properties using finite element model in comparison to the yielding test preformed in our setup. Besides, the further miniaturization of the array-based fabrication is more feasible than traditional MEMS probe devices. In other words, array-based meniscus-confined parallel process could be a promising candidate for fabricating next-generation IC testing probes.

CHAPTER 6

THREE-DIMENSIONAL MICRO PRINTING

6.1 Introduction

The array based parallel process electrodeposition discussed in the previous chapters realizes the fabrications of metal microstructure arrays having the array spacing matching exactly the array spacing of the corresponding nozzle array defined through the lithography-based microfabrication. However, due to some technical limitations in lithography-based microfabrication for fabricating the nozzle array that needs to meet certain design requirements, it is still difficult to apply this parallel process electrodeposition method to fabricate very high area density metal microstructure arrays having spacing to diameter ratio below 2. Besides, the previous method is limited to fabricate only continuously-shaped wire structures, as the electrodeposition process is self-regulated continuous deposition one. On the other hand, the traditional 3-D printing technology has shown to be versatile in fabricating essentially any-shaped 3-D structures through the digitized voxel-based forming mechanism. Herein, 3-D metal micro-printing process is developed which integrates the concept of the traditional 3-D printing with the meniscus-confined electrodeposition principle to realize the 3-D printing of high mechanical and electrical quality pure metal microstructures with extremely high aspect-ratio, extremely high array density and more complex 3-D shape. Moreover, a parallel process 3-D metal micro-printing process is developed which integrates the traditional 3-D printing with the nozzle array based electrodeposition to significantly scale up the 3-D printing process for making metal structures with microscale and even nanoscale resolution, and ultrahigh aspect-ratio.

6.2 Mechanisms of the 3-D Metal Micro-Printing

The general principle of the 3-D metal micro-printing process is schematically shown in Figure 41. The meniscus-confined electrodeposition is applied to deposit only a short segment of metal wire each time at every designated sites that can be highly closely spaced, and is repeated on the same designated sites for growing the second short segments. A final metal structure is fabricated by going through many of such repeated processes in an essentially "layer by layer" fabrication process. In this digitized fabrication process, the voxel is defined by the diameter of a nozzle and the thickness of each layer, more complex-shaped and compact metal array microstructures can be fabricated, while the microstructural and mechanical quality of the deposited metal is guaranteed by electrochemical deposition principle. In this study, the diameter of each deposited metal segment was varied from 200 nm to 25 μm, and the thickness from 100 nm to 2 μm, dimensions not accessible with existing 3-D printing methods.

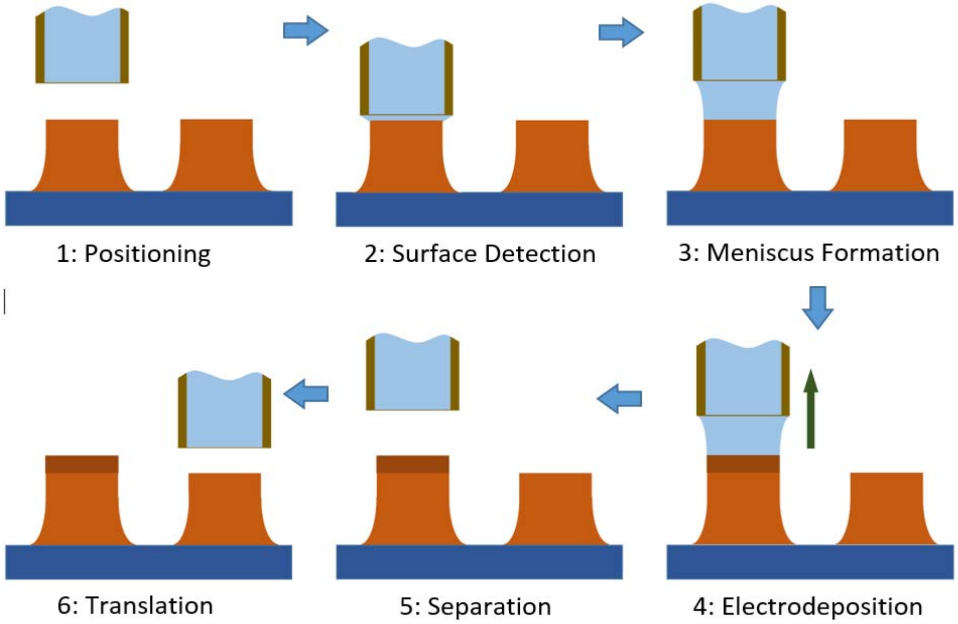

Figure 41: The working principle of the electrochemical 3-D micro-printing via a confined meniscus, enabling printing of microscale and nanoscale metal structures in a discrete manner.

6.3 Comparison between a Continuous Process and a Printing Process

Due to the existence of a liquid/air interface in the meniscus confined electrodeposition, and thus the continuous evaporation of water off the microscale meniscus, as explained previously, the rate of metal deposition is intrinsically higher than the corresponding electroplating process typically performed in an electrolyte bath. The "on-and-off" nature of the micro-printing process promotes the evaporation further, which allows the quick replenish of the metal ions in the meniscus through diffusion and the conditioning of the electrolyte in the meniscus to higher concentration through water evaporation during the "off" stage. Both are favorable for realizing higher electrodeposition rates for depositing the metal layer in the subsequent "on" stage.

Figure 42 (A) shows the current data of a printing wire and a continuous grown wire recorded when a 5μm micro-pipette was used, which exhibit distinct patterns. The dotted line in the figure shows a typical deposition current during a stable continuous process. It was found that, upon the initiation of the electrochemical reaction, the current response undergoes an initial drop and gradually stabilizes as the process proceeds. The current response of a printing process comprises four voxels of copper print, represented by the solid line in Figure 42, in which every voxel printing contains two current pulses. The printing of each voxel consists of four stages, including detecting a surface, engaging a meniscus, printing a material to a target length, and separating the meniscus. The first short pulse in the printing current corresponds to the engagement of the meniscus after surface detection, when a meniscus forms and bridges the surface with a supporting electrolyte. The second current peak denotes an actual material deposition process followed by zero current during off-time operations: voltage cutoff, meniscus separation after each growth, and consecutive surface detection.

In general, the rate of deposition can be obtained from current data. In Figure 42, the current during an entire actual printing is higher than the stable current in a continuous pulling process, which suggests a higher deposition rate. Recorded current data can be used to calculate segmental lengths via numerical integration and Faraday's law:

$$l = \frac{M}{Fz\pi r^2 \rho} \int I \, dt \tag{16}$$

where l the length of the wire, t the printing period, M the molecular weight of copper, F the Faraday number, r the radius of the wire, and ρ the density of the copper.

From the equation, the rate of deposition within the "on" stage of the micro-printing process was calculated to be 215 nm/s, which matched well with that calculated through measuring the layer thickness in a scanning electron microscope. In comparison, the same nozzle was used to continuously grow a Cu wire at a nozzle withdrawal speed synchronized with the height growth rate of the Cu wire without going through the "on-and-off" printing process, and the acquired variation of current in time is included as the dotted line in Figure 3. The rate of deposition was determined to be ~170 nm/s, 20 percent smaller than the rate in the printing process.

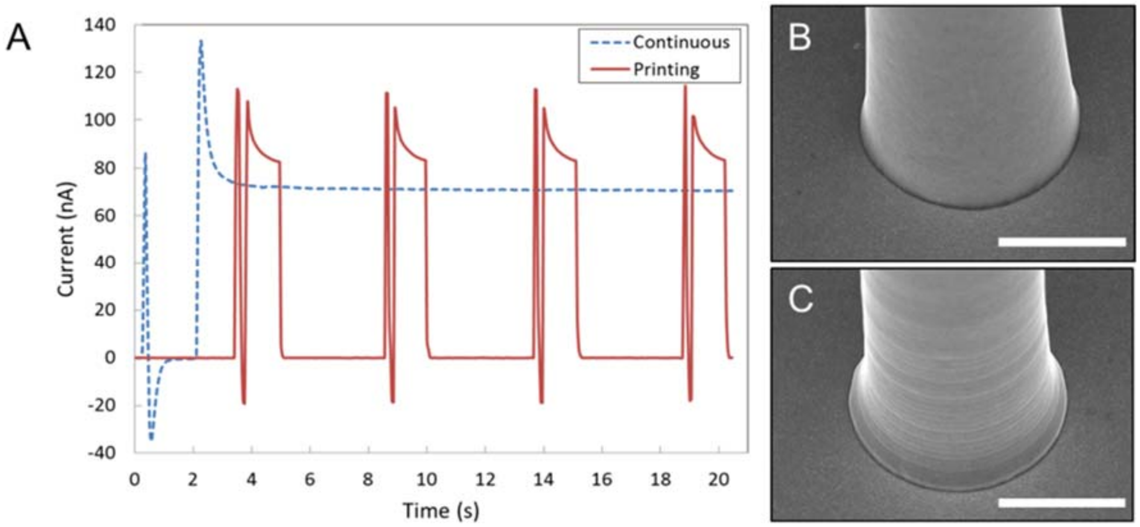

Figure 42. Ionic current response in the 3-D micro-printing process. (A) Plot showing the ionic current variation in time during the electrodeposition of 4 metal layers (solid curve) acquired from the printing of a Cu wire with the use of nozzle having a diameter of ~ 5 µm. The narrow peak indicates the detection stage for locating the exact x-y-z coordinates of the starting surface for printing, and the wide peak indicates the electrodeposition stage to deposit a metal layer of a designated thickness, in each printing period. The ionic current variation in time (the dotted line) acquired during the continuous electrodeposition of a Cu wire of ~ 5 µm in diameter realized within the stability limit of the meniscus by synchronizing the nozzle withdrawal speed with the (height growth) rate of the wire (at 170 nm/s) was included for comparison. (B) SEM image showing the surface finish of the continuously electrodeposited Cu wire. (C) SEM image showing the micro-printed Cu wire and the layered presence. Both scale bars are 3 µm.

Microscopic textures and features of two wires fabricated using a continuous growth process and a printing process are shown in scanning electron microscope (SEM) images in Figure 42 (B) and (C), respectively. Figure 42(C) shows a printed wire with a tapping layer thickness about 300nm, this closer view of resulting wire reveals segmented character produced by layer-by-layer deposition. Performing numerical integration via eqn (1) yields a wire layer thickness that is similar to our SEM observation. When adopting extremely thin layers, wires yield high surface quality close to continuous growth wires shown in Figure 42 (B). Therefore, such printing is applicable for creating high quality pure metal structures without compromising surface qualities.

Certainly, the overall rate of fabrication should also take into account the "off" time in each period of layer deposition. Considering the printing of a wire of a fixed height by depositing layers of thickness of h each, the rate of fabrication is then $h/(t_{on} + t_{off})$, where t_{on} and t_{off} are the time durations set for the electrodeposition stage and the rest for printing each layer, respectively. $t_{on} = h/v$, where v is the rate of electrodeposition or the withdrawal speed of the nozzle that can sustain the electrodeposition of metal to a certain thickness before the meniscus breaks. t_{off} is the time duration mostly needed for translating the nozzle to a new neighboring site and is typical fixed. The rate of fabrication is then $h/(h/v + t_{off})$. As t_{off} is typically larger than t_{on}, it is understood that the highest rate of fabrication is realized by maximizing the printed thickness of each layer with the highest withdrawal speed of the nozzle. Note that this v is above the speed parameter window of stability for maintaining the stable meniscus formation during the whole synchronized and sustained electrodeposition process, so only a thin layer of metal can be deposited before the meniscus is stretched to break. The higher this nozzle withdrawal speed goes, the thinner the deposited metal layer. The optimal rate of fabrication is thus simply determined by the needed layer thickness resolution and the highest nozzle withdrawal speed capable of just producing that desired layer thickness.

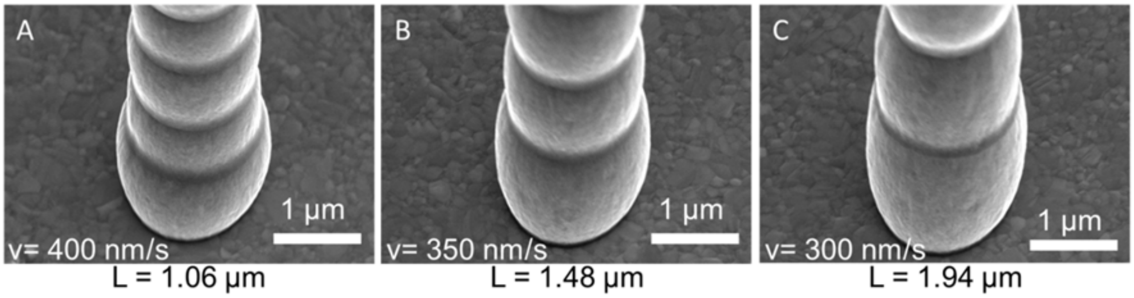

Figure 43. The sustainable segmental length, L, with respect to the pulling speed, v, in the printing scheme. Results show the sustainable segmental length increase with the decreasing pulling speed. (A) L = 1.06 μm with v = 400 nm (B) L = 1.48 μm with v = 350 nm (C) L = 1.94 μm with v = 300 nm

6.4 Printing of Compact and Complex Micro/Nano Structures

To demonstrate the advantages of this proposed printing method for constructing microstructures with high complexity, several representative structures were printed and shown in Figure 44 and Figure 45. Ultrahigh density and ultra-high aspect-ratio metal microstructure arrays were readily fabricated, as shown in Figure 44 (A)-(B). The layer-by-layer nature of the printed metal structures is clearly seen in the structures. With nanopositioning motion control, there is practically no limit on how close the neighboring structures can be fabricated next to each other. Compact structures shown in Figure 44 (A-D) with high aspect-ratio cannot be produced by a continuous growing process because the existing structure prevents a dispense tool from accessing the adjacent printing site. Structures with complex geometry were also created even when a structure has vertically-overlapped features (Figure 44 (E)-(I)), which takes advantages of the discrete manner in which structures are built layer-by-layer. In a continuous process, an existing structure prevents a micro-pipette from depositing a material in the underneath working area, limits the creation of a free-form structure. A mesh structure was printed to show the capability of printing structures with inter-connects (Figure 45A).

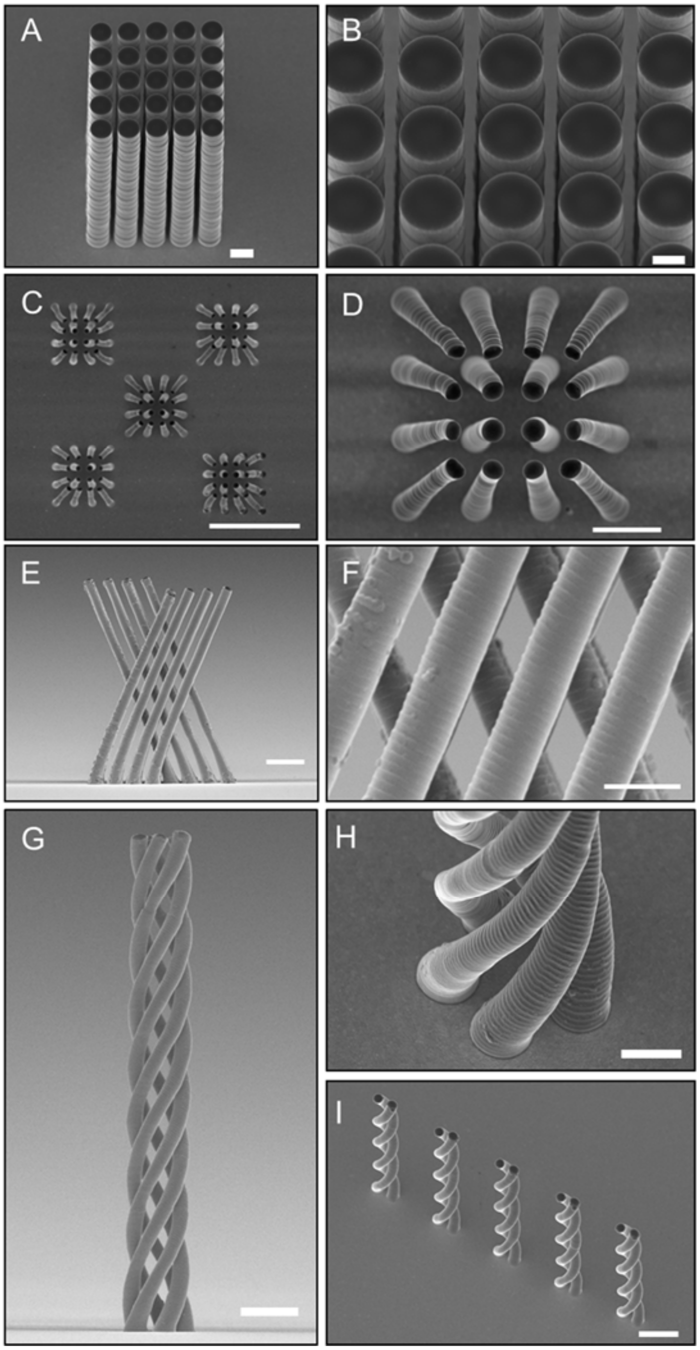

Figure 44. SEM observations of micro printed 3D structures. (A) High density vertical wire array of 25µm in height. Diameter of each wire is 2µm. The scale bar is 2µm. (B) Zoom-in image of high density wire array. Layer thickness of 1µm with gap spacing of 300nm. The scale bar is 1µm. (C) An array of shrinking wire arrays. Each array has is about 10 um in height. The scale bar is 25µm. (D) Zoom-in image of a shrinking array, with center to center spacing decreasing from 5µm to 2.5um. The scale bar is 5µm. (E) A 4 by 4 tilted wire array using a 2µm pipette with layer thickness of 200nm. The scale bar is 5µm. (F) Zoom in of the tilted wire array to show surface texture of the surface. Resulting tilting wires are 1.4µm in diameter. The scale bar is 2µm. (G) A multi-threaded helix tower consists of 5 wires of 2µm in diameter and the height of tower is 43.7µm. The scale bar is 5µm. (H) Image near the base of the tower. The scale bar is 2µm. (I) An array of double helix wire towers with 28.5 um in height and layer thickness of 200nm. The scale bar is 5µm.

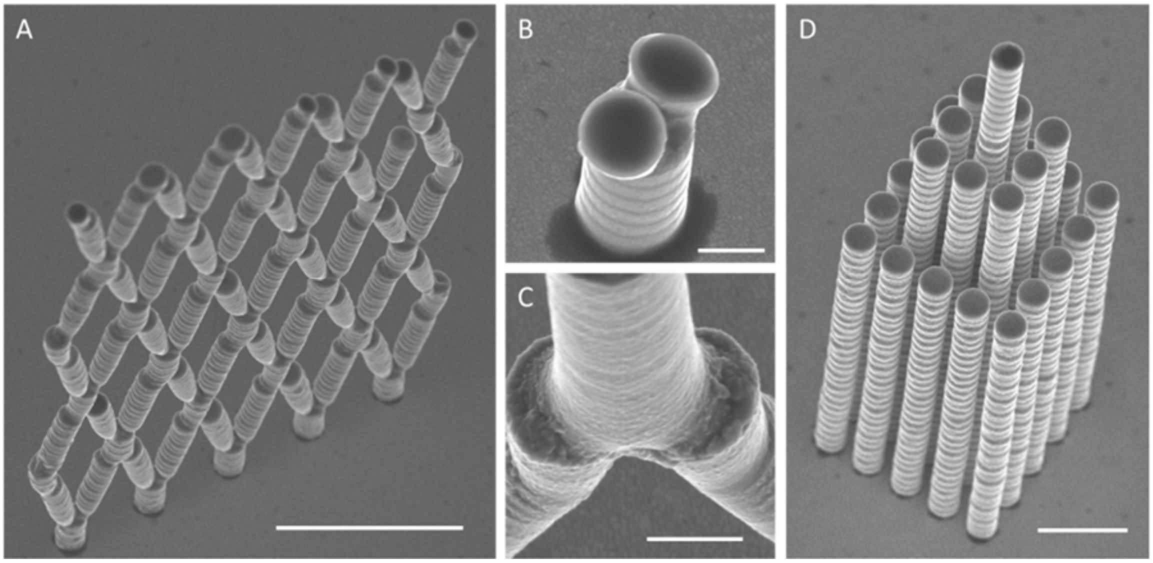

Figure 45. Some printed complex structures. (A) A printed large scale interconnected web structure constructed by unit structures shown in (B) and (C). The scale bar is10μm. (B) Zoom-in image of a interconnect structure showing formation of the branch out joint. Scale bar is 1μm. (C) Zoom-in image of a interconnect structure showing formation of the merging joint. Scale bar is 1μm. (D) A high density vertical array with different height. Scale bar is 5μm.

The 3-D metal micro-printing was extended to nano-printing by creating structures using nano-pipettes and thinner layer thicknesses. Figure 46, for example, shows a 3-by-3 vertical wire array printed using a 250nm-diameter nano-pipette with layer thickness of 100nm in each print. A close inspection shown in Figure 46 (B) reveals the layer-by-layer nature of the printing process. Another 2-by-2 nano-wire array with wire diameter of 300nm and aspect-ratio over 65 was created, shown in Figure 46 (C). Realization of printing ordered high density nanowire arrays potentially validates many applications such as gas sensors, biological tags, nano optics and so on, as geometric shape and high surface area of these 1-D nano-material potentially provides high functionality (*118*).

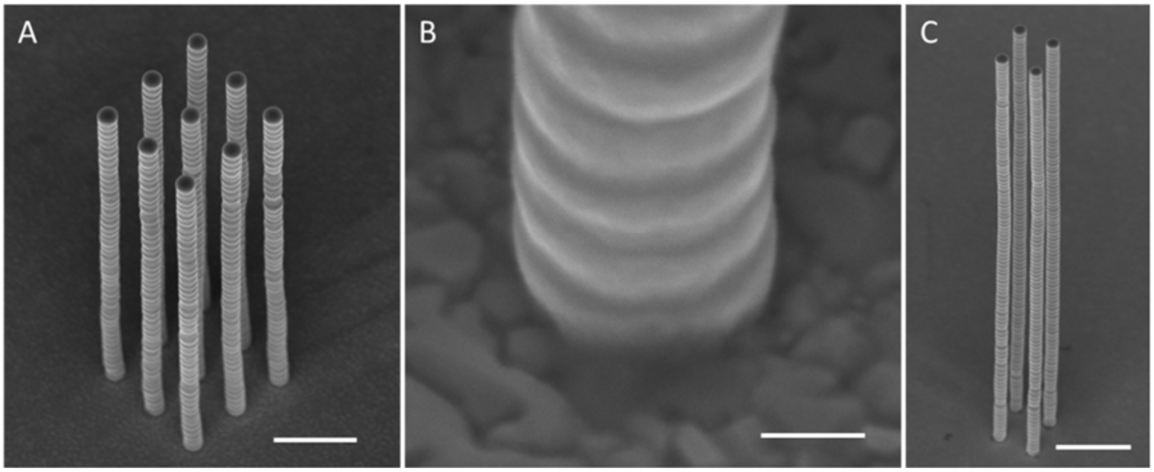

Figure 46. Vertical nanowire arrays. (A) A 3 by 3 nanowire array with 700nm spacing, structure is 6 µm in height. The scale bar is 1µm. (B) Zoom-in image of a printed wire base showing wire diameter ~240 nm. The scale bar is 100nm. (C) A 2 by 2 wire array with wire diameter of about 300nm and 20 µm in height gives aspect-ratio over 65. The scale bar is 2 µm.

6.5 Self-regulated Parallel Process 3-D Micro-Printing

Scaled-up 3-D micro-printing can be realized through the self-regulated printing mechanism unique to the meniscus-confined electrodeposition and the use of a nozzle array for micro-printing. Figure 47 (A) shows a nozzle array based micro-printing process that "prints" an array of metal wires array layer by layer with each layer having a thickness as thin as 500 nm. Detailed microscopic view shown in Figure 47 (B) reveals the layered characteristic of the printed wire. Figure 47(C) shows another array structure fabricated with the parallel process micro-printing, which consists of an array of oppositely tilted metal wire pairs. In this case, the parallel process micro-printing fabricates not only simultaneously an array of microstructures matching the array pattern of the corresponding nozzle array but also paired microstructures that are closely packed and with designed 3-D shapes and configuration. A close-up inspection, shown in Figure 47 (C), shows again the layered texture as a result of the printing process.

In the nozzle array based 3-D micro-printing, the variation in nozzle dimension and the misalignment of the nozzle array with the substrate practically exist. However, within the thermodynamic stability limit of the meniscus, meniscus formation can be realized between every nozzle opening and the corresponding growth front of the metal wire, albeit the stable shape of the meniscus varies slightly from one nozzle to another. For example, at a place with more separation between nozzle opening and metal wire, the meniscus is stretched more, which, during the meniscus confined electrodeposition, results in the deposition of a metal wire segment of less diameter but with a higher (height growth) rate. This effectively levels out the initial unevenness of the growth fronts of all wires under all nozzles. The same leveling effect exists due to the slight variation of nozzle diameters across the nozzle array.

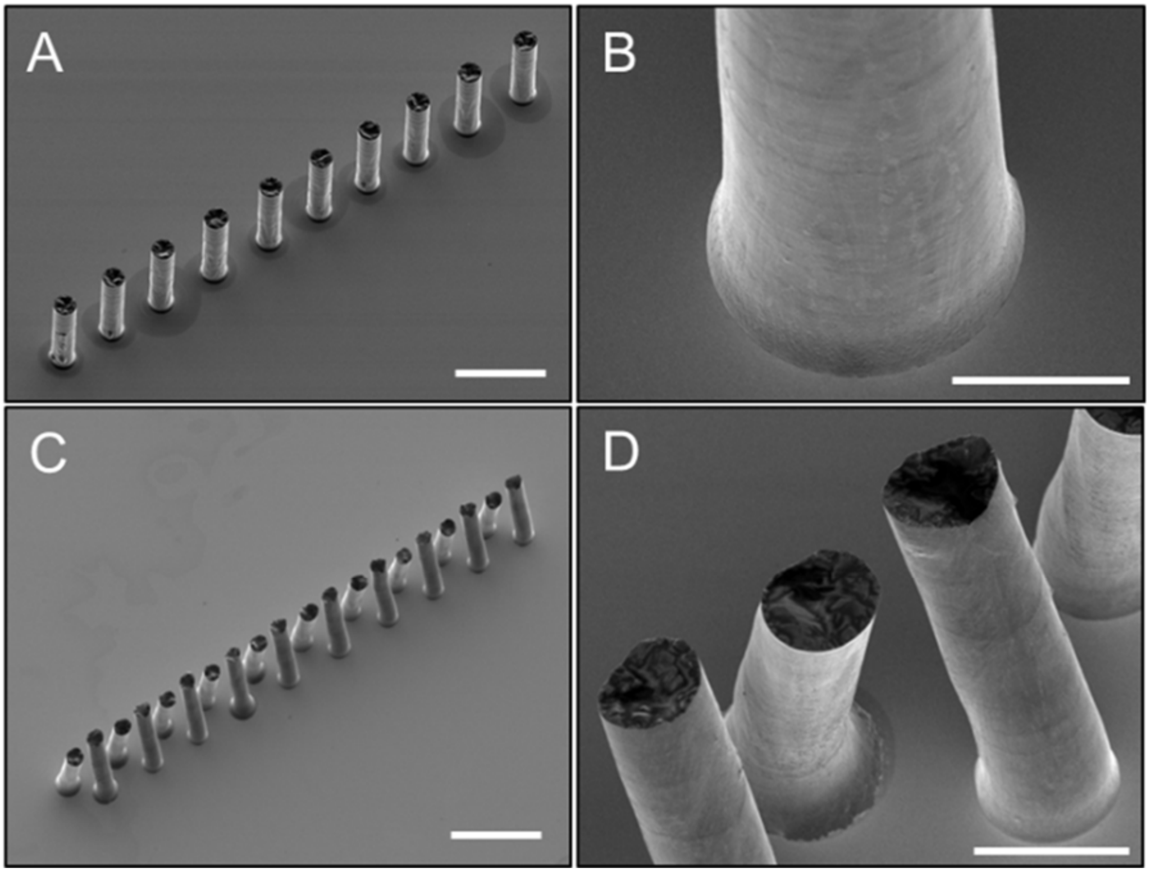

Figure 47. SEM images of Cu wire structures micro-printed with the nozzle array based micro-printing method. The center to center spacing of the wires is 70 µm. (A) A vertical metal wire array with wires 80 µm in height. The scale bar is 100 µm. (B) Close-up view of a wire in the vertical wire array showing the layered texture with a layer thickness of 500 nm. The scale bar is 10 µm. (C) An array of tilted metal wire pairs printed with the nozzle array based micro-printing method. The wire height is 100 µm. The scale bar is 100 µm. (D) Close-up view of the printed metal wire pairs showing the layer thickness being around 500 nm. The scale bar is 20 µm.

The parallel process micro-printing is further scaled up with the use of a nozzle array consisting of over 3000 microscale nozzles in an area of 12 mm by 12 mm as shown in Figure 48. Figure 48 (A) shows an optical microscope image of a printed pattern, which shows the successful printing of metal structures from the great majority of nozzles in the nozzle array. The missing of structures near some corner areas is caused by the imperfect alignment between the nozzle array and the substrate surface or potentially a small degree of planar warping of the nozzle array itself. The warping problem in large nozzle arrays fabricated through the lithography-based fabrication process has been documented in other studies and can be technically resolved with more careful nozzle designs. The high planar alignment resolution requirement between the nozzle array and the substrate surface is also within the limit of existing precision machine control technologies. Efforts in both direction were underway.

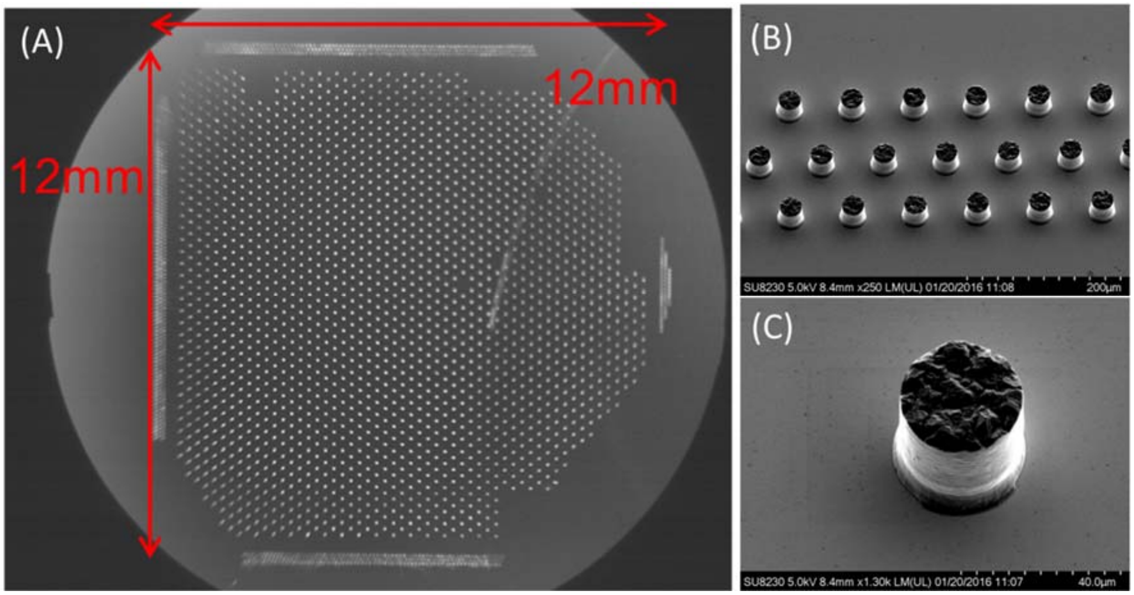

Figure 48. Large stamp printing. (A) An optical image of large stamp printing showing the resulting stamp pattern of 1.2mm by 1.2mm. (B) An SEM image of close inspection of the printed array. (C) An SEM image of close inspection of an individual printed wire.

6.6 Material Characterization of Parallel Printing

To confirm material integrity of printed structures, mechanical testing of the printed wires has been performed in a Hysitron nanoindentor. The acquired Young's modulus of the electrodeposited copper is found to be 116.4 ± 4.0 GPa, within the reported range for bulk copper. This was expected as the sequential metal layers were fabricated through electrodeposition and were bonded together with atomic quality interfaces.

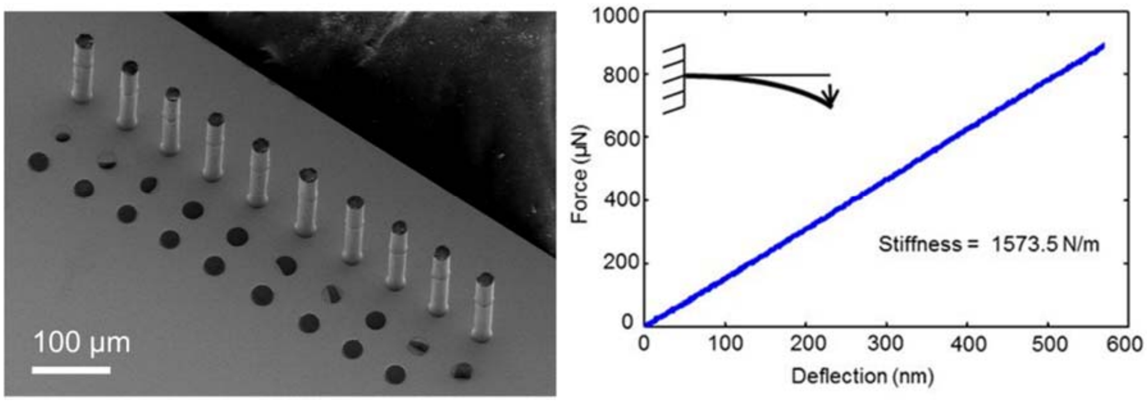

Figure 49. Mechanical measurement of printed Cu wires. (A) An SEM image of ten straight Cu wires deposited onto a flat substrate. The scale bar is 100 µm. (B) A representative force vs. deflection curve acquired from a wire shown in the array.

6.6 Summary

In this chapter, a three-dimensional micro-printing method was developed that realized the 3-D printing of pure metal structures in the micro-/nano- scale. Microscale and even nanoscale structures with high structural quality and complex 3-D shapes were printed to demonstrate the process capabilities. Theoretically, this method is available for printing any materials that can be electrochemically reduced and onto any conductive substrate, thus significantly extends the traditional 3-D printing method.

A parallel process 3-D micro-printing was further developed for high throughput fabrication of metal microstructures. Successful parallel process printing of array structures with the use of corresponding nozzle arrays was demonstrated. Some technical issues remain to scale up the process for printing very large scale arrays, but can be resolved with the existing capabilities with further improvement. With a properly designed and fabricated nozzle array and more precise alignment between the nozzle array and the substrate, an array of more complicated 3-D metal microstructures as those presented in Figure 44 and Figure 45 can be fabricated with the parallel process printing process to significantly multiply the production. A larger nozzle array may also be microfabricated and be used to efficiently produce a larger array of potentially ultrahigh density and ultrahigh aspect-ratio three dimensional microstructures that has so far beyond the reach of existing microfabrication capabilities.

CHAPTER 7

EXTENTED DEVELOPMENTS OF THE MENISCUS-CONFINED METHOD

7.1 Introduction

In this section, several extended developments of the meniscus-confined electrochemical method were reported, including control the bias between an anode and a cathode, adjust AC voltage frequency and on/off ratio, reverse the voltage, and raise the temperature of the growth interface. These extended methods are applied in an effort to control the internal structure or to accelerate the rate of the deposition through control of the ion transport. Various preliminary results of extended studies imply the future development of the technique.

7.2 Low Frequency Growth of the Meniscus-Confined Electrodeposition

In AC deposition, there are several parameters that can be controlled, including the relative humidity of the environment, and the magnitude, frequency, and on/off ratio of the applied voltage. In this section, low frequency AC voltages (frequency < 50Hz) are applied between the anode and the cathode in an effort to control the ion transport of the process thus the internal morphology of a fabricated structure. As a result, hollow tube structures are obtained through this voltage control. For instance, Figure 50 shows a hollow tube array fabricated using a 3 μm pipette with applied voltage of 0.5V and on/off time of 10ms/10ms at a relative humidity of 20%.

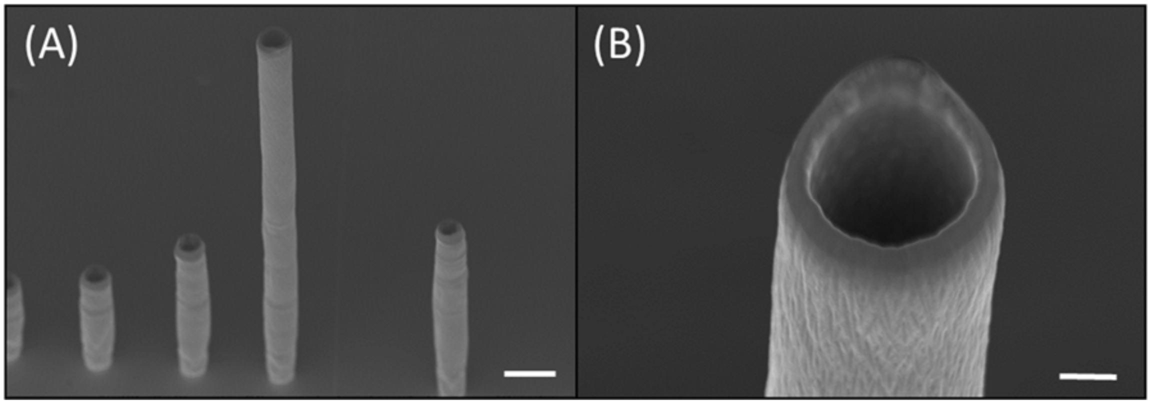

Figure 50. (A) An SEM image of a hollow tube array. Scale bar is 5 µm. (B) The close SEM inspection of the tube structure. Scale bar is 1 µm.

To demonstrate the reliability of the tube growth, a 5 µm pipette was used with applied voltage of 0.5V and on/off time of 10ms/30ms at relative humidity of 30% to fabricate a uniform 5 by 5 tube array, shown in Figure 51. Each tube in the array has a height 10 µm.

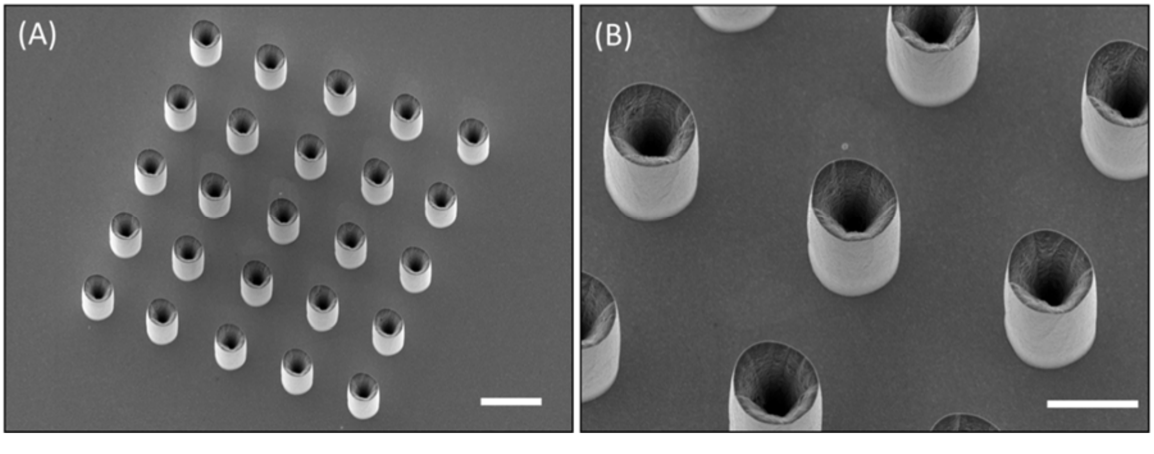

Figure 51. (A) An SEM image of a 5 by 5 tube array. Scale bar is 10 µm. (B) The close SEM inspection of the tube structure. Scale bar is 5 µm.

To further visualize the formation of the tube growth, experiments that sequentially grow tubes with designated incremental lengths, 0.5 µm, were set up. Figure 52 shows the evolution of tubular growth with the same pipette at environmental humidity of 30% and 50%. Both experiments use a 5 μm pipette with 0.5V applied voltage and on/off time of 10ms/30ms. The pulling speed of growth at 30% humidity, 85 nm/s, is slightly higher than that at 50% humidity, 75nm/s. Since two growths are performed with the same AC on/off ratio, a higher pulling rate in lower humidity implies grown wires have thinner walls.

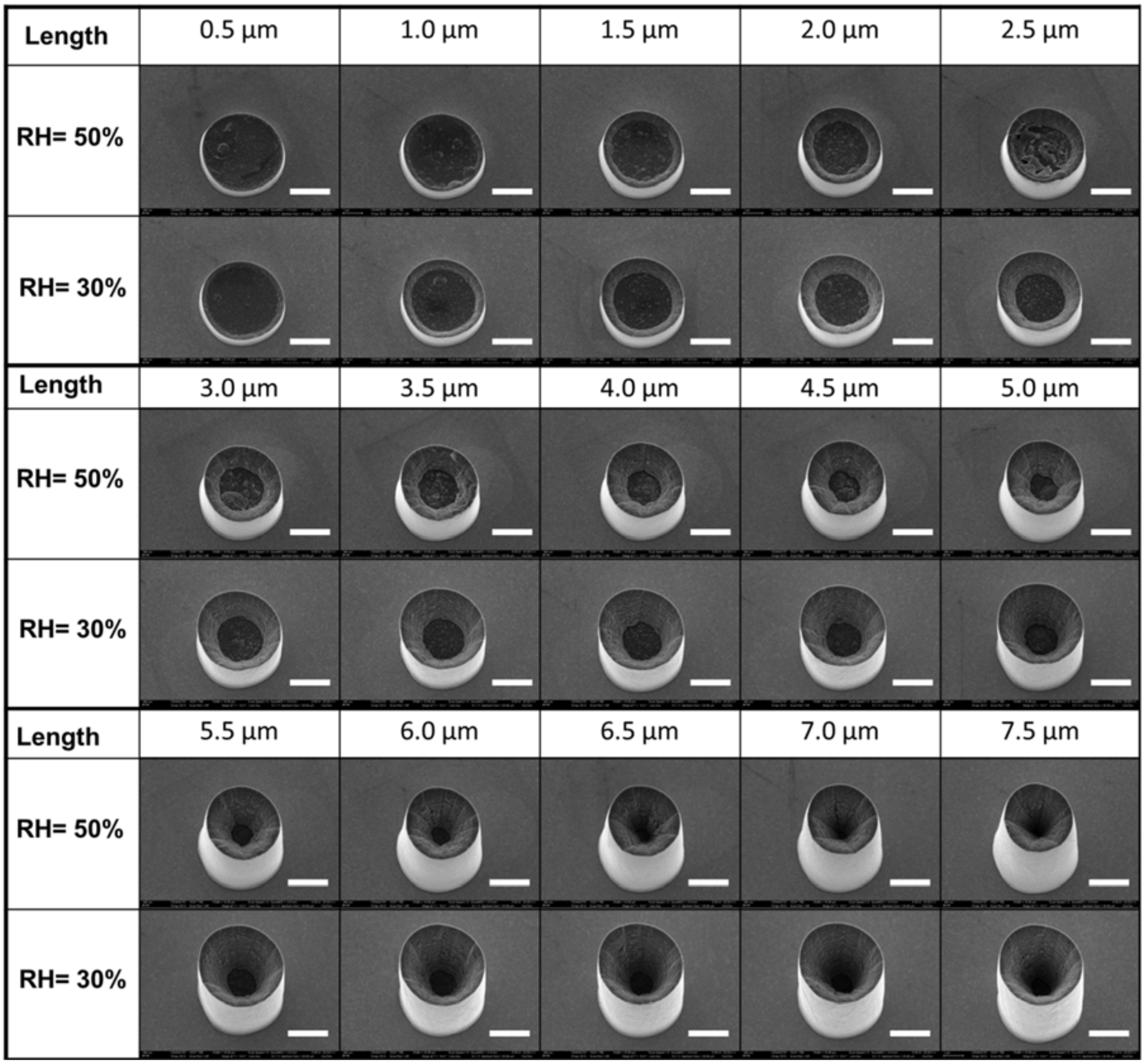

Figure 52. The evolution of tubular growth with the same pipette under two environmental humidities. Both are using a 5 μm pipette with 0.5V applied voltage and on/off time of 10ms/30 ms. Scale bars are 2 μm.

Figure 52 also shows growth at a 30% humidity reveals an earlier onset of the tubular growth, around 0.5 μm, whereas tubular growth appears at around 1.5 μm at a 50% humidity. However, in the later stage, growth at a lower humidity (30%) shows a thinner wall growth and a steeper edge profile toward center, confirms the results obtained in a higher pulling speed. This observation also implies growth at a higher humidity have more uniform planer ion consumption. In other words, ion concentration under lower environmental humidity may possess a more significant concentration profile at the growth front, with higher concentration near the edge than in the center.

A set of more comprehensive study on relevant parameters in AC growth were tested with 5 μm pipettes, results are shown in Table 2. In general, the pulling speed decrease with the increasing off-time. Besides, when the voltage was increased by 2 times for experiments with long off time, change in pulling speed is not significant. Besides, changing the RH has a limited effect on pulling speed when using a long off-time. Finally, when the pulse voltage was changed from 0.5V to 0.2V, the pulling speed does not decrease by more than half, instead, pulling speeds around 60-75% of 0.5V speed were obtained.

To conclude mechanisms of the tube growth, it is suspected that the tube growth is due to its higher ion concentration near the edge of the meniscus, established by strong evaporation during the off-time, been depleted within the on-time. There are several tubular growth parameters that need to be carefully controlled, including the on-time voltage, the pipette diameter, the frequency and the control of on/off time, and humidity control.

Table 2. Effects of relevant parameters on pulling speed

RH (%)	V (Voltage)	on/ off (ms/ ms)	Speed (um/s)
43	0.5	10/30	0.085
42	0.5	10/50	0.08
42	0.5	1/7	0.07
42	0.5	1/10	0.06
42	1	1/10	0.06
41	0.2	10/10	0.07
41	0.2	10/30	0.05
41	0.2	1/3	0.06
41	0.2	1/10	0.04
41	0.2	1/20	0.03
40	0.2	1/30	0.025
20	0.2	1/30	0.03
<15	0.2	1/30	0.03

In general, a higher voltage results in a higher current density and thus higher deposition rate, thus can be used to ensure complete depletion of highly concentrated ions during on-time of a pulse as long as the hydrogen evolution was suppressed. Smaller crystalline grains can also be obtained through higher voltage because of higher nucleation rates, which provides a better tube surface morphology. Although using a smaller pipette keeps the pulling at a higher rate, results from strong evaporation, a larger pipette ensures more stable meniscus formation. If a pipette is too small, meniscus becomes too unstable to stabilize the tubular growth. Contrary, if a pipette is too big, a large diameter prohibits the development of the variant concentration profile and results in conditions similar to solid wire growths.

In addition, to have tubular growths, the proper frequencies and on/off ratios are chosen when an on-time is sufficient for the depletion of highly concentrated ions, while an off-time is essential to establish required concentration profiles. If an on-time is not sufficient, remaining high concentration ions will diffuse to the center. On the other hand, an excessive on-time results in a thick-wall growth. Without the off-time (e.g. DC growth) or if an off-time is insufficient, it is possible the concentration profile near the edge is insignificant for a tubular growth, and results in growth conditions similar to solid wire growth. Another parameter need to be considered is the humidity of the environment. For growing a thin-wall tube, a lower humidity can be adopted in order to establish a steeper concentration profile near the edge of the meniscus.

In short, an optimal condition for the tubular growth might exist when an on-time is short enough to consume the high concentration ions and a high voltage without hydrogen evolution while an off-time is sufficiently long to have significant concentration profile.

7.3 Meniscus-confined Electrochemical Etching

When reversing an electrochemical cell, depends on the composition of the cell, a reverse reaction can be obtained. The copper deposition process used in this study is a reversible process when a substrate coated with copper is used. As a result, copper material can be removed using electrochemical etching as a micromachining tool. In this section, the meniscus-confined electrochemical method was used as an etching tool to etch thin layers of thermal coated copper on a glass substrate to demonstrate potential surface machining applications.

In this section, a e-beam evaporator was used to coat substrates with thin layers of copper of 100 nm in thickness. CuSO4 of 0.5M is used as the electrolyte with a copper electrode inserted in the micropipette. When performing electrochemical etching, reverse voltage of 0.5V was used to dissolve the surface coating. Most of material are etched by micro-pipettes with diameter of 2 μm.

Prior to experiments, patterns to be etched are designed in pixel forms as shown in Figure 53 (A). After the design, patterns are processed in MATLAB to obtain the position information, plotted in Figure 53 (B), before importing into the program for the pattern etching. It should be noted a pixel size is not necessarily the same as a pipette diameter in the meniscus-confined electrochemical etching. Each pixel represents a coordinate to be patterned and the dimension can be determined in the program where as the pipette dimeter merely determines the resolution of the pattern. In other words, a pipette diameter could be smaller than, equal to, or larger than a pixel.

There are two modes of the meniscus-confined electrochemical etching, one is the continuous etching mode and the other is the discrete etching mode. In a continuous etching mode, the orientation of the surface is first determined by detecting the spatial position of 3 points on a substrate. After determining the surface orientation, the pipette etches the coated copper following the designed pattern continuously, assuming the surface is flat. Therefore, pipettes in a continuous mode sweep through pixels, based on the designated routes and connect pattern, without leaving a blank when a pipette has a diameter that is smaller than the pixel size. On the contrary, in a discrete etching mode, pipettes engage on a surface to form the meniscus at every pixel of the pattern regardless of the surface profile because the meniscus-confined electrochemical etching implemented a feedback mechanism to detect the surface of contact in the revolving etching process. In other words, the continuous mode is suitable for patterning a flat surface while the discrete mode is capable of patterning a curved surface. However, in a discrete mode, extra caution is needed if the diameter of a pipette is smaller than a pixel to avoid leaving unwanted un-patterned spots in a pattern. With the build-in detection mechanism, the meniscus-confined electrochemical etching can be used for patterning a surface with complex geometry, which is difficult to be realized by any other methods.

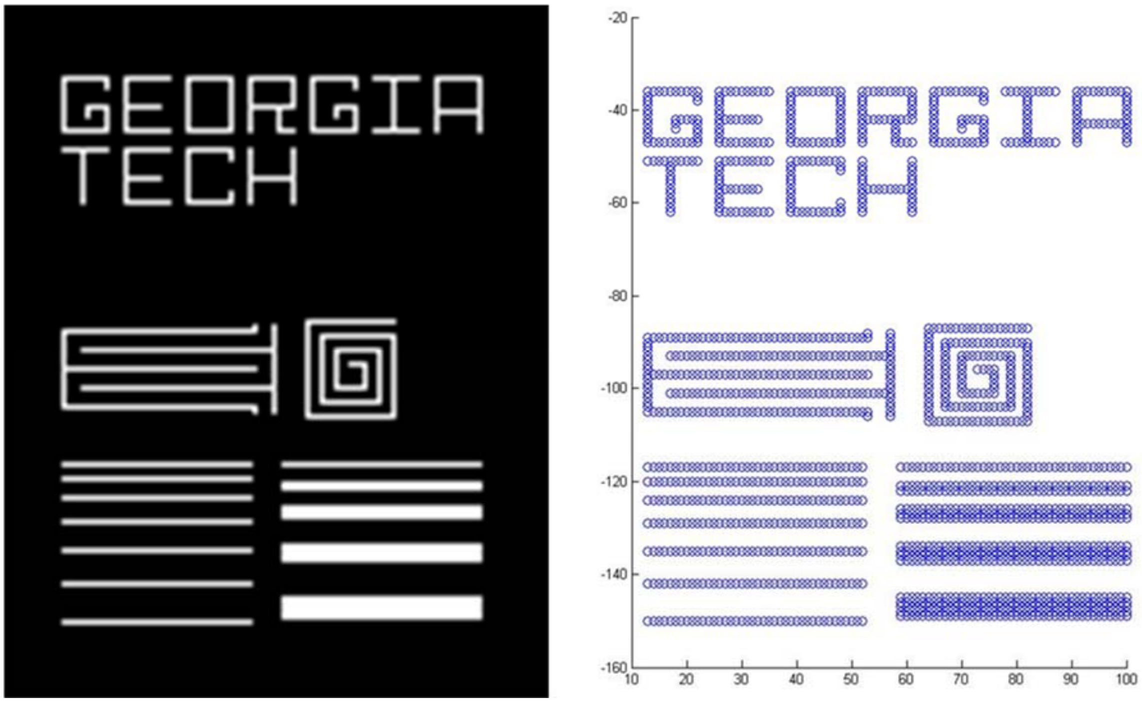

Figure 53. Pattern design for meniscus-confined electrochemical etching (A) pattern design in the pixel form (B) Exported file that contains position information for further etching

Several representative results are shown in Figure 54, Figure 55, and Figure 56. Figure 54 shows an optical image of two spirals that has been etched with different etching speeds in the continuous etching mode. The black area represents un-etched copper and yellow area represents etched surface that become transparent. The upper pattern with a thinner street size is etched with a pipette moving at a speed of 3 µm/s, and the other at a speed of 1 µm/s. With a slower moving speed, an etch width becomes wider due to the spreading of the meniscus.

Figure 55 (A) shows an optical image of the pattern etched with the discrete etching mode, where a pixel size is larger than the diameter of a pipette. As a result, a dotted pattern was observed as discussed. Figure 55 (B) shows another optical image of the zig-zag pattern, potentially can be utilized as a surface resistor, etched with the discrete etching mode with pixel size smaller than the diameter of a nozzle. This shows a high quality discrete etch can be achieved by meticulous pattern design and the corresponding pixel size. Figure 55 (C) shows two line patterns etched with different pipette moving speeds in the continuous etching mode, where the upper pattern is etched with a speed of 5μm/s and bottom pattern with a speed of 3 μm/s. From the figure, the upper pattern has more uniform line widths and the bottom pattern appears to have bat shapes, possibly caused by lingering electrolyte behind the etched patterns that is still electrochemically active. Shrinking patterns were previously seen in Figure 54, where a continuous etching starts from the center of a pattern. As the pipette moves further away from the etched area, the influence of the reverse voltage decreases. An optimal etching speed is chosen so that lines been patterned are as uniform as possible.

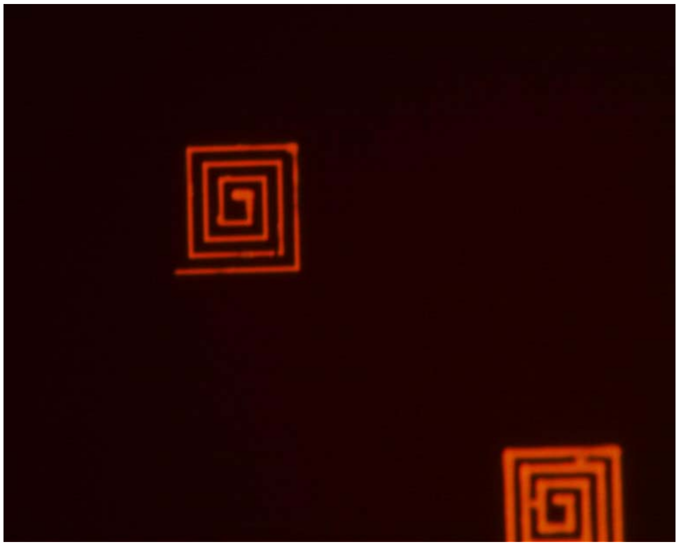

Figure 54. An optical image of the etched pattern. Black part is un-etched copper and light part is etched pattern.

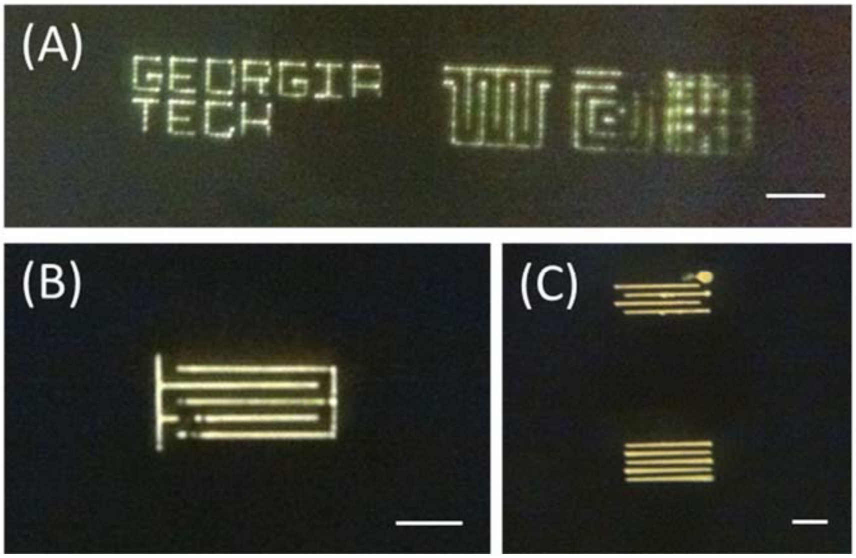

Figure 55. An optical image of etched pattern. Black part is un-etched copper and light part is etched pattern. (A) Scale bar is 20 µm. (B) Scale bar is 40 µm. (C) Scale bar is 20 µm.

Figure 56 (A) shows an optical image of several "GEORGIA TECH" patterns etched with various pixel dimension in a discrete etching mode using the same micropipette, and (B) and (C) are SEM images of the pattern. In the optical image, etched patterns become more scattered with an increasing pixel size. The pattern become fragment when a pixel dimension is larger than a pipette diameter, thus a worse pattern quality. Ideally, a pipette with a diameter slightly larger than width of a pixel will result in a better etching quality.

The meniscus-confined electrochemical etching, as demonstrated by the etching of the coper metal layers on transparent substrates, can be readily utilized as a fast prototyping tool for rapid mask-fabrications. Other potential applications include the curved-surface patterning and the post-process patterning for optical or electrical applications.

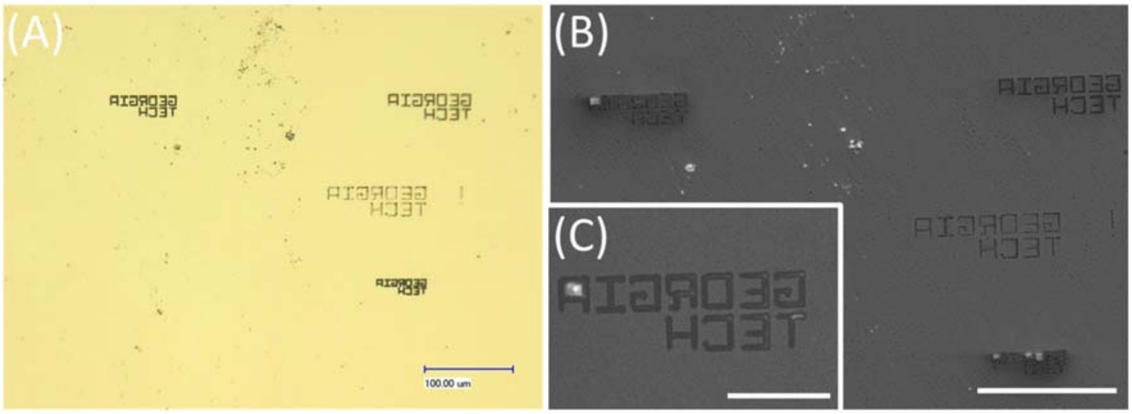

Figure 56. Optical and SEM images of a etched pattern. (A) An optical image of etched pattern. Yellow part is un-etched copper and black part is etched pattern. Scale bar is 100 µm. (B) SEM image of the same pattern. Scale bar is 100 µm. (C) An SEM image shows the close inspection of the pattern shown in the bottom right corner in (B). Scale bar is 30 µm.

7.4 High Temperature Meniscus-confined Electrodeposition

In addition to controlling an applied bias, the temperature at where electrodeposition takes place was raised to control the ion transport near the interface. Theoretically, an increase in the temperature of the electrolyte results in a higher conductivity, due to the higher ion mobility, and reduced anode and cathode polarization. In this section, the substrate temperature was raised in order to increase the rate of electrodepostion.

Several nozzle arrangements were tested including a single pipette, a 1 by 10 1 D nozzle array, and a 10 by 10 2D nozzle array. The substrate is heated with a ceramic heater (model HT24S2, THORLABS) place underneath the substrate. During the experiment, currents of stable growths of a setup were recorded and converted into current densities taking into account of the deposited surface areas underneath the nozzle setup. Results show linear relations between the current density and the heating power regardless the nozzle arrangement, plot in Figure 57. This indicates the deposition rate increases with the increase heating power, thus the raise in deposition temperature has an impact on increasing deposition rate.

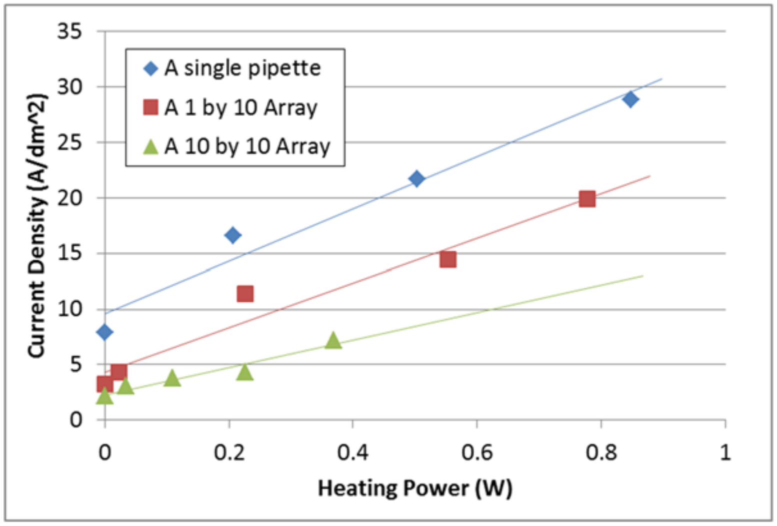

Figure 57. Current densities of different array arrangements with respect to the heating power of the metal ceramic heater.

To verify the quality growth of solid structures, theoretical pulling speeds were calculated based on recorded currents in experiments, using Faraday's law, and compared to the recorded pulling speeds. Results, shown in Figure 58, show good agreement between theoretical values and experiment data, which implies the higher growing speed in the high temperature growth comes from solid wire growths.

In this section the deposition rate of the meniscus-confined electrodeposition was increased by raising the temperature at growth interface with a metal ceramic heater. Results show that the effect of temperature is significant either for the growth performed with a single pipette, a 1 by 10 1D array, and a 10 by 10 2D array. When comparing pulling speeds calculated from the current data to that measured in experiments, the higher speed growth results was verified, indeed, come from the solid wire growth. This provides a potential solution to further increase production efficiency beyond the array-based growth.

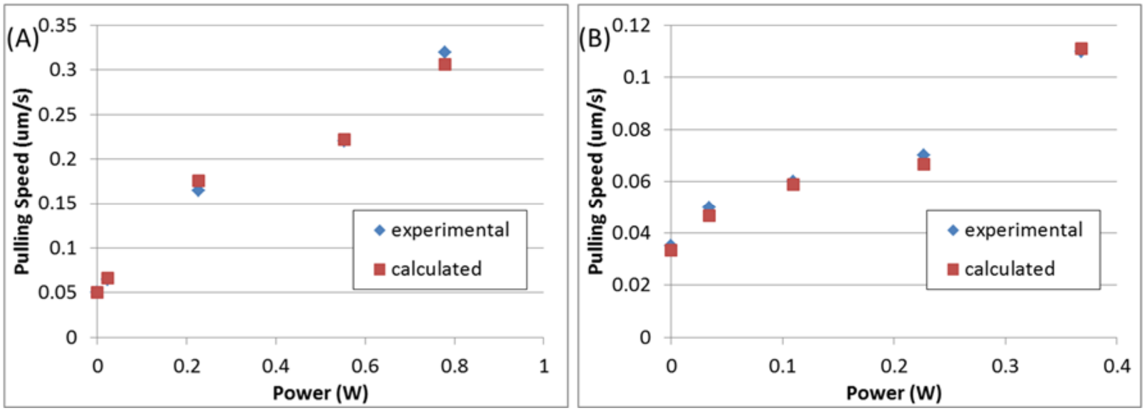

Figure 58. Plots of pulling speeds with respect to heating powers for (A) a 1 by 10 1D nozzle array, and (B) a 10 by 10 2D array.

7.5 Summary

In this chapter, several extended applications of the meniscus-confined electrochemical method were discussed, including adjusting AC voltage frequency and on/off ratio to produce micro hollow tubes, reverse the voltage for electrochemical etching on transparent glass substrates, and raise the temperature of the growth interface to accelerate deposition rate. Mechanisms are qualitatively studied based on preliminary results in an effort to explore the potential directions of the development of the meniscus-confined electrochemical method.

CHAPTER 8

SUMMARY

In this study, I explored a self-regulated growth mechanism revealed in the meniscus-confined direct-write electrodeposition method to realize the parallel process fabrication of high density area arrays of ultrahigh aspect-ratio metal microwires with designed shape and mechanical characteristics. A theoretical model that provides a fundamental understanding of the array-based meniscus-confined electrodeposition was developed. Precision nozzle arrays were designed and fabricated using surface micromaching processes that took advantage of high resolution of photolithography and met the dimensional precision requirement for realizing the parallel process fabrication. High density area array fabrication of ultrahigh aspect-ratio metal microwires were then realized with the designed shape and mechanical characteristics using the array-based parallel process fabrication method. Such an electrode array structure was designed and studied for wafer probe testing application. It was expected that such a scale-up fabrication process for making high density electrode arrays could provide a cost effective and flexible alternative for developing electrical interconnection structures possessing designed mechanical, thermal and structural properties with micro-/nano-scale resolutions that could match with the requirement for the I/O architectures at the chip scale level of integrated circuits.

In addition, the meniscus-confined electrodeposition was integrated with a 3-D printing process for fabricating ultrahigh density and ultrahigh aspect-ratio metal structures with complex 3-D shapes and even nanoscale resolution. An array nozzle based process was also realized for this microscale 3-D metal printing method, and was shown to be capable of being significantly scaled up for more advanced fabrication.

Several preliminary studies were also performed that laid the foundation for future development of the technology. Pulsed electrodeposition was explored in the meniscus-confined electrodeposition and was shown to produce metal tube microstructures. Localized electrochemical etching was integrated with the meniscus-confined electrodeposition to create a novel way for patterning curved metal surfaces. Finally, electrodeposition at elevated temperature above the room temperature was studied with the meniscus-confined electrodeposition and was seen to be capable of significantly increasing the deposition rate in the nozzle array based fabrication.

The development described in this dissertation is believed to be unique in the field of 3-D manufacturing, and provides an essential tool for fabricating metal structures with electrical/mechanical/structural quality, dimensional resolution, aspect-ratio and spatial density that are unmatched by other traditional fabrication methods. Moreover, further extended development is possible to advance new processes and methods for fabricating more complicated 3-D structures beyond the simple metal material system based on the mechanisms and processes described in this research.

REFERENCES

1. S. Xu *et al.*, Assembly of micro/nanomaterials into complex, three-dimensional architectures by compressive buckling. *Science* **347**, 154-159 (2015).
2. T. A. Schaedler *et al.*, Ultralight Metallic Microlattices. *Science* **334**, 962-965 (2011).
3. H. Gao *et al.*, Large-scale nanoshaping of ultrasmooth 3D crystalline metallic structures. *Science* **346**, 1352-1356 (2014).
4. R. Bhandari, S. Negi, F. Solzbacher, Wafer-scale fabrication of penetrating neural microelectrode arrays. *Biomed. Microdevices* **12**, 797-807 (2010).
5. S. Takeuchi, T. Suzuki, K. Mabuchi, H. Fujita, 3D flexible multichannel neural probe array. *J Micromech Microeng* **14**, 104-107 (2004).
6. M. J. Madou, *Fundamentals of microfabrication : the science of miniaturization*. (CRC Press, Boca Raton, FL, ed. 2nd, 2002), pp. 723 p.
7. W. Chen, S. K. Sitaraman, Area-Array of 3-Arc-Fan Compliant Interconnects as Effective Drop-Impact Isolator for Microsystems. *J Microelectromech S* **25**, 337-346 (2016).
8. K. Kacker, S. K. Sitaraman, Design and Fabrication of FlexConnects: A Cost-Effective Implementation of Compliant Chip-to-Substrate Interconnects. *Ieee T Compon Pack T* **31**, 816-823 (2008).
9. Q. Zhu, L. Y. Ma, S. K. Sitaraman, beta-Helix: A lithography-based compliant off-chip interconnect. *Ieee T Compon Pack T* **26**, 582-590 (2003).
10. Q. Zhu, L. Y. Ma, S. K. Sitaraman, Design optimization of one-turn helix: A novel compliant off-chip interconnect. *Ieee T Adv Packaging* **26**, 106-112 (2003).
11. C. K. Malek, V. Saile, Applications of LIGA technology to precision manufacturing of high-aspect-ratio micro-components and -systems: a review. *Microelectron. J.* **35**, 131-143 (2004).
12. E. W. Becker *et al.*, Production of Separation-Nozzle Systems for Uranium Enrichment by a Combination of X-Ray-Lithography and Galvanoplastics. *Naturwissenschaften* **69**, 520-523 (1982).
13. E. W. Becker, W. Ehrfeld, P. Hagmann, A. Maner, D. Münchmeyer, Fabrication of microstructures with high aspect ratios and great structural heights by synchrotron radiation lithography, galvanoforming, and plastic moulding (LIGA process). *Microelectron. Eng.* **4**, 35-56 (1986).
14. H. Lorenz *et al.*, SU-8: a low-cost negative resist for MEMS. *J Micromech Microeng* **7**, 121-124 (1997).
15. C. H. Lin, G. B. Lee, B. W. Chang, G. L. Chang, A new fabrication process for ultra-thick microfluidic microstructures utilizing SU-8 photoresist. *J Micromech Microeng* **12**, 590-597 (2002).
16. J. D. Madden, I. W. Hunter, Three-dimensional microfabrication by localized electrochemical deposition. *J Microelectromech S* **5**, 24-32 (1996).
17. E. M. El-Giar, R. A. Said, G. E. Bridges, D. J. Thomson, Localized electrochemical deposition of copper microstructures. *J. Electrochem. Soc.* **147**, 586-591 (2000).
18. A. D. Muller, F. Muller, M. Hietschold, Localized electrochemical deposition of metals using micropipettes. *Thin Solid Films* **366**, 32-36 (2000).

19. A. Jansson, G. Thornell, S. Johansson, High resolution 3D microstructures made by localized electrodeposition of nickel. *J. Electrochem. Soc.* **147**, 1810-1817 (2000).
20. S. Yeo, J. Choo, K. Sim, On the effects of ultrasonic vibrations on localized electrochemical deposition. *J Micromech Microeng* **12**, 271 (2002).
21. R. A. Said, Shape formation of microstructures fabricated by localized electrochemical deposition. *J. Electrochem. Soc.* **150**, C549-C557 (2003).
22. R. A. Said, Localized electro-deposition (LED): the march toward process development. *Nanotechnology* **15**, S649-S659 (2004).
23. J. E. Smay, J. Cesarano, J. A. Lewis, Colloidal inks for directed assembly of 3-D periodic structures. *Langmuir* **18**, 5429-5437 (2002).
24. Q. Li, J. A. Lewis, Nanoparticle Inks for Directed Assembly of Three-Dimensional Periodic Structures. *Adv. Mater.* **15**, 1639-1643 (2003).
25. G. M. Gratson, M. Xu, J. A. Lewis, Microperiodic structures: Direct writing of three-dimensional webs. *Nature* **428**, 386-386 (2004).
26. B. Y. Ahn *et al.*, Omnidirectional Printing of Flexible, Stretchable, and Spanning Silver Microelectrodes. *Science* **323**, 1590-1593 (2009).
27. S. Z. Guo *et al.*, Solvent-Cast Three-Dimensional Printing of Multifunctional Microsystems. *Small* **9**, 4118-4122 (2013).
28. S. Z. Guo, M. C. Heuzey, D. Therriault, Properties of Polylactide Inks for Solvent-Cast Printing of Three-Dimensional Freeform Microstructures. *Langmuir* **30**, 1142-1150 (2014).
29. H. W. P. Koops *et al.*, Characterization and Application of Materials Grown by Electron-Beam-Induced Deposition. *Jpn J Appl Phys 1* **33**, 7099-7107 (1994).
30. B. Bhushan, *Springer handbook of nanotechnology*. (Springer, Berlin ; New York, ed. 2nd rev. & extended, 2007), pp. xliv, 1916 p.
31. M. Vaezi, H. Seitz, S. F. Yang, A review on 3D micro-additive manufacturing technologies. *Int J Adv Manuf Tech* **67**, 1721-1754 (2013).
32. S. J. Randolph, J. D. Fowlkes, P. D. Rack, Focused, nanoscale electron-beam-induced deposition and etching. *Crit. Rev. Solid State Mater. Sci.* **31**, 55-89 (2006).
33. S. Matsui, T. Ichihashi, I nsitu observation on electron-beam-induced chemical vapor deposition by transmission electron microscopy. *Appl. Phys. Lett.* **53**, 842-844 (1988).
34. I. Utke, P. Hoffmann, J. Melngailis, Gas-assisted focused electron beam and ion beam processing and fabrication. *Journal of Vacuum Science & Technology B: Microelectronics and Nanometer Structures Processing, Measurement, and Phenomena* **26**, 1197-1276 (2008).
35. S. Reyntjens, R. Puers, A review of focused ion beam applications in microsystem technology. *J Micromech Microeng* **11**, 287-300 (2001).
36. O. Lehmann, M. Stuke, 3-Dimensional Laser Direct Writing of Electrically Conducting and Isolating Microstructures. *Mater. Lett.* **21**, 131-136 (1994).
37. O. Lehmann, M. Stuke, Generation of 3-Dimensional Freestanding Metal Micro-Objects by Laser Chemical-Processing. *Appl Phys a-Mater* **53**, 343-345 (1991).
38. K. Kanda *et al.*, NEXAFS study on carbon-based material formed by focused-ion-beam chemical-vapor-deposition. *Radiat. Phys. Chem.* **75**, 1850-1854 (2006).

39. F. Foulon, O. Lehmann, M. Stuke, Laser Direct-Write Al Deposition on Si, Gaas and Diamond from Trialkylamine-Alane Precursors. *Appl. Surf. Sci.* **69**, 87-93 (1993).
40. D. Stewart, J. Morgan, B. Ward, Focused ion beam induced deposition of tungsten on vertical sidewalls. *Journal of Vacuum Science & Technology B: Microelectronics and Nanometer Structures Processing, Measurement, and Phenomena* **9**, 2670-2674 (1991).
41. M. Ishida *et al.*, Focused ion beam-induced fabrication of tungsten structures. *Journal of Vacuum Science & Technology B: Microelectronics and Nanometer Structures Processing, Measurement, and Phenomena* **21**, 2728-2731 (2003).
42. H. Komano, H. Nakamura, T. Takigawa, A rewiring technique for integrated circuit operation analysis using a silicon oxide film deposited by a focused ion beam. *Journal of Vacuum Science & Technology B: Microelectronics and Nanometer Structures Processing, Measurement, and Phenomena* **9**, 2653-2655 (1991).
43. M. Ogasawara *et al.*, Beam induced deposition of an ultraviolet transparent silicon oxide film by focused gallium ion beam. *Appl. Phys. Lett.* **68**, 732-734 (1996).
44. T. Morita *et al.*, Free-space-wiring fabrication in nano-space by focused-ion-beam chemical vapor deposition. *Journal of Vacuum Science & Technology B: Microelectronics and Nanometer Structures Processing, Measurement, and Phenomena* **21**, 2737-2741 (2003).
45. T. M. Lee *et al.*, Drop-on-demand solder droplet jetting system for fabricating microstructure. *Ieee T Electron Pack* **31**, 202-210 (2008).
46. K. Yamaguchi, K. Sakai, T. Yamanaka, T. Hirayama, Generation of three-dimensional micro structure using metal jet. *Precis Eng* **24**, 2-8 (2000).
47. A. I. Kuznetsov, R. Kiyan, B. N. Chichkov, Laser fabrication of 2D and 3D metal nanoparticle structures and arrays. *Opt. Express* **18**, 21198-21203 (2010).
48. C. W. Visser *et al.*, Toward 3D Printing of Pure Metals by Laser-Induced Forward Transfer. *Adv. Mater.* **27**, 4087-4092 (2015).
49. C. Ladd, J. H. So, J. Muth, M. D. Dickey, 3D Printing of Free Standing Liquid Metal Microstructures. *Adv. Mater.* **25**, 5081-5085 (2013).
50. P. F. Jacobs, *Rapid prototyping & manufacturing: fundamentals of stereolithography*. (Society of Manufacturing Engineers, 1992).
51. C. W. Hull. (Google Patents, 1986).
52. I. Gibson, D. W. Rosen, B. Stucker, *Additive manufacturing technologies*. (Springer, 2010), vol. 238.
53. C. Sun, N. Fang, D. M. Wu, X. Zhang, Projection micro-stereolithography using digital micro-mirror dynamic mask. *Sensor Actuat a-Phys* **121**, 113-120 (2005).
54. J. R. Tumbleston *et al.*, Continuous liquid interface production of 3D objects. *Science* **347**, 1349-1352 (2015).
55. M. Vaezi, H. Seitz, S. Yang, A review on 3D micro-additive manufacturing technologies. *The International Journal of Advanced Manufacturing Technology* **67**, 1721-1754 (2013).
56. S. Maruo, S. Kawata, Two-photon-absorbed near-infrared photopolymerization for three-dimensional microfabrication. *J Microelectromech S* **7**, 411-415 (1998).

57. S. H. Park, T. W. Lim, D.-Y. Yang, N. C. Cho, K.-S. Lee, Fabrication of a bunch of sub-30-nm nanofibers inside microchannels using photopolymerization via a long exposure technique. *Appl. Phys. Lett.* **89**, 173133 (2006).
58. S. Maruo, O. Nakamura, S. Kawata, Three-dimensional microfabrication with two-photon-absorbed photopolymerization. *Opt. Lett.* **22**, 132-134 (1997).
59. H.-B. Sun, S. Matsuo, H. Misawa, Three-dimensional photonic crystal structures achieved with two-photon-absorption photopolymerization of resin. *Appl. Phys. Lett.* **74**, 786-788 (1999).
60. M. Straub, M. Gu, Near-infrared photonic crystals with higher-order bandgaps generated by two-photon photopolymerization. *Opt. Lett.* **27**, 1824-1826 (2002).
61. B. H. Cumpston *et al.*, Two-photon polymerization initiators for three-dimensional optical data storage and microfabrication. *Nature* **398**, 51-54 (1999).
62. D. Day, M. Gu, A. Smallridge, Use of two-photon excitation for erasable–rewritable three-dimensional bit optical data storage in a photorefractive polymer. *Opt. Lett.* **24**, 948-950 (1999).
63. P. Galajda, P. Ormos, in *Lasers and Electro-Optics, 2002. CLEO'02. Technical Digest. Summaries of Papers Presented at the*. (IEEE, 2002), pp. 634-635.
64. H. Xia *et al.*, Ferrofluids for Fabrication of Remotely Controllable Micro-Nanomachines by Two-Photon Polymerization. *Adv. Mater.* **22**, 3204-3207 (2010).
65. S. Maruo, H. Inoue, Optically driven micropump produced by three-dimensional two-photon microfabrication. *Appl. Phys. Lett.* **89**, 144101 (2006).
66. S. Kawata, H.-B. Sun, T. Tanaka, K. Takada, Finer features for functional microdevices. *Nature* **412**, 697-698 (2001).
67. K. Sun *et al.*, 3D Printing of Interdigitated Li-Ion Microbattery Architectures. *Adv. Mater.* **25**, 4539-4543 (2013).
68. B. Leukers *et al.*, Hydroxyapatite scaffolds for bone tissue engineering made by 3D printing. *J Mater Sci-Mater M* **16**, 1121-1124 (2005).
69. C. X. F. Lam, X. M. Mo, S. H. Teoh, D. W. Hutmacher, Scaffold development using 3D printing with a starch-based polymer. *Mat Sci Eng C-Bio S* **20**, 49-56 (2002).
70. S. Kawata, H. B. Sun, T. Tanaka, K. Takada, Finer features for functional microdevices - Micromachines can be created with higher resolution using two-photon absorption. *Nature* **412**, 697-698 (2001).
71. D. C. Jang, L. R. Meza, F. Greer, J. R. Greer, Fabrication and deformation of three-dimensional hollow ceramic nanostructures. *Nat Mater* **12**, 893-898 (2013).
72. L. R. Meza, S. Das, J. R. Greer, Strong, lightweight, and recoverable three-dimensional ceramic nanolattices. *Science* **345**, 1322-1326 (2014).
73. L. C. Montemayor, L. R. Meza, J. R. Greer, Design and Fabrication of Hollow Rigid Nanolattices via Two-Photon Lithography. *Adv. Eng. Mater.* **16**, 184-189 (2014).
74. A. Cohen *et al.*, EFAB: low-cost automated electrochemical batch fabrication of arbitrary 3-D microstructures. *P Soc Photo-Opt Ins* **3874**, 236-247 (1999).
75. A. Cohen *et al.*, EFAB: Rapid, low-cost desktop micromachining of high aspect ratio true 3-D MEMS. *Proc Ieee Micr Elect*, 244-251 (1999).

76. A. Cohen *et al.*, EFAB: Batch production of functional, fully-dense metal parts with micron-scale features. *Sol Freeform Fabric*, 161-168 (1998).
77. K. Subramanian, N. Vail, J. Barlow, H. Marcus, Selective laser sintering of alumina with polymer binders. *Rapid Prototyping J* **1**, 24-35 (1995).
78. H. Exner, P. Regenfuss, L. Hartwig, S. Klötzer, R. Ebert, in *Fourth International Symposium on Laser Precision Microfabrication*. (International Society for Optics and Photonics, 2003), pp. 145-151.
79. P. Regenfuss *et al.*, Industrial freeform generation of microtools by laser micro sintering. *Rapid Prototyping J* **11**, 18-25 (2005).
80. A. T. Clare, P. R. Chalker, S. Davies, C. J. Sutcliffe, S. Tsopanos, Selective laser melting of high aspect ratio 3D nickel–titanium structures two way trained for MEMS applications. *International Journal of Mechanics and Materials in Design* **4**, 181-187 (2008).
81. J.-P. Kruth *et al.*, Selective laser melting of iron-based powder. *J. Mater. Process. Technol.* **149**, 616-622 (2004).
82. B. Vandenbroucke, J.-P. Kruth, Selective laser melting of biocompatible metals for rapid manufacturing of medical parts. *Rapid Prototyping J* **13**, 196-203 (2007).
83. F. Abe, K. Osakada, M. Shiomi, K. Uematsu, M. Matsumoto, The manufacturing of hard tools from metallic powders by selective laser melting. *J. Mater. Process. Technol.* **111**, 210-213 (2001).
84. J.-P. Kruth, P. Mercelis, J. Van Vaerenbergh, L. Froyen, M. Rombouts, Binding mechanisms in selective laser sintering and selective laser melting. *Rapid Prototyping J* **11**, 26-36 (2005).
85. A. P. Suryavanshi, M. F. Yu, Electrochemical fountain pen nanofabrication of vertically grown platinum nanowires. *Nanotechnology* **18**, (2007).
86. M. Minary-Jolandan, A. Tajik, N. Wang, M. F. Yu, Intrinsically high-Q dynamic AFM imaging in liquid with a significantly extended needle tip. *Nanotechnology* **23**, (2012).
87. J. Hu, M. F. Yu, Meniscus-Confined Three-Dimensional Electrodeposition for Direct Writing of Wire Bonds. *Science* **329**, 313-316 (2010).
88. J. Hu *et al.*, Diffusion limited current in very high aspect ratio Pt needle electrodes. *Appl. Phys. Lett.* **99**, (2011).
89. K. Yum, N. Wang, M. F. Yu, Nanoneedle: A multifunctional tool for biological studies in living cells. *Nanoscale* **2**, 363-372 (2010).
90. M. Minary-Jolandan, M. F. Yu, Nanomechanical imaging of soft samples in liquid using atomic force microscopy. *J. Appl. Phys.* **114**, (2013).
91. A. P. Suryavanshi, J. Hu, M. F. Yu, Meniscus-controlled continuous fabrication of arrays and rolls of extremely long micro- and nano-fibers. *Adv. Mater.* **20**, 793-+ (2008).
92. A. P. Suryavanshi, M. F. Yu, Probe-based electrochemical fabrication of freestanding Cu nanowire array. *Appl. Phys. Lett.* **88**, (2006).
93. M. Paunovic, M. Schlesinger, Electrochemical Society., *Fundamentals of electrochemical deposition*. The Electrochemical Society series (Wiley, New York, 1998), pp. viii, 301 p.

94. A. J. Bard, L. R. Faulkner, *Electrochemical methods : fundamentals and applications*. (Wiley, New York, ed. 2nd, 2001), pp. xxi, 833 p.
95. A. Suryavanshi, Ph.D., University of Illinois at Urbana-Champaign, (2007).
96. S. Chen, A. Kucernak, Electrodeposition of Platinum on Nanometer-Sized Carbon Electrodes. *The Journal of Physical Chemistry B* **107**, 8392-8402 (2003).
97. J. O. M. Bockris, B. E. Conway, in *Modern aspects series of chemistry*. (Plenum Press etc., New York etc., 1954), pp. no.
98. S. S. Djoki*c, SpringerLink (Online service), in *Modern Aspects of Electrochemistry,*. (Springer Science+Business Media, LLC,, New York, NY, 2010), pp. 1 online resource.
99. J. M. Maxwell, M. G. Huson, Using the scanning probe microscope to measure the effect of relative humidity on sample stiffness. *Rev. Sci. Instrum.* **73**, 3520-3524 (2002).
100. O. Stukalov, C. A. Murray, A. Jacina, J. R. Dutcher, Relative humidity control for atomic force microscopes. *Rev. Sci. Instrum.* **77**, (2006).
101. L. Heerman, A. Tarallo, Theory of the chronoamperometric transient for electrochemical nucleation with diffusion-controlled growth. *J. Electroanal. Chem.* **470**, 70-76 (1999).
102. B. R. Scharifker, Diffusion to Ensembles of Microelectrodes. *J. Electroanal. Chem.* **240**, 61-76 (1988).
103. J. Strutwolf, M. D. Scanlon, D. W. M. Arrigan, Electrochemical ion transfer across liquid/liquid interfaces confined within solid-state micropore arrays - simulations and experiments. *Analyst* **134**, 148-158 (2009).
104. S. Wilke, M. D. Osborne, H. H. Girault, Electrochemical characterisation of liquid|liquid microinterface arrays. *J. Electroanal. Chem.* **436**, 53-64 (1997).
105. B. Scharifker, G. Hills, Theoretical and Experimental Studies of Multiple Nucleation. *Electrochim. Acta* **28**, 879-889 (1983).
106. B. R. Scharifker, J. Mostany, 3-Dimensional Nucleation with Diffusion Controlled Growth .1. Number Density of Active-Sites and Nucleation Rates Per Site. *J. Electroanal. Chem.* **177**, 13-23 (1984).
107. A. M. Bond, D. Luscombe, K. B. Oldham, C. G. Zoski, A Comparison of the Chronoamperometric Response at Inlaid and Recessed Disk Microelectrodes. *J. Electroanal. Chem.* **249**, 1-14 (1988).
108. V. A. Tatarchenko, *Shaped crystal growth*. Fluid mechanics and its applications (Kluwer Academic, Dordrecht ; Boston, 1993), pp. x, 287 p.
109. E. J. Marinissen, in *Proceedings of the Conference on Design, Automation and Test in Europe*. (EDA Consortium, 2012), pp. 1277-1282.
110. E. J. Marinissen, in *Proceedings of the Conference on Design, Automation and Test in Europe*. (European Design and Automation Association, 2010), pp. 1689-1694.
111. G. L. Mathieu, B. N. Eldridge, G. W. Grube. (Google Patents, 2001).
112. F. Wang, R. Cheng, X. Li, MEMS vertical probe cards with ultra densely arrayed metal probes for wafer-level IC testing. *J Microelectromech S* **18**, 933-941 (2009).

113. V. Y. Gertsman, M. Hoffmann, H. Gleiter, R. Birringer, The Study of Grain-Size Dependence of Yield Stress of Copper for a Wide Grain-Size Range. *Acta Metall Mater* **42**, 3539-3544 (1994).
114. J. Schiotz, K. W. Jacobsen, A maximum in the strength of nanocrystalline copper. *Science* **301**, 1357-1359 (2003).
115. L. Lu, X. Chen, X. Huang, K. Lu, Revealing the Maximum Strength in Nanotwinned Copper. *Science* **323**, 607-610 (2009).
116. M. A. Meyers, A. Mishra, D. J. Benson, Mechanical properties of nanocrystalline materials. *Prog. Mater Sci.* **51**, 427-556 (2006).
117. M. A. Meyers, K. K. Chawla, *Mechanical behavior of materials*. (Cambridge University Press, Cambridge ; New York, ed. 2nd, 2009), pp. xxii, 856 p.
118. G. Kartopu, O. Yalçın, *Fabrication and applications of metal nanowire arrays electrodeposited in ordered porous templates*. (INTECH Open Access Publisher, 2010).

VITA

Yen-Po Lin

Yen-Po Lin was born in Tainan, Taiwan. He received a B.S. in the Power Mechanical Engineering from National Tsing Hua University, Hsinchu, Taiwan in 2006 and a M.S. in Mechanical Engineering from Texas A&M University, College Station, Texas in 2010. Before coming to Georgia Institute of Technology to pursue a doctorate degree in Mechanical Engineering in 2012, he started his Ph.D. study in University of Illinois at Urbana Champaign, Champaign, Illinois in 2010, where he joined the research group under the guidance of Dr. Min-Feng Yu. His research expertise is on microscale and nanoscale fabrication/characterization, electrochemical deposition, precision 3-D manufacturing and instrument development. Through this research, he developed an electrodeposition-based high-throughput parallel process fabrication method for making high density three-dimensional metal microstructures.